

Characterizing Quantum-Dot Cellular Automata

by

Burkhard Ritter

A thesis submitted in partial fulfillment of the requirements for the degree of

Doctor of Philosophy

Department of Physics  
University of Alberta

©Burkhard Ritter, 2014

# Abstract

We undertake an in-depth numerical study of quantum-dot cellular automata (QCA), a beyond-CMOS computing paradigm which represents bits as bistable charge distributions in cells consisting of quantum dots. Using semi-realistic but material-independent modelling, we characterize the building blocks of QCA circuits in as detailed and unbiased a manner as possible. Starting from an extended Hubbard model, and introducing two controlled Hilbert space truncations whose limits we study and understand, we use exact diagonalization to calculate time-independent properties of small systems. We derive a transverse-field Ising model as an effective description for QCA devices, but find that it is only valid in a restrictive parameter range. We demonstrate that the commonly used intercellular Hartree approximation is inadequate and gives results that are qualitatively incorrect. In contrast to previous work, we show that the response between pairs of adjacent cells is linear and does not exhibit gain. Non-linearity and gain only emerge in response to static-charge input cells that have no quantum dynamics of their own. As a consequence, QCA circuits cannot retain a logic state in the thermodynamic limit, and there is a maximum circuit size set by the system's parameters. Overall, QCA as a computing architecture is seen to be more fragile than previously thought. We establish charge neutral cells as a strict requirement for QCA operation. We identify parameter bounds for functional devices: small cell-cell distances, moderate temperatures, and large Coulomb energy scales are necessary.

# Acknowledgments

This thesis concludes almost four years of work at the University of Alberta and could not have been written without the help and support of my mentors, coworkers, friends, and family.

I would like to thank my colleague and office mate Christopher Polachic for tirelessly enduring my monologues on quantum-dot cellular automata, bouncing off my ideas, and giving valuable feedback. Thanks to him I am equipped with a better understanding of the dynamic mean field theory and the dynamic Hubbard model, and everything from Canadian childcare to Quebec's separation efforts to sensible stock investments. My coworker Jin Xu has taught me about most things between spin systems and job hunting, and has always been there for some deeper insights into Chinese culture. I would like to thank him. I am indebted to Roshan Achal for distractful office lunch breaks and a fun year with the graduate physics student association. I extend my gratitude to Carl Chandler for writing a small software library together and for tolerating my snoring in Denver. I owe a great trip to Boston and New York, a missed flight, and an awesome time in Dresden to Fabian Zschocke, with whom I shared the office for one year.

Marco Taucer and the whole group of Robert Wolkow have provided valuable comments on my ideas and calculations, and patiently explained dangling bonds on silicon and their understanding of and vision for quantum-dot cellular automata. Their experiments originally inspired my research and I am greatly thankful for their work and feedback.

I would like to note the advice and support I have received from my supervisory committee members, Mark Freeman, Massimo Boninsegni, and Frank Marsiglio. I am very grateful for them accepting and working with my tight deadlines. Special thanks go to my supervisor Kevin Beach. He has provided guidance and help over the years, and an all-in-all very comfortable and enjoyable environment. It has been a pleasure to work with him. I am also grateful to my previous supervisor Fakher Assaad for suggesting that I

work with Kevin Beach and move to Edmonton, the nice city with the underwhelming reputation in the middle of nowhere in western Canada, in the first place. I thank Alberta Innovates - Technology Futures for paying my living for the last two years. I am grateful for Kevin's NSERC Discovery grant for covering travelling and other expenses.

I particularly want to thank my girlfriend Esly Alvarez for encouraging me to keep going, convincing me that this thesis can actually be completed, and for accepting my working odd hours through the night. I thank her for always being there and moving around half the world with me.

# Contents

<b>1</b>	<b>Introduction</b>	<b>1</b>
<b>2</b>	<b>Quantum-dot cellular automata</b>	<b>10</b>
2.1	An alternative computing paradigm . . . . .	10
2.2	Atomic silicon quantum dots . . . . .	17
2.3	The extended Hubbard model . . . . .	20
2.4	Basic characterization . . . . .	23
2.5	Exact diagonalization . . . . .	28
<b>3</b>	<b>Approximations</b>	<b>31</b>
3.1	Fixed charge model . . . . .	31
3.2	Bond model . . . . .	32
3.3	Ising model . . . . .	33
3.4	Validity of the approximations . . . . .	41
<b>4</b>	<b>Characterization</b>	<b>55</b>
4.1	The three-cell wire . . . . .	55
4.2	Workable parameters for QCA . . . . .	62
4.3	The majority gate . . . . .	72
<b>5</b>	<b>Conclusion</b>	<b>75</b>

# List of Tables

4.1	Critical $V_1$ for different systems . . . . .	64
-----	--	----

# List of Figures

2.1	Building blocks of quantum-dot cellular automata (QCA) circuitry . . . . .	11
2.2	QCA gates . . . . .	12
2.3	Clocked QCA for a line of cells . . . . .	16
2.4	Atomic silicon quantum dots . . . . .	18
2.5	Parameterizing QCA layouts . . . . .	21
2.6	Basic characteristics of QCA devices . . . . .	24
3.1	The six bonds of a QCA cell . . . . .	32
3.2	Mapping QCA to an Ising-like model . . . . .	33
3.3	The fixed-charge approximation . . . . .	42
3.4	The bond approximation for a one-cell system . . . . .	42
3.5	The bond approximation for a two-cell system . . . . .	45
3.6	The Ising approximation for a one-cell system . . . . .	47
3.7	The Ising approximation for a two-cell system . . . . .	50
3.8	The Ising approximation for three- to five-cell wires . . . . .	53
4.1	The cell-cell polarization response . . . . .	56
4.2	Cell polarization over cell-cell distance . . . . .	57
4.3	Cell polarization over the inter-cell angle . . . . .	61
4.4	The semi-infinite wire . . . . .	64
4.5	Self-consistent polarization and critical $V_1$ . . . . .	64
4.6	Cell polarizations along two- to twelve-cell wires . . . . .	66
4.7	Cell-cell response over $V_1$ and cell-cell distance . . . . .	66
4.8	The majority gate . . . . .	73

# Acronyms

CMOS	complementary metal-oxide-semiconductor
CNTFET	carbon nanotube field-effect transistor
DB	dangling bond
EQCA	electrostatic quantum-dot cellular automata
FET	field-effect transistor
ICHA	intercellular Hartree approximation
ITRS	International Technology Roadmap for Semiconductors
LED	light-emitting diode
MEM	micro-electro-mechanical
MEMS	micro-electro-mechanical systems
MOSFET	metal-oxide-semiconductor field-effect transistor
MQCA	magnetic quantum-dot cellular automata
NML	nanomagnetic logic
NMOS	n-type metal-oxide-semiconductor
QCA	quantum-dot cellular automata
SSE	stochastic series expansion
STM	scanning tunnelling microscope



# Notation

$a$	edge length of a cell
$d$	cell-cell distance
$\theta$	inter-cell angle
$q$	compensation charge
$\mu$	chemical potential
$T$	temperature
$t$	hopping parameter
$U$	on-site Coulomb repulsion
$V_1$	nearest-neighbour Colomb repulsion ( $V_1 = 1/a$ )
$V_0$	next-nearest-neighbour Colomb repulsion ( $V_0 = 1/\sqrt{2a^2}$ )
$V_{\text{1crit}}$	mean field critical $V_1$
$\Delta E_{\text{S}}$	singlet-triplet splitting
$P_k$	cell polarization (of cell $k$ )
$P_{\text{D}}$	polarization of the driver cell
$\epsilon_k^{\text{I}}$	relative error of the polarization of cell $k$ for the Ising model
$\epsilon_k^{\text{B}}$	relative error of the polarization of cell $k$ for the bond model
$\chi_{kl}$	linear polarization response of cell $k$ with respect to cell $l$
$\chi$	linear nearest-neighbour polarization response (the same for all cells)
$\chi_{\text{e}}$	linear polarization response of the system to an external driver cell
$H_k^{\text{c}}$	single-cell Hamiltonian
$H_{kl}^{\text{cc}}$	Coulombic cell-cell interaction (between cells $k$ and $l$ )
$S_k^z$	pseudo spin (of cell $k$ )
$J_{kl}$	Ising cell-cell interaction (between cells $k$ and $l$ )
$J'_{kl}$	modified Ising cell-cell interaction (between cells $k$ and $l$ )
$\gamma$	Ising transverse field / effective hopping parameter

# Chapter 1

## Introduction

The rise of electronic information technology has been one of the main drivers of economical and societal change over the past seventy years. Computers have flown us to the moon, trade stocks, diagnose illnesses, and even run simulations of quantum spin systems. The advent of the internet, invented some 25 years ago, and the relentless march of an army of mobile gadgets, from the venerable notebook, over the smart phone and tablet, to wearable tech of all forms and colours, together with readily available mobile data connections, is changing the way we communicate, socialize, read, write and think. The benefits of information technology are so multifaceted and ubiquitous that it is easy to take them for granted. Yet as we ask for faster, more functionally rich, and lighter devices, the data centres that feed us our cloud streams have developed a great hunger for energy. And if the internet of things is supposed to happen, it surely needs more energy-efficient devices than the phones that we always keep in sight of a power outlet. The desire to build functional and at the same time more power-efficient computing technology has led to efforts at all levels of the technology stack, from the data centres, to the processor architectures, to better and more parallel algorithms. Digital circuitry and specifically the transistor, which underpins all of modern day information technology, have not been an exception.

The penetration of computing technology into all aspects of modern life has been fuelled by the incredible success of the complementary metal-oxide-semiconductor (CMOS) integrated circuit. Computer chips have become ever more cheaper, smaller, power-efficient, and at the same time much more capable. But there is a growing concern that CMOS is close to its scaling limits—that it can no longer become ever faster and cheaper. CMOS uses two complementary n-type and p-type metal-oxide-semiconductor field-effect transis-

tors (MOSFETs), greatly reducing power consumption compared to older technologies, such as n-type metal-oxide-semiconductor (NMOS) logic. Invented in the early 1960s, the CMOS integrated circuit has since seen the number of transistors per chip double roughly every two years, an exponential growth predicted by Gordon Moore and hence known as Moore’s law [1]. Whereas in the eighties feature sizes were on the order of micrometres, today’s processors use a 22 nm process and integrate billions of transistors on a single chip [2]. One of the main reasons for the relentless miniaturization of CMOS technology is cost reduction. In the manufacturing process, the cost is dominantly set per wafer—the slab of pure crystalline silicon used as the device substrate. Therefore, chips become cheaper by either increasing the size of the wafer—current silicon wafers are typically 30 cm in diameter—or by increasing the device density and thus by smaller feature sizes. Obviously, higher device density means more functionality per same-area chip. But smaller feature sizes also, in principle, allow for shorter switching times and reduced switching energy, and thus faster and more power-efficient devices. In the past, obstacles that seemed to inhibit the continued downscaling were time and again overcome by scientific and engineering ingenuity, and the exponential growth predicted by Moore’s law has been kept pace with. Technological innovation has been fuelled and financed by consumer demand for more capable and functionally rich devices.

Historically, feature size scaling was limited by the photolithographic process used to manufacture semiconductor integrated circuits. But advances in fabrication technology, such as 193 nm immersion lithography and double patterning, have pushed below the 32 nm mark, with 10 nm deemed possible [3,4]. Beyond, extreme ultraviolet lithography is being developed, promising even smaller feature sizes [5]. These dimensions approach the atomic scale and further downsizing is increasingly inhibited by the fundamental physical limits of the MOSFET. Simply put, the smaller the transistor in size, the higher the leakage currents. There are several leakage channels. If the distance between source and drain becomes too small, then electrons can tunnel through the channel region regardless of the gate barrier, and it has been estimated that 5.9 nm is the minimal gate dimension before this tunnelling current becomes substantial [6]. Similarly, the gate voltage has to shrink with shrinking feature sizes, which increases the subthreshold current through the channel region. Lastly, if the gate oxide layer becomes too thin, electrons can tunnel from the gate to the drain, again leading to a leakage current. Some of these problems can be mitigated by technological advances. For example, current generation microprocessors substitute the traditionally used silicon dioxide with materials with higher relative permittivities, such

as hafnium oxide, for the gate oxide, allowing thicker oxide layers and thus decreasing electron tunnelling. But overall, smaller feature sizes, which lead to faster switching times and higher device densities, significantly increase leakage currents. Already, leakage is a substantial part of the total power consumption of current devices.

The International Technology Roadmap for Semiconductors (ITRS) [7] maps out the pace of future CMOS miniaturization and estimates that feature size and voltage scaling can continue for one or two decades, before reaching its absolute lower limit. Even with the scaling limits approaching, CMOS is still a very viable technology with several strategies for future improvements. On the MOSFET level, specialized field-effect transistors (FETs) for specific applications could be used, possibly on the same chip. For example, if speed is paramount then transistors with short switching times but high leakage, and therefore high power consumption, can be employed. Conversely, for power-conscious applications, slower transistors with larger feature sizes but less leakage would be preferable [6]. On a higher level, architecture and circuit design could—and this is already done to some extent—work around the changed electronic characteristics of downscaled devices. For manufacturing, higher parallelism in fabrication, e.g. larger wafers, could cut down costs. More clever packaging, for example by stacking circuits on top of each other, could increase device density further. Lastly, the integration of different and complementary technologies with CMOS directly on the chip holds significant promise for future applications. Combining CMOS circuitry with optical devices, such as waveguides, detectors, light-emitting diodes (LEDs), and Lasers, or radio frequency, or micro-electro-mechanical systems (MEMS), to name just a few possibilities, would all yield devices with richer functionality. Eventually, however, merely pushing CMOS further will not be enough, and, consequently, considerable effort has been put into the search and development of completely new computing paradigms that could one day replace CMOS technology. Even if an emerging new computing technology could not compete with CMOS in all aspects, it could, conceivably, be used for specific applications, e.g. memory, and thus complement traditional circuitry.

There is no shortage of ideas for novel computing principles and architectures to replace or complement the existing technology [6, 8]. Broadly speaking, these ideas fall into three categories. First, some device proposals seek to incrementally improve the MOSFET. They might exploit better materials, or be based on other physical principles internally, but show the same characteristics and outside functionality as the transistor. They would be a drop-in replacement for MOSFETs, and the computing architecture would remain otherwise unchanged. Second, devices have been suggested that implement Boolean logic but use

different physical properties to store and communicate the binary state and might, as a consequence, allow different architectural designs that better and more efficiently exploit their specific characteristic properties. Lastly, some ideas explore the radical departure from the existing computing architecture. They do not necessarily strive to realize Boolean logic and include examples such as quantum computing and neuromorphic computing, that is, computing based on neural networks or otherwise inspired by nature [9–11]. These proposals are at various stages of development. Some are only concepts, others have seen extensive numerical studies, and others still have been realized experimentally. However, none of the ideas for novel computing architectures is anywhere close to becoming a mature technology that could rival CMOS, and there is also no obvious candidate that could be pushed forward as the single most promising future technology.

Devices implementing Boolean logic can be characterized by the physical property—the computational variable—used to represent binary state, as well as input and output [12]. For example, the MOSFET uses charge on the oxide capacitor as its state variable, but voltage for input and output. Other computational variables include electronic or atomic spin, used in spintronic and nanomagnetic devices, position, used in some micro-electro-mechanical approaches, or the electric dipole moment, used for ferroelectric systems. For Boolean logic devices, binary switches with characteristics similar to the transistor are usually required, such as gain, non-reciprocity, i.e. no feedback from the output to the input, and the ability to chain the switches. Similarly, benchmarking often concentrates on switching time and energy, as well as device density. However, if the proposed architecture is sufficiently dissimilar to CMOS, then these metrics and requirements become less applicable. As an example, the requirement of non-reciprocity can be circumvented by introducing clocking schemes; switches with more than two inputs could potentially perform logic operations differently, or multiple operations at the same time.

Different materials are being explored to improve the characteristics of the existing field-effect transistor. For example, III-V compounds such as InAs can be used for the channel of the transistor to increase electron mobility and hence switching speeds. Similarly, making the channel a carbon nanotube achieves nearly ballistic transport, and these devices are then called carbon nanotube field-effect transistors (CNTFETs). As another example, tunnel-junction field-effect transistors may be used to realize binary switches [6,12]. For most of these approaches, however, accurate and reproducible manufacturing, the integration with silicon and, not least, the upscaling of fabrication pose severe challenges. A different route is pursued by replacing the electronic binary switches with micro-mechanical

switches, while still using the same conventional computing architecture. Micro-electro-mechanical (MEM) relays are relatively slow, but provide negligible leakage currents and are easy to manufacture, making them attractive for ultra-low-power applications, such as environmental sensing logic [13]. Prototypical MEM circuits have been experimentally demonstrated [14]. Further removed from CMOS circuitry are spintronic devices, which use the spin degree of freedom to encode binary information [15]. Device proposals cover a wide range of ideas of how the spin is used, stored, and interfaced with. For example, domain wall devices represent bits by magnetization domains in ferromagnetic wires forming a network. The domain walls are propagated through the wire and junctions and other geometrical layouts implement logic functions. The wire’s magnetization can then be sensed with a magnetic tunnel junction [16]. Spin wave devices encode information in the phase of spin waves, which interfere constructively or destructively at junctions, and multiple signals at different frequencies can potentially be processed in parallel [17, 18]. All-spin logic devices are yet another proposed technology that stores binary state in nanomagnets which communicate with spin-polarized currents. For logic functionality, a majority gate has been proposed where spin-polarized currents mix and the majority spin polarization wins and sets the output [19, 20].

Quantum-dot cellular automata (QCA) is a beyond-CMOS computing paradigm that is a more radical departure from conventional CMOS circuit design than most of the approaches discussed so far [21]. The binary state is encoded as a bistable charge distribution—electric dipoles—in a cell consisting of several quantum dots. Cells interact through electrostatic forces in a fashion similar to a cellular automaton, where each cell’s state is dominantly set by its closest neighbouring cells. The device functionality is determined by the geometrical arrangement of the cells. For example, cells placed next to each other in a horizontal line can transport a signal and therefore function as a wire [22]. Three input cells placed as closest neighbours to a fourth cell vote on that cell’s state, and the majority wins. This majority gate is used to realize AND and OR logic; a different geometric arrangement implements an inverter. *A priori*, the information flow in quantum-dot cellular automata is not directional. Rather, the computation process can be understood as perturbing the system out of its ground state by setting external inputs, where the device then dissipatively propagates to its new ground state, which corresponds to the computational solution of the problem the circuit was designed to solve. The approach is current-free and promises extremely low-power operation. On a higher level, to design large-scale QCA circuits, directionality in information flow is enforced by introducing a clocking scheme [25].

Quantum-dot cellular automata are the subject of this thesis.

The underlying idea of QCA—bistable interacting cells—is quite versatile and can be recast in different physical domains. For example, within the last decade the possibility of molecular QCA implementations has been explored [26,27]. Cells would be comprised of molecules instead of quantum dots and these molecules have to allow for bistable electron charge distributions. Due to their molecular scale, these devices promise to operate at room temperature and allow extremely high device densities. Molecular electronics offers the prospect of efficient self-assembly. However, a molecular QCA scheme also poses some severe challenges: suitable molecules need to be identified, synthesized reliably, attached to a surface and arranged in the desired geometric cell layout. Interfacing input and output with more conventional electronics is likely to be difficult. A second interesting adaptation of the QCA idea is in the magnetic domain. Magnetic quantum-dot cellular automata (MQCA) [28,29], occasionally referred to as nanomagnetic logic (NML) [6], employ bistable nanomagnets as cells which are coupled through magnetic instead of electrostatic fields. MQCA works at room temperature, promises very low power dissipation, and is non-volatile. Lines of cells, the majority gate, and clocking have all been demonstrated experimentally [30–32].

For the original QCA scheme—sometimes referred to as electrostatic quantum-dot cellular automata (EQCA) to distinguish it from the molecular and magnetic variants—a number of systems have been explored for experimental implementation. Lent *et al.* demonstrated the first experimental QCA cell in 1997 in a metal-island system [33]. The quantum dots were realized as tunnel-coupled aluminum islands of micrometer size at millikelvin temperatures, and the bistable nature of the cell was observed. Experiments were then extended to demonstrate binary wires (two cells), majority gate operation (a single cell with three inputs), and a shift register (consisting of six dots) [34–36]. Single QCA cells have also been implemented in GaAs / AlGaAs heterostructures, ion-implanted phosphorus-doped silicon, and, most recently, on a hydrogenated silicon surface [37–39]. On the hydrogenated silicon surface, individual hydrogen atoms are removed with a scanning tunnelling microscope tip. The remaining dangling bonds act as quantum dots. These atomic silicon quantum dots are tunnel-coupled when placed close enough together (a few nanometers), at larger distances they interact only via Coulomb repulsion [40]. This silicon-based QCA implementation is particularly exciting, because it promises room temperature operation due to its small feature sizes and large electrostatic energy scales, and potentially easy integration with the existing CMOS technology. The precision and upscaling of the

fabrication capabilities have seen encouraging progress recently [41].

On the theoretical side, the building blocks of QCA circuitry, such as the single cell or a line of cells, have been characterized and the dynamical behaviour of larger systems such as gates has been studied [22, 42]. Importantly, the cell-cell response—the switching behaviour of a cell with respect to an input cell—was found to be non-linear and exhibit gain, two of the main requirements for building traditional CMOS-like integrated logic circuits. If that is indeed true, then lines of cells are always fully switched and fanout and concatenation of devices do not pose difficulties. Clocking schemes have been introduced to improve the reliability and speed of QCA computations and, starting from the basic building blocks, more complex circuits like shift registers, adders, and memory have been explored [25, 45, 46]. A circuit design and simulation program exists, which treats the QCA system with a high level of abstraction and strongly idealized cells [47].

Numerical work on QCA typically starts from an extended Hubbard model. However, because the full quantum mechanical problem becomes computationally intractable very quickly even for small systems, two ubiquitous approximations are employed: the inter-cellular Hartree approximation (ICHA) and the two-state-per-cell approximation [21, 42]. Crucially, even though there are plausibility arguments to motivate their use, neither of these approximations has been rigorously validated. The ICHA approximation in particular is problematic: as a mean field scheme ICHA should be expected to over-emphasize charge-density-wave order in low-dimensional structures and therefore potentially yield results that are too optimistic regarding the operational range of the devices. To our knowledge, almost all previous efforts to characterize QCA building blocks rest on ICHA, and there is a danger that the whole emerging physical picture of the QCA approach is coloured by the particularities of this mean field approximation. Recently, Taucer *et al.* explicitly identified the need to go beyond the ICHA approximation [48]. Concentrating on system dynamics, they showed that ICHA yields quantitatively and qualitatively wrong results. QCA was found to be more fragile than previously predicted. Although it has been argued that in practical systems, quantum decoherence would stabilize QCA [49], the fact remains that the approximation underlying most theoretical work on QCA is not well understood and known to be qualitatively wrong in some cases.

In this work we undertake a thorough and rigorous numerical study of the electrostatic QCA approach. We do not attempt the quantitatively accurate modelling of a specific material system, but aim for the generic, semi-realistic description of QCA devices. Starting from the extended Hubbard model and using exact diagonalization, we do away with the



ICHA approximation. Instead, we introduce two controlled Hilbert space truncations, the fixed-charge and the bond model, whose limits we study and understand. We derive the two-states-per-cell model—which is equivalent to a transverse-field Ising model—and show the limits in which it is an appropriate description of QCA systems. Restricting ourselves to time-independent properties, we concentrate on a few simple building blocks of QCA—the cell and a line of cells—but aim to characterize them in as detailed and unbiased a way as possible. Remarkably, even for these very simple QCA systems, we already find notable differences to previously published results. In particular, the cell-cell response is *linear* and does not exhibit gain. This has profound consequences and essentially changes the whole physical picture of QCA. We explore the systems’ characteristics over a wide range of parameters and establish minimal requirements for QCA operation as well as parameters for optimal performance. Using the two-states-per-cell model in a tightly controlled parameter regime, we briefly investigate wires of up to twelve cells in length and the majority gate.

The following chapter introduces the QCA approach in detail. We explain the basic idea, logic gates as the building blocks of QCA circuitry, and the clocking of larger devices. As an example experimental system, we discuss atomic silicon quantum dots, which we use as a reference throughout the thesis. We then dive into the modelling of QCA systems, and specifically the extended Hubbard model which we use as our starting point. Previous theoretical results are presented, along with a more detailed explanation of the intercellular Hartree approximation. We conclude the chapter with a brief overview of our exact diagonalization implementation. Chapter 3 focuses on the approximations we use. Two Hilbert space truncations are introduced, the fixed-charge model and the bond model. We then derive an Ising-like model—the two-states-per-cell approximation—as an effective low-energy model from the bond Hamiltonian. This derivation will already yield some insights into the characteristics of the QCA paradigm. The last part of the chapter goes into great detail to understand how the approximations work and in which regime they are valid. The fourth chapter presents the numerical results from our study. We use a three-cell wire as an exemplary QCA system to investigate its basic characteristics. We then employ an extended “cluster” mean field scheme in an effort to establish lower boundaries for workable QCA system parameters. Using the Ising model for lines of up to twelve cells, we identify a set of parameters where the QCA approach works well and put those parameters into context by contrasting them with corresponding parameter estimates for the atomic silicon quantum dots. The chapter concludes with a brief numerical exploration

of the majority gate. The last chapter summarizes our results and offers a perspective on future directions for research on the QCA approach.

## Chapter 2

# Quantum-dot cellular automata

### 2.1 An alternative computing paradigm

Lent *et al.* introduced the concept of quantum-dot cellular automata (QCA) as an alternative computing paradigm in 1993 [21]. They devised a novel physical scheme to build digital circuits that would overcome some of the limitations of complementary metal-oxide-semiconductor (CMOS) technology, promising potentially lower power consumption, higher device density, and faster clocking. As the name suggests, quantum-dot cellular automata are made from quantum dots that are grouped into cells. Figure 2.1(a) shows a basic QCA cell in which four quantum dots are arranged on the corners of a square. The dots are idealized as highly localized single orbitals that are perfectly decoupled from some non-intrusive medium or substrate. Because of the Pauli principle, each dot can be occupied by zero, one, or two electrons. In the QCA scheme, however, each cell is occupied by exactly two electrons, and each constituent dot is quarter-filled on average. The electrons tunnel only weakly between different dots in a cell, and the dominant energy scale is the Coulomb repulsion between the particles. Because of the large energy cost to two electrons occupying the same site or adjacent ones, the diagonal states are the two energetically preferred electron configurations. In comparison, edge states or doubly occupied quantum dots are unfavourable higher energy states, see Fig. 2.1(b). The two diagonal states can be identified with logic 0 and 1, respectively. *A priori* the two bit encodings have the same energy, but this degeneracy can be lifted by an external Coulomb potential, arising, for example, from a second nearby QCA cell.

A single cell by itself is not very interesting. But multiple cells can be positioned next

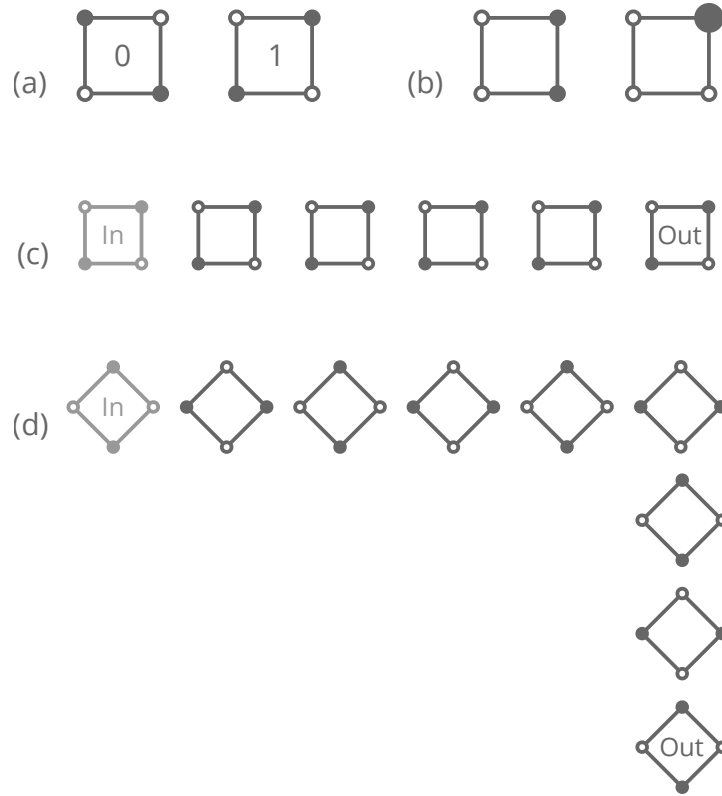


Figure 2.1: Building blocks of quantum-dot cellular automata (QCA). (a) A QCA cell consists of four quantum dots on the corners of a square and is occupied by two electrons. Due to Coulomb repulsion, two energetically preferred states emerge, logic 0 and logic 1. (b) Both electrons occupying the edge of the cell or doubly occupying a single quantum dot are unfavourable high-energy states. (c) A straight line of cells functions as a wire and transmits a signal. (d) A diagonal line of cells (cells rotated by  $45^\circ$ ) transmits a signal alternating from cell to cell. Wires can have kinks.

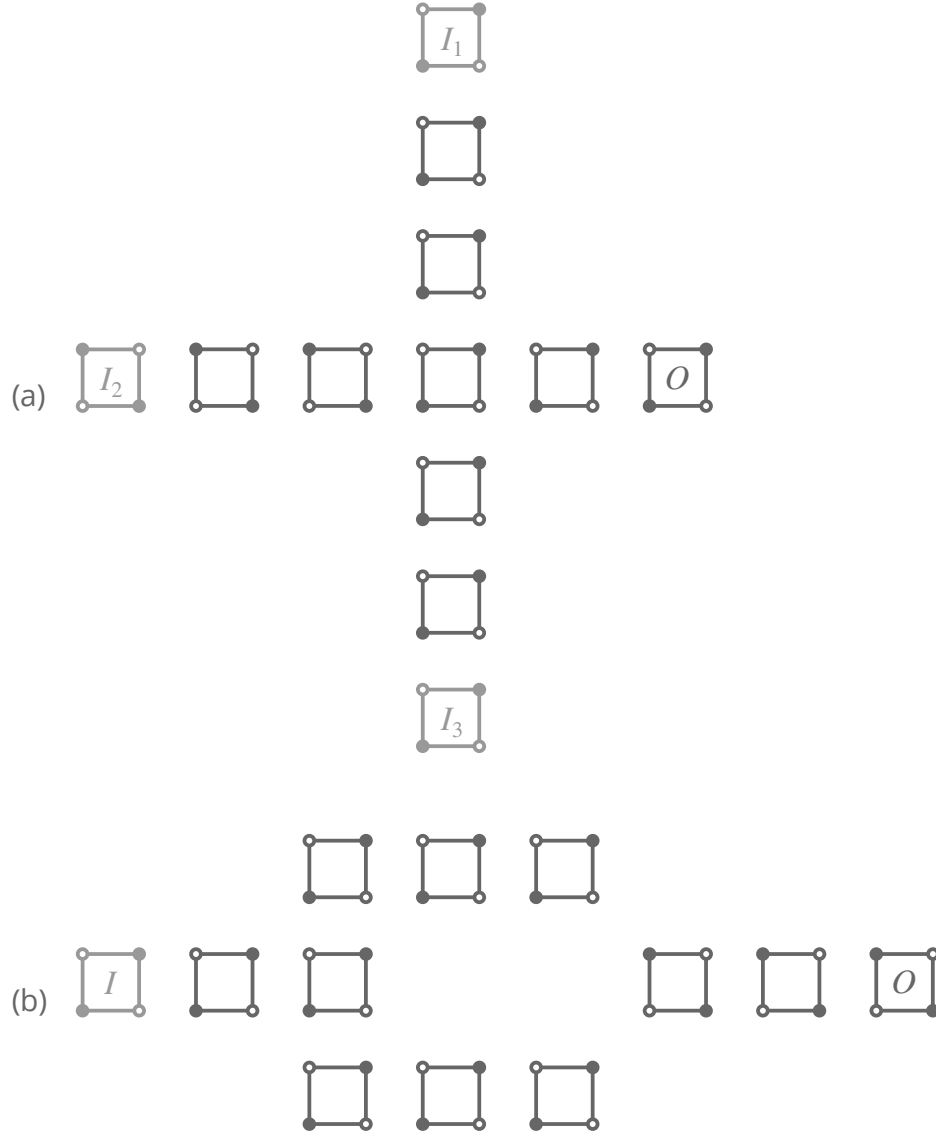


Figure 2.2: QCA gates. (a) The majority gate's three inputs "vote" on the output. The gate is commonly operated with one fixed input, for example  $I_3$ , and then functions as an AND ( $I_3 = 0$ ) or OR gate ( $I_3 = 1$ ) for the remaining two inputs. Here the gate performs the computation  $1 \vee 0 = 1$ . (b) The inverter performs logical negation, swapping logic 0 for logic 1 and vice versa.

to one another, for example as a straight line of cells, as shown in Fig. 2.1(c). The approach once again assumes that Coulomb forces are strong and that electron tunnelling between cells is very small. For a straight line of cells, the long-ranged, unscreened Coulomb forces will tend to align the electron configurations of adjacent cells. If the first cell is in logic state 1, then the second cell will also prefer logic state 1 and so in turn will all the other cells in the line. The situation is the same for logic state 0. Therefore, a straight line of cells is similar to a wire not only in geometry, but also in functionality: it transmits a digital signal. The same is true, with slight modifications, for a diagonal line of cells—cells rotated by  $45^\circ$ , as illustrated in Fig. 2.1(d). In this case, the signal alternates from cell to cell; that is, logic 1 will follow logic 0 which followed from logic 0, and this again is simply by virtue of the dominant Coulomb interaction between electrons on different cells. By using an even number of cells the diagonal line of cells works as a wire just as well as a straight line of cells. The pictogram also demonstrates a  $90^\circ$  kink for the diagonal line of cells, which our newly gained intuition for these Coulomb-driven systems expects to pose no problem for signal transmission.

The main idea of the QCA approach becomes apparent: ideal, bistable cells interact with each other solely by Coulomb repulsion. By arranging the cells in clever geometries, we can realize interesting functionalities. The idea as such is quite general and does not strictly rely on the two-electron–four-dot cell introduced above. Indeed, a number of variations exist, such as cells consisting of two dots and occupied by only one electron that interact via dipole fields instead of quadrupole fields as for the conventional cells. Another variation is a four-dot cell with six electrons—two holes—instead of two electrons. Even the interaction need not be Coulombic. For example, magnetic QCA schemes have been explored [29]. While QCA carries “quantum” in its name and is sought to be implemented at the nanoscale, the approach operates close to the classical limit. The Coulomb interaction dominates with the tunnelling of electrons serving as a small perturbation, which nonetheless drives the system’s dynamics. The approach is insensitive to the spin degrees of freedom. Let us finally note that QCA is not a cellular automata in a strict mathematical sense, but only by analogy to the idea of cells evolving according to simple rules that depend on neighbouring cells.

One clever geometrical cell arrangement, the majority gate, is shown in Fig. 2.2(a). The gate has three inputs which “vote” on the central cell. The majority wins and sets the single output. The device is commonly operated with one fixed input, for example  $I_3 \doteq 0$  or  $I_3 \doteq 1$ . In the first case, with  $I_3 \doteq 0$ , the device functions as an AND gate for the

remaining two inputs,  $O = I_1 \wedge I_2$ . In the second case, with  $I_3 \doteq 1$ , it is an OR gate with  $O = I_1 \vee I_2$ . The figure shows the gate performing the computation  $1 \vee 0 = 1$ . Now the only missing piece for Boolean algebra is negation,  $O = \neg I$ . We had already seen that simply arranging cells at an  $45^\circ$  angle as in the diagonal line of cells negates the signal from cell to cell. The inverter, shown in Fig. 2.2(b), recasts this idea into a more robust layout. With that we have, at least in principle, all the necessary building blocks for Boolean algebra and thus digital circuitry.

Conceptually, it is most elegant to set the inputs for a QCA circuit via driver cells—cells that resemble the QCA cell in form, but are made up of static point charges instead of quantum dots. These static charges are thought to be manipulable to vary the input smoothly from the logic 0 to the logic 1 state. In Figs. 2.1 and 2.2, these driver cells are represented in light grey. Of course, in practice such driver cells would be difficult if not impossible to implement and the inputs are more likely set by leads that provide the necessary perturbative electrostatic fields. The output of a QCA device can be directly read from its output cells. In practical implementations this will require a non-trivial charge probing apparatus. Changing the input for a QCA device throws the system into an excited, non-equilibrium state. The system will then dissipatively propagate to its new ground state. For the given inputs, this ground state corresponds to the solution of the computational problem the circuit is designed to solve. Let us emphasize this: in QCA, the computational solution maps directly to the physical ground state. While the computation is being performed, only a few charges move locally, in each cell. Operating close to the ground state, QCA is thus a truly current-free approach and consequently inherently low-power, especially when compared with CMOS technology. But the operation close to the ground state also raises concerns for the operational temperature for these devices. It is clear that for real-world applications we would want to engineer the system so that the energy gap between the ground state and the low-lying excited states far exceeds room temperature. Different material systems provide different dissipative channels, and modelling them quantitatively or even qualitatively correctly is very challenging. As a consequence, it is difficult to derive general expectations for the clocking speed of QCA circuits. The switching speed of a majority gate, for example, will greatly depend on the system's parameters, but particularly on the nature of the dissipative coupling of the circuit to its environment. A small dissipative coupling will have the output polarization oscillating before it eventually settles to its correct value. A very dissipative system in contrast might get stuck in meta-stable states.

QCA circuits consist of wires, gates, and other structures arranged on a two-dimensional surface—very similar to conventional electronics devices. However, the structures themselves are quasi-one-dimensional, and this poses a challenge for building large-scale QCA circuits. A good example is a single long wire, which is truly one-dimensional. When we think about switching the input for the wire, we think of the information being propagated as a charge density wave along the line of cells, or, equivalently, as propagating the domain boundary between logic 0 and logic 1. This domain boundary incurs an energy cost that the system seeks to minimize, causing the wire to order. For an increasingly longer wire, however, the gain in entropy for moving a domain boundary freely throughout the wire ( $S \sim \log N$ ,  $N$  the number of cells) soon exceeds the loss in energy, which is reflected by the free energy of the system ( $F = U - TS$ ). Quite generally, a one-dimensional system with discrete (rather than continuous) degrees of freedom cannot be ordered in the thermodynamic limit except at zero temperature. Therefore, the finite-temperature, infinitely long wire will always exhibit exponentially decaying bit correlations and thus be unable to transmit a signal. The gap between the first excited state—with two domains—and the completely ordered ground state, together with the desired operational temperature will determine the maximum system size.

To address this scaling problem, we partition large circuits into smaller units. The size of each unit is chosen to be small enough to avoid entropy-induced disorder at a given operational temperature. Each unit can be turned “on” and “off” separately: ideally, individual gates would allow one to effectively raise and lower the tunnelling barriers between quantum dots in each unit and thus provide a mechanism to freeze or delocalize the electrons. A unit with *frozen* electrons can serve as the input for a unit with more *active* charge carriers, which works like a regular QCA circuit. A unit with completely *delocalized* electrons, in contrast, will not influence adjacent units. By putting each unit through the three phases *delocalized*, *active*, and *frozen* and synchronizing adjacent units appropriately, we can control the information flow through the system very nicely, as illustrated in Fig. 2.3. Therefore, by partitioning the circuit and introducing a clocking scheme, we not only handle the scaling problem but also arrive at a pipelining architecture. If and how the tunnelling barriers can be effectively modified will depend on the details of the specific QCA implementation. Also, in practice the QCA circuit units cannot be too small as they must be individually addressable. Gates which turn QCA units “on” and “off” provide another potential benefit as well. We are able to control how and especially how fast the gate voltage is changed and should be able to tune it with respect to the inherent



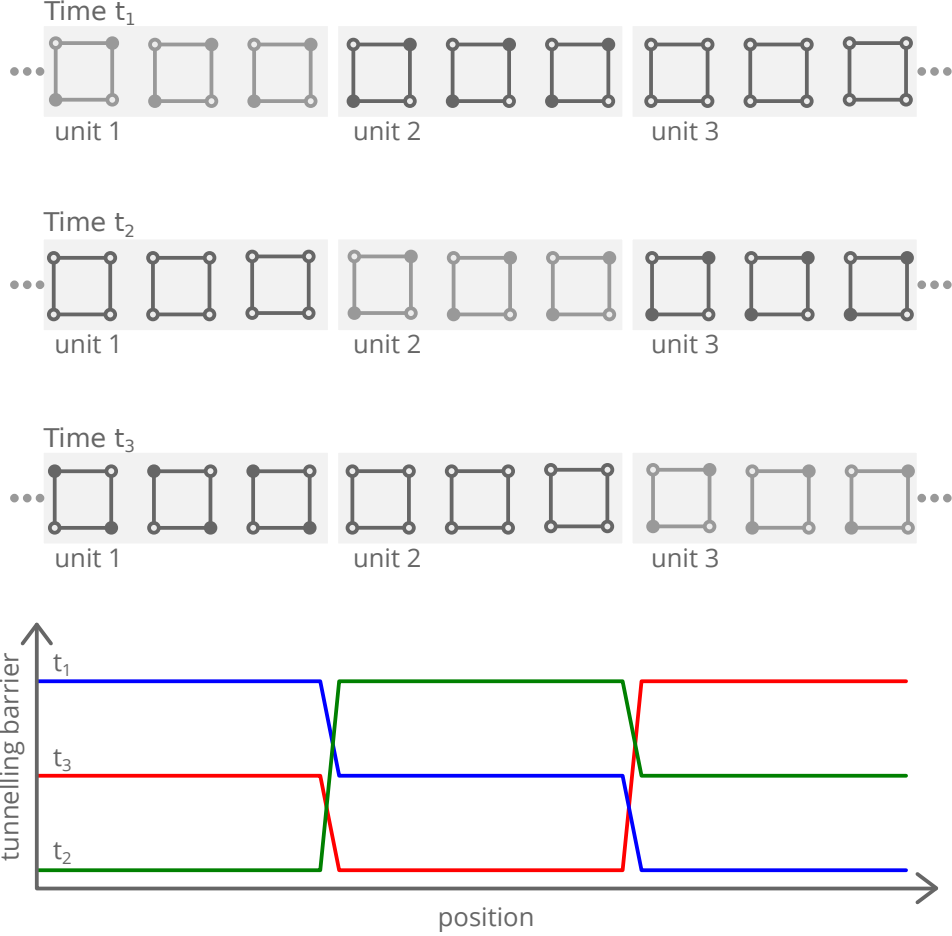


Figure 2.3: Clocked QCA for a line of cells. To avoid entropy-induced disorder in large QCA circuits, the system is partitioned into smaller units, labelled 1, 2, and 3 in this example. By varying the tunnelling barriers, each unit is put through the three phases *frozen* (high barrier, light grey cells), *active* (medium barrier, dark grey cells), and *delocalized* (low barrier, dark grey cells with empty dots). Synchronizing the phases of adjacent units allows to pipeline information flow and computations. The line of cell's three units and their tunnelling barriers are shown at three different times,  $t_1 < t_2 < t_3$ . A logic 1 state is propagated from the left to the right. At  $t_3$  a logic 0 state is coming in from the left.

time scales of the QCA system, which are set by the system’s parameters and the dissipative coupling to its environment. This should afford a better control over the dynamics of the switching process and might help mitigate problems such as oscillating outputs and meta-stable states, mentioned above [25].

## 2.2 Atomic silicon quantum dots

Our objective is the general, rather than implementation-specific, characterization of the QCA approach. Even so, it is still important to consider concrete experimental realizations, not only as a motivation for our work, but also to put our modelling and results into context. One of the most promising and recent experimental implementations of QCA is based on atomic silicon quantum dots [39–41], and we will therefore use them as our experimental reference. Atomic silicon quantum dots were first demonstrated as a possible QCA implementation by Wolkow *et al.* in 2009, when the group first constructed a single QCA cell. Figure 2.4(a) shows a scanning tunnelling microscope (STM) image of their device. Since then impressive advances have been made both in the understanding of the electronic properties of these quantum dots as well as in the precise fabrication of larger QCA structures. With atomic-scale feature sizes, this experimental system promises room temperature operation, while at the same time tapping into the established and highly sophisticated silicon technology. Being based on silicon should also ease integration with existing CMOS circuitry.

Atomic silicon quantum dots are *dangling bonds* on a hydrogen-terminated (100) silicon surface. Atoms on a (100) silicon surface have two unsatisfied bonds. Pairs of surface atoms form dimers, satisfying one bond. The remaining bond is satisfied by passivating the surface with hydrogen. Figure 2.4(c) shows a STM image of the reconstructed silicon surface, where the dimer rows are clearly visible and the dimensions are indicated. By applying a relatively large current through the STM tip, individual hydrogen atoms can be removed, with atomic precision. This leaves a *dangling bond (DB)* that acts as a quantum dot: energetically, electrons on the DB orbital sit in the silicon band gap and are therefore decoupled from the silicon substrate. Figure 2.4(b) shows the band diagram of a DB on an n-doped substrate. Chemically, DBs have proven to be surprisingly robust with respect to environmental molecules. From *ab initio* calculations it is known that the  $sp^3$  DB orbital extends predominantly into the bulk and only a little into the vacuum. The orbital’s lateral extent is on the order of 1 nm and therefore spans multiple silicon lattice atoms.

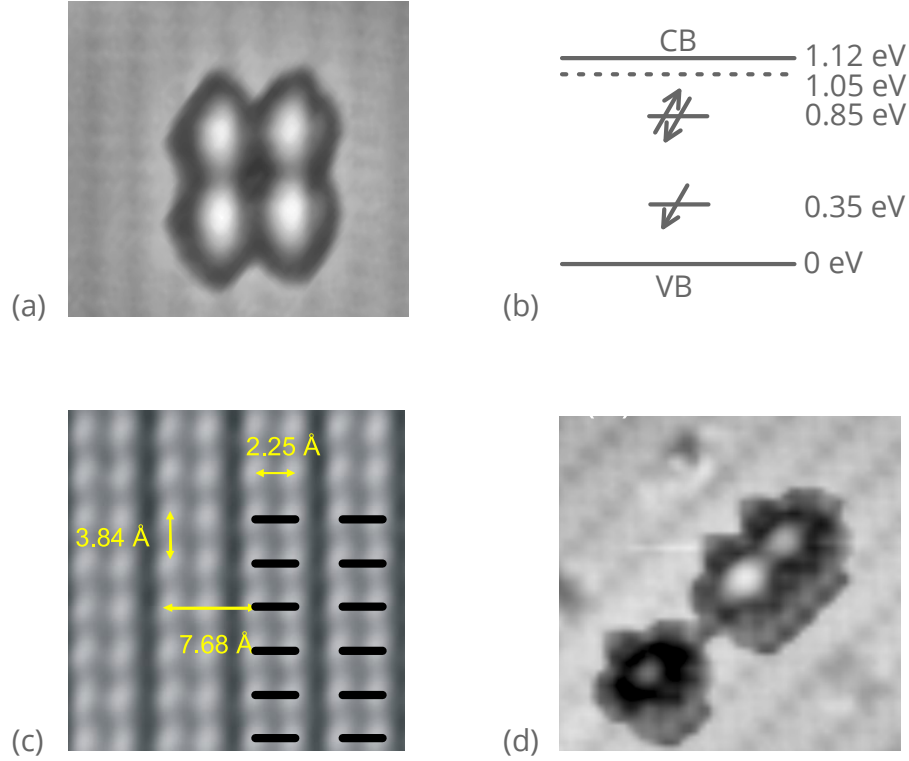


Figure 2.4: Atomic silicon quantum dots are *dangling bonds (DBs)* on a hydrogenated (100) silicon surface. (a) A scanning tunnelling microscope (STM) image of an atomic silicon quantum dot QCA cell. (b) Band diagram of a DB on a strongly n-doped silicon substrate. (c) The reconstructed (100) hydrogenated silicon surface, showing dimer rows. (d) Two closely spaced tunnel-coupled DBs perturbed by a third DB. The top right DB is seen to be more negatively charged than the other DB of the closely spaced pair, due to Coulomb repulsion from the perturbing third DB in the bottom left. All STM images and *ab initio* estimates from Wolkow *et al.* [40,41].

Due to orbital overlap, closely spaced DBs are tunnel-coupled. A neutral DB consists of the positive silicon ion and one electron. In the experimentally common strongly n-doped system, the DB accepts one more electron and is therefore  $-1e$  negatively charged. Conversely, in a p-doped system the DB will donate its electron and become  $+1e$  positively charged. The Coulomb repulsion between negatively charged DBs can be used to adjust the filling of DB assemblies simply by controlling the DBs' positions. For example, on an n-doped substrate two DBs may eject one electron (which goes back to the bulk) and share the remaining single electron, when placed close enough together. To prove this, a third DB is placed close by, but not close enough to be tunnel-coupled. The effect of the Coulomb repulsion can be seen via STM imaging, Fig. 2.4(d), where the DB farthest from the perturbing external charge is more negatively charged (darker in the STM image) than the closer DB. The observed charge shift is only possible when both closely-spaced DBs share a single electron. To form the previously shown QCA cell, Fig. 2.4(a), on a strongly n-doped silicon substrate four DBs are brought close enough together so that two electrons go back to the bulk, leaving the cell with six electrons (two holes) in total and a cell net charge of  $-2e$ , which is the right charge regime for QCA.

Atomic silicon quantum dots provide some examples of how a real world system might be different from the idealized picture we typically employ to describe the QCA approach. We like to think of quantum dots as highly localized orbitals. But in the silicon system the orbitals of the DBs actually span multiple lattice sites and only if the DBs are placed far enough apart might we still be able to consider them as localized. We do not consider the substrate but treat quantum dots as perfectly isolated entities. Of course, in practice the substrate will certainly influence the QCA device. In the silicon system, free charge carriers will screen the long-ranged Coulomb interactions that the QCA scheme relies on, although likely on scales larger than the circuit feature size. The screening—which to some extent should be controllable via the doping—is not necessarily disruptive for QCA and might even be beneficial, for example by minimizing charge buildup in large systems. But to quantify the screening accurately it is necessary to thoroughly understand and precisely model the system; for atomic silicon quantum dots, which live at the surface, that would surely be very challenging. The silicon substrate could also, conceivably, provide a second tunnelling channel between DBs. In addition to electrons hopping directly from DB to DB they could first tunnel from DB to substrate and then back to another DB. Therefore, an accurate model for atomic silicon quantum dots might need to accommodate the nature of the DB orbitals, screening, multiple tunnelling channels, and possibly other phenomena.

As we are aiming at a general description of QCA devices, we will not include any of these effects in our model.

## 2.3 The extended Hubbard model

QCA systems are typically modelled by an extended Hubbard Hamiltonian. The Hubbard model originated in the early 1960s to describe rare-earth systems with highly localized d- and f-electrons and has since then, of course, become one of the most widely studied and successful models in condensed matter physics [50]. In basing our description on the Hubbard model we already put some key assumptions in place. For example, we assume that the quantum dots are similar to the highly localized d-orbitals. As discussed above, depending on the particular QCA implementation this might or might not be a good description. However, our interest is not in the precise details of any particular material system; rather, our aim is to investigate universal characteristics of QCA systems. As long as a QCA system can be broadly qualitatively described by Hubbard physics—and most prospective QCA implementations fall into this category—our modelling and findings should be valid. Conversely, for implementations that are decidedly not Hubbard-like, our results might not be applicable. An idealized but semi-realistic description is what we want and for that the Hubbard model is indeed an appropriate—and tractable—starting point. Specifically, the Hamiltonian we use is

$$\begin{aligned}
H = & - \sum_{ij\sigma} t_{ij} c_{i\sigma}^\dagger c_{j\sigma} + U \sum_i n_{i\uparrow} n_{i\downarrow} - \mu \sum_{i\sigma} n_{i\sigma} \\
& + \sum_{i<j} V_{ij} (n_{i\uparrow} + n_{i\downarrow} - q) (n_{j\uparrow} + n_{j\downarrow} - q) ,
\end{aligned} \tag{2.1}$$

where  $c_{i\sigma}^\dagger$  ( $c_{i\sigma}$ ) creates (annihilates) an electron on quantum dot  $i$  with spin  $\sigma$  and the particle number operator is  $n_{i\sigma} = c_{i\sigma}^\dagger c_{i\sigma}$ . The overlap integral between dots  $i$  and  $j$  is denoted by  $t_{ij}$ ,  $U$  is the Hubbard on-site Coulomb repulsion,  $\mu$  the chemical potential, and  $V_{ij}$  the long-ranged Coulomb interaction, which is characteristic for QCA systems. For simplicity the Coulomb term is chosen to be  $V_{ij} = \frac{1}{r_{ij}}$  where  $r_{ij}$  is the distance between the two dots  $i$  and  $j$ . We also introduce the *compensation charge*  $q$  which is thought to represent a possible positive ion at each quantum dot site. This constant positive charge allows us to tune the net cell charge. For two electrons per cell, for example,  $q = 0$  yields a net cell charge of  $-2e$  whereas  $q = \frac{1}{2}$  represents zero net cell charge. The  $q = \frac{1}{2}$  charge

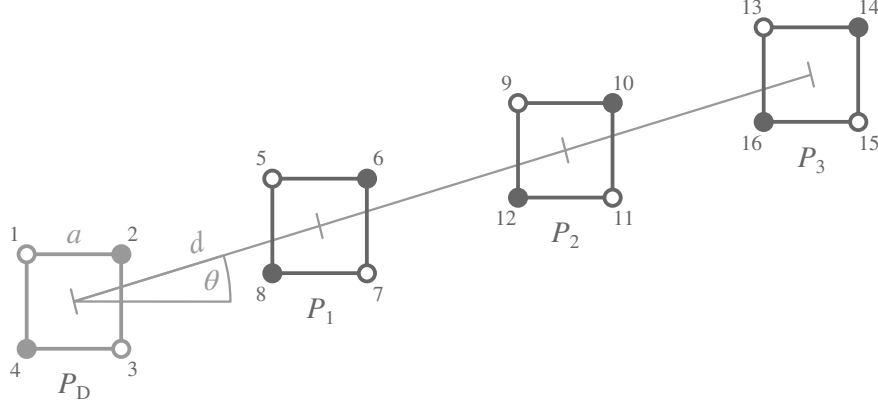


Figure 2.5: Parameterizing a three-cell QCA wire. The quantum dots are numbered clockwise for each cell and consecutively from cell to cell. The edge length of a QCA cell is denoted by  $a$ , the cell-cell distance by  $d$ , and the cell-cell angle by  $\theta$ . The wire's input is set by the driver cell's polarization  $P_D$ , the active cells' polarizations are  $P_1$ ,  $P_2$ , and  $P_3$ .

neutral cells are perfect electrostatic quadrupoles.

The geometric layout of the QCA system and therefore its functionality is encoded in the hopping parameter  $t_{ij}$  and the long-ranged Coulomb term  $V_{ij}$ . For the hopping parameter, we usually only consider nearest-neighbour hopping  $t$  and specifically no hopping between the cells. While this constraint is not strictly necessary for QCA, it is in line with the approach's underlying idea and greatly simplifies calculations. Because the overlap integral decays exponentially with distance, as long as the distance between dots from different cells is larger than the distance between dots within one cell, the assumption will introduce only a small error. Still, this is something to keep in mind if we place cells very close to each other. Note that without inter-cell hopping we can decompose the Hamiltonian into purely Coulombic cell-cell interaction terms  $H_{kl}^{cc}$  and single cell terms  $H_k^c$ , which capture the kinetics as well as the inside-cell Coulomb interactions,

$$H = \sum_k H_k^c + \sum_{k < l} H_{kl}^{cc}, \quad (2.2)$$

where  $k$  and  $l$  number the cells.

To parameterize the Coulomb term  $V_{kl}$  and specifically  $r_{ij}$ , the distance between quantum dots  $i$  and  $j$ , we introduce the cell edge length  $a$  and the cell-cell distance  $d$ , as illustrated in Fig. 2.5, where we have used a short line of cells as an example QCA system.

The angle between adjacent cells is denoted by  $\theta$ . Ideally each cell should be in logic state 0 or logic state 1, but, of course, in practice a cell can be in any superposition of the two states or even in a different state altogether. The *cell polarization*  $P_k$  quantifies the state of the cell,

$$P_k = \frac{1}{2} (n_{4k+2} + n_{4k+4} - n_{4k+1} - n_{4k+3}) , \quad (2.3)$$

where the dots in each cell are numbered clockwise as indicated in the figure. We have also introduced the shorthand notation  $n_i = n_{i\uparrow} + n_{i\downarrow}$ . The cell polarization is  $P_k = -1$  for a logic 0 and  $P_k = +1$  for a logic 1 state. Without any external input the polarization of a cell will be  $P_k = 0$ . In the example line of cells, the input is set via the driver cell's polarization  $P_D$  at the left end. The driver cell's four static point charges are adjusted to reflect the desired polarization  $P_D$ . For QCA, the cell polarization really is the observable of utmost interest. It indicates whether a cell is more in logic state 0 or logic state 1 and how polarized the cell is, where ideally it should always be fully polarized,  $|P_k| = 1$ . In short, the cell polarizations will indicate how well the QCA approach works for a given system and, unsurprisingly, calculating cell polarizations for various geometric layouts over a wide range of system parameters will be our main focus.

The QCA cell is characterized by three energy scales: the nearest-neighbour hopping  $t$ , the nearest-neighbour Coulomb repulsion  $V_1 = \frac{1}{a}$ , and the on-site Coulomb repulsion  $U$ . For QCA operation,  $U$  is usually assumed to be large enough that doubly occupied states are gapped out. We can introduce  $V_0 = \frac{1}{\sqrt{2}a}$ , the energy scale for next-nearest-neighbour Coulomb repulsion, which is realized when both electrons sit diagonally at opposing corners of the cell—our preferred  $P_k = \pm 1$  states, ideally the ground state. Conversely,  $V_1$  corresponds to both electrons occupying the edge of the cell. Again, for QCA operation we would like the edge states to be sufficiently gapped out. In other words, the energy gap,

$$\Delta V = V_1 - V_0 = \frac{2 - \sqrt{2}}{2} \frac{1}{a} \approx 0.3V_1 \quad (2.4)$$

should be large compared to temperature  $\Delta V \gg T$ , and similarly  $U \gg \Delta V \gg T$ . The competition between temperature  $T$  and  $V_1$  will thus directly influence how polarized a cell is. In addition,  $V_1$ , which seeks to order the cell, will compete with  $t$ , which delocalizes and disorders the electrons. QCA is thought to function in a regime where Coulomb is the dominant energy scale and hopping is a small perturbation: the ratio  $V_1/t$  is large. But it is also clear that if  $V_1/t$  becomes too large, for example by taking  $t \rightarrow 0$ , the system

slows down and eventually freezes, which is rather undesirable for QCA operation as well. In essence we can describe a cell by the ratios  $V_1/t$ ,  $U/t$ , and  $T/t$ . By similarly expressing the cell-cell distance in units of the cell size  $d/a$ , we characterize any QCA system in dimensionless units.

## 2.4 Basic characterization

At the time of this writing, the QCA idea is over twenty years old. Naturally, the fundamental building blocks of QCA circuitry such as the single cell itself, the wire, and the majority gate have been characterized. Interestingly, time-independent properties were investigated relatively briefly and arguably not exhaustively [21–24]. The bulk of the existing theoretical work soon came to focus on system dynamics [42, 43], the building of large-scale computing architectures with the QCA paradigm [25, 44, 45], and specific potential experimental implementations [34–39]. Previous work on the characterization of time-independent QCA properties yielded two main results. First, the cell-cell response, that is, how the polarization of one cell responds to the polarization of a neighbouring cell, was established to be non-linear and exhibit gain [21]. Therefore, even an only partially polarized cell would fully polarize the cell next to it, Fig. 2.6(a). Of course, gain is highly desirable, if not essential, for building digital circuits. It compensates for any loss or imperfections and makes the scheme overall robust. Not coincidentally, CMOS technology is built around the MOSFET transistor with gain as one of its intrinsic properties. Second, lines of cells were seen to be polarized with an almost constant polarization throughout the whole line, Fig. 2.6(b) [22]: apart from a few cells next to the driver cell, all remaining cells in the line would be polarized with the same *saturation polarization*. As a consequence, the output polarization should not depend on the number of cells in the line. The saturation polarization was observed to be largely independent of the driver cell’s polarization, but solely determined by the system’s parameters such as the hopping  $t$  and the Coulomb energy  $V_1$ . For unfavourably chosen parameters, the saturation polarization might be very small, but over a wide range of system parameters it was shown to be close to perfect. For example, for large hopping  $t$ , the saturation polarization is expected to be zero. If  $t$  is then decreased and passes a critical value  $t_c$ , a second-order phase transition takes place. The saturation polarization becomes non-zero and in fact very quickly close to perfect as  $t$  is further decreased. In addition to the cell-cell response and the analysis of a line of cells, larger QCA structures such as the majority gate were reported to function correctly for



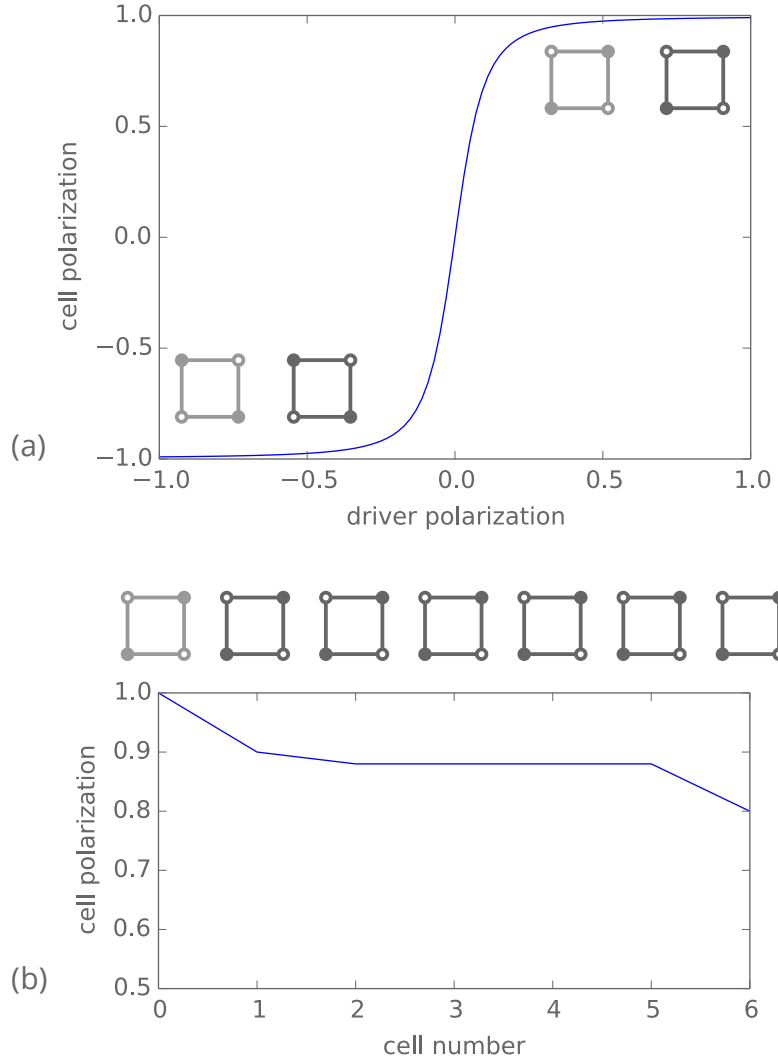


Figure 2.6: Basic characteristics of QCA devices, schematically. (a) The response of a cell's polarization to a driver cell's polarization is non-linear and exhibits gain. This gain has been used extensively to argue for the QCA approach's inherent robustness. (b) Cell polarizations of a six-cell wire with input polarization  $P_D = 1$ , as calculated with the intercellular Hartree approximation. Most cells are polarized with the same saturation polarization and only the leftmost and rightmost cells deviate slightly. In this picture, the output polarization does therefore not depend on the wire length.

a select set of parameters but were not analyzed in depth. Overall, the physical picture emerging from the early time-independent calculations is of bistable cells readily snapping into the correct fully polarized state throughout the whole device. It is a picture where the QCA approach works robustly and in fact almost perfectly over a presumably wide range of parameters. It is the prevailing picture to this day. It is also quite wrong.

These early calculations of time-independent QCA properties concentrated almost exclusively on the ground state of the system (with one exception [23]). However, focusing solely on the ground state is not sufficient. While the QCA approach is intended to be operated “close to the ground state,” at least the first excited state is needed to obtain an estimate for the operational temperature for these devices—a parameter of significant practical interest. More subtly, what the QCA idea calls the ground state actually corresponds to multiple states, namely one spin singlet and three spin triplet states for  $P = -1$  and  $P = 1$ , respectively, in each cell. While these states can reasonably be expected to be near-degenerate, a thorough study of QCA should still consider them. In more practical terms, QCA is expected to operate at finite temperatures, so simulating the devices at non-zero temperature is appropriate. Similarly, the existing work on time-independent QCA properties is not exhaustive with regard to the exploration of other parameters. For example, while the saturation polarization’s dependence on  $V_1$  and  $t$  is roughly mapped out, concrete numerical values for these quantities are hard to come by. In other cases, the Coulomb scale  $V_1$  is not indicated explicitly at all. Cells are assumed to be charge-neutral, but the effects of non-charge-neutrality are not investigated. Different cell-cell distances are not discussed, nor what system parameters should be chosen for optimal performance.

The exact numerical simulation of QCA systems is challenging and in fact intractable for all but the smallest structures. Therefore, approximations are necessary. In the literature on QCA two approximations are prevalent: the intercellular Hartree approximation (ICHA) and the two-states-per-cell approximation [21,42]. Most of the studies of time-independent QCA properties employ the ICHA. Only the cell-cell response is calculated with a “full” quantum mechanical model, where the “full” model is actually already the reduced Hilbert space of exactly two electrons per cell.

ICHA is a mean field scheme: the Hamiltonian of one cell is solved exactly in the mean field of the polarizations of all the other cells. More specifically, the cell-cell interaction

term  $H_{kl}^{\text{cc}}$  in equation (2.2) is rewritten

$$\begin{aligned} H_{kl}^{\text{cc}} &= \sum_{\substack{i \in k \\ j \in l}} V_{ij} (n_i - q) (n_j - q) \\ &\approx \sum_{\substack{i \in k \\ j \in l}} V_{ij} [(n_i - q) (\langle n_j \rangle - q) + (\langle n_i \rangle - q) (n_j - q) + \text{const.}] , \end{aligned} \quad (2.5)$$

and, introducing the mean field for dot  $i$  on cell  $k$ ,

$$\tilde{V}_i^k = \sum_{l \neq k} \sum_{j \in l} (\langle n_j \rangle - q) = \sum_{l \neq k} \mathcal{F}[\langle P_l \rangle] , \quad (2.6)$$

the one-cell mean field Hamiltonian becomes

$$H_k^{\text{MF}} = H_k^{\text{c}} + \sum_{i \in k} (n_i - q) \tilde{V}_i^k . \quad (2.7)$$

Because the cell polarization is directly related to the occupancies of the sites of the cell, we have  $\tilde{V}_i^k = \tilde{V}_i^k(\langle P_l \rangle)$ . Solving the one-cell Hamiltonian allows one to compute the polarization  $\langle P_k \rangle$  of the cell, which in turn is used to set the mean field originating from all other cells. The procedure is repeated until a self-consistent cell polarization and thus self-consistent solution for Eq. (2.7) is found. The standard mean field approximation, with  $n_i n_j \approx n_i \langle n_j \rangle + \langle n_i \rangle n_j - \langle n_i \rangle \langle n_j \rangle$ , was first introduced to study phase transitions. The approximation amounts to neglecting the quantum fluctuations, replacing the dynamical fields with static, effective fields of an averaged strength. Intuitively, a static field causes more order than dynamic, fluctuating interactions and, consequently, mean field calculations generally wrongly overemphasize order in the studied systems. Only at high dimensionality can the neglected fluctuations really tend to zero, and indeed mean field schemes can be shown to become exact in the limit of infinite dimensionality [51]. Conversely, for low dimensional systems fluctuations are more important and mean field approximations are expected not to work well. As an uncontrolled approximation, the validity of a mean field approach has to be verified on a case by case basis. Consequently, because QCA is quasi-one-dimensional, it is arguably not well suited for a mean field treatment. Even then a mean field approximation might be appropriate as a first stab at the problem. But ICHA, having been introduced in the very first QCA paper, was never properly verified or complemented by more accurate methods. It is rather remarkable that a large part of

the existing work on QCA characterization rests, directly or indirectly, on an approximation that can reasonably be expected to give wrong results. And indeed, in the context of the dynamic properties of QCA, it has been known for a long time that ICHA does go wrong [43]. Much more recently, it has been shown very explicitly that even for the single cell-cell response ICHA introduces artefacts that are clearly non-physical [48]. As an intuitive simple example where ICHA will give wrong results we can go back to the infinitely long wire we already discussed above: we argued that due to entropy the infinite wire can only be ordered at zero temperature. In contrast, a mean field approximation will—by construction—predict order up to a finite critical temperature. Additionally, mean field approaches give phase transitions even for finite systems, where, technically and by definition, distinct phases do not exist. For a finite wire, we can only achieve a state that is “ordered enough,” at a given temperature and over a sufficiently long time.

For the calculation of time-dependent properties, the two-states-per-cell approximation is typically used, precisely because it was realized that ICHA is not sufficient, for example to calculate the switching behaviour of some majority gate structures. Perplexingly, in the literature the two-state approximation is motivated and justified by the ICHA picture [42]. Starting from the observation that cells in a wire are polarized with a saturation polarization  $P_{\text{sat}}$ —in ICHA calculations—a cell is represented by two basis states, corresponding to  $P = P_{\text{sat}}$  and  $P = -P_{\text{sat}}$ . In a loose sense, the two-states-per-cell model thus comes from a picture of how we would like QCA to work: perfectly bistable, interacting cells. The approximation has been verified to the extent that it was shown that the ground state of the full quantum mechanical model can be represented nearly perfectly by the two-state basis, but only for one cell and for one particular set of system parameters. In a more rigorous treatment it should be possible to clearly derive the two-state model as the correct emerging low-energy Hamiltonian from the original extended Hubbard model. Such a derivation would also reveal the parameter regime in which the effective two-state Hamiltonian is valid. We will attempt the derivation in due course. In contrast to the ICHA, the two-states-per-cell approximation retains inter-cell entanglement and therefore yields more correct results, not only for dynamics, but also for time-independent properties. This comes at the cost of exponential scaling for the two-state model, whereas ICHA scales linearly in system size. Therefore, even with the two-state approximation only relatively small QCA devices are computationally feasible. As a final note, the two-state model is clearly a close cousin to the transverse field quantum Ising model, where the two polarization states correspond to a pseudo spin and the hopping is like a transverse field, flipping

cell polarizations.

## 2.5 Exact diagonalization

We use the numerical method of exact diagonalization [51] to simulate QCA systems described by the Hamiltonian (2.1). In principle, exact diagonalization is a straightforward method: for a chosen basis the matrix of the Hamiltonian is constructed explicitly and then diagonalized, yielding the eigenenergies and eigenstates of the system. With that we know everything about the system and can calculate observables of interest. The problem is that memory consumption scales as  $N_s^2$  and the computational cost roughly as  $N_s^3$ , where  $N_s$  is the size of the state space; and the number of states scales exponentially with system size,  $N_s = 4^{N_d} = 256^{N_c}$ .  $N_d$  denotes the number of dots and  $N_c$  the number of cells. As an example, to store the full Hamiltonian matrix of a two-cell QCA system requires 3GB of memory, and to store the Hamiltonian matrix of a three-cell system already requires 2000TB. That's clearly not feasible on any available computer. As a side note, we cannot employ projective algorithms such as Lanczos [51], because we are interested in finite temperatures and therefore need the full energy spectrum. Typically, projective schemes are only useful to calculate the ground state or the few lowest energy states.

To decrease the memory requirements and computational cost of exact diagonalization, symmetries must be exploited. The Hamiltonian matrix is actually quite sparse—most entries are zero. By using symmetries and a suitable basis, the Hamiltonian matrix can be brought into block diagonal form and then only those much smaller blocks need to be diagonalized. In our QCA system, the total particle number operator  $N = \sum_i n_{i\uparrow} + n_{i\downarrow}$  and the total spin operator  $S^z = \sum_i n_{i\uparrow} - n_{i\downarrow}$  are good quantum numbers, i.e.  $[N, H]_- = [S^z, H]_- = 0$ . If we now use basis states which are eigenstates of the symmetry operators,  $|n, s, l\rangle$ , with

$$\begin{aligned} N |n, s, l\rangle &= n |n, s, l\rangle , \\ S^z |n, s, l\rangle &= s |n, s, l\rangle , \end{aligned} \tag{2.8}$$

then we have

$$\begin{aligned} \langle n', s', l' | [N, H]_- |n, s, l\rangle &= (n' - n) \langle n', s', l' | H |n, s, l\rangle \stackrel{!}{=} 0 \\ \langle n', s', l' | [S^z, H]_- |n, s, l\rangle &= (s' - s) \langle n', s', l' | H |n, s, l\rangle \stackrel{!}{=} 0 \end{aligned} \tag{2.9}$$

and therefore

$$\langle n', s', l' | H | n, s, l \rangle = 0 \quad \text{for } n \neq n' \text{ or } s \neq s'. \quad (2.10)$$

Consequently, in ordering basis states by the symmetry operators' eigenvalues, the Hamiltonian matrix becomes block diagonal, where the blocks are labelled by  $n$  and  $s$ . The blocks can be constructed and diagonalized separately, and all observables can then be calculated block-wise as well, hence vastly reducing memory requirements and computational time. In our implementation, however, we do keep all blocks in memory simultaneously. This still yields considerably reduced memory usage and the same speedup in computational time. For the QCA system the single largest block is the spin zero sector at half-filling. Its size is

$$N'_s = \left( \frac{N_d}{2} \right)^2. \quad (2.11)$$

This corresponds to memory requirements of 180MB for two cells and 5400GB for three cells. Thus, although this is a considerable improvement for the two-cell system (not least in computational time), the three-cell system still remains unreachable with conventional computer hardware. To access larger systems we need to introduce approximations, which we will pursue in detail and with great care in the following chapter.

Computational physics is, true to its name, to considerable extent concerned with writing computer code. If ingenious algorithms which bring sophisticated physical problems to the computer are the art that excites the computational physicist's intellect, then writing good computer code is the craft. It is a curious fact that traditionally in computational condensed matter physics, little weight has been put on collaboration on the code level, the development of common tools, coding techniques, and the code itself. This not only frustrates the newcomer to the field, for it is a long way from a formally stated algorithm to a correct and efficient implementation, but also poses a more fundamental problem to science in a time when computing has long become an essential part of it. Scientific results obtained from sophisticated numerical algorithms can be difficult to verify and reproduce without an openly available implementation of those algorithms. But verification and reproducibility are core assets of the scientific process. Fortunately, the culture is slowly changing. In computational condensed matter physics, the ALPS and Abinit projects provide open implementations of a variety of commonly used methods and algorithms [52, 53]. In the wider scientific community, IPython is a shining example of building a powerful computational tool collaboratively, with a huge impact across disciplines [54].

Our QCA exact diagonalization implementation is written in C++ and uses the excellent Eigen linear algebra library [55]. Matrices are stored in sparse representation, except for the block-wise diagonalization itself, performed by Eigen, where we use dense matrices. The basis states can be filtered and sorted, for example to truncate the Hilbert space to a specific charge sector and to exploit symmetries. We do not build the Hamiltonian matrix directly, but instead construct creation and annihilation operator matrices. Therefore, operators such as the Hamiltonian and the polarization can be expressed in an intuitive, almost mathematical notation. We employ the “curiously recurring template” pattern to achieve simple static polymorphism, avoiding the overhead of runtime polymorphism [56]. In less abstract terms, this allows us to reuse code, for example the Hamiltonian, for the conceptually similar, but physically quite different various QCA models which we are going to introduce in detail in the next chapter. Our C++ code cannot be executed directly, but is instead compiled as an extension module for the Python language, via the Boost library’s Boost.Python [57]. We also use the unit testing framework from the Boost library. In our experience, making the C++ code available in Python provides enormous benefits. With Python data input, output and storage becomes a breeze, especially compared to the chore these tasks are in pure C++. Python makes it easy to script and distribute (i.e. simply parallelize) simulation runs, and, being well established in the scientific community, comes with extensive libraries for data analysis and plotting, for example SciPy and Matplotlib [58, 59]. Consequently, the integration with Python facilitates quickly trying out new ideas, implementing new features and more fluid data analysis. The advent of the fantastic IPython notebook ties all of these pieces together in a consistent, productive and highly enjoyable workflow [54]. The IPython notebook is also an apt format for effectively communicating results with colleagues. The disadvantages of the Python integration are the additional dependencies, although both Python and Boost are commonly available on any number of platforms these days, and the more involved (and hence error-prone) build process. We have written a small Python library to support our data storage and organization needs. The library facilitates storing and retrieving data in standard file formats and allows to define and run “numerical experiments,” which can be distributed across multiple computers. Both the QCA exact diagonalization code and the Python library are available under an open license on GitHub [60, 61].

## Chapter 3

# Approximations

### 3.1 Fixed charge model

Exact diagonalization scales exponentially with system size. With the full *grand canonical* QCA Hamiltonian (2.1), only devices of up to two cells are computationally feasible. Therefore, we need to introduce approximations to access larger systems. Approximating means to simplify. However, by carefully establishing successive approximations and their limits, we also reduce the problem to its essential ingredients and thus, hopefully, we gain a better understanding of the QCA approach. As a first step, we reduce the Hilbert space to states with a fixed number of particles per cell. We disallow any charge fluctuations, both for the system as a whole and for each individual cell. With that, we omit the chemical potential term in the Hamiltonian,  $\mu = 0$ , and prohibit inter-cell hopping. This is a major simplification. However, it is in line with the QCA idea: the approach requires a fixed number of charges per cell, typically two electrons, and cells are thought to interact only via Coulomb forces. If the *fixed-charge* approximation is not valid for a given system, then there is no hope of implementing QCA on it. For experimental systems like the atomic silicon quantum dots, it should always be possible, at least in principle, to tune the system parameters so that for a given cell layout each cell is occupied by the same number of electrons. The two-electrons-per-cell sector has to be lowest in energy and other particle number sectors need to be sufficiently gapped out, that is, at an energy much larger than temperature. Of course, in practice there are very clear limits as to how much the system parameters can be tuned. Any QCA cell layout considered within the fixed-charge approximation cannot necessarily be readily implemented on a given real-world material



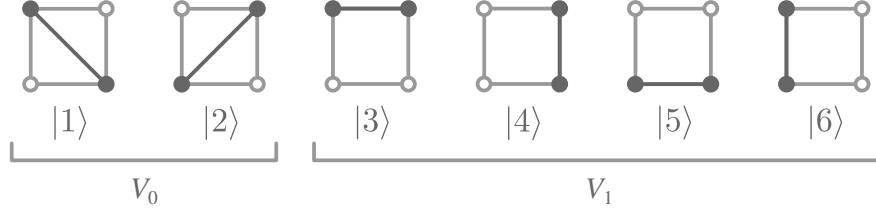


Figure 3.1: The six bonds of a QCA cell. The basis of a QCA cell in the fixed-charge picture consists of six bonds and four doubly occupied dots. Each bond corresponds to one spin singlet and three spin triplet states. The bond model neglects doubly occupied states and keeps only one state per bond for a total of six states per cell. From those, the Ising approximation only retains the two lowest energy states,  $|1\rangle$  and  $|2\rangle$  with energy  $V_0$ .

system.

For the fixed-charge model, the state space scales as  $N_s = \binom{8}{2}^{N_c} = 28^{N_c}$  ( $N_c$  is the number of cells). Using symmetries, the largest block of the Hamiltonian matrix is the spin zero sector, of size  $N'_s = 16^{N_c}$ . On conventional computer hardware, systems of up to four cells are possible, with memory requirements of 32GB. However, such calculations take very long and therefore three-cell systems are the practical limit.

### 3.2 Bond model

At its heart, QCA is a semi-classical idea. It relies dominantly on charge-charge interactions and ignores the particle spin. Therefore, as a next step in our quest to access larger system sizes, we neglect the spin degrees of freedom. The 28 states of each cell in the fixed-charge model can be reorganized into four doubly occupied dots and six bonds, illustrated in Fig. 3.1. Each bond corresponds to one spin singlet and three spin triplet states. The *bond* approximation only keeps one state for each bond and discards the doubly occupied states as well. With the bond model, we thus assume that singlet and triplet states are energetically equivalent and that doubly occupied dots are sufficiently gapped out, that is,  $U \gg T$ . Because the operation of QCA does not rely on the spin, singlets and triplets should behave qualitatively the same—for example, they should yield the same cell polarizations. However, we can speculate that virtual double-occupancy lowers the energies of the singlet states and therefore introduces a small singlet-triplet splitting. Neglecting this small splitting presumably does not introduce a large error, but we will have to verify

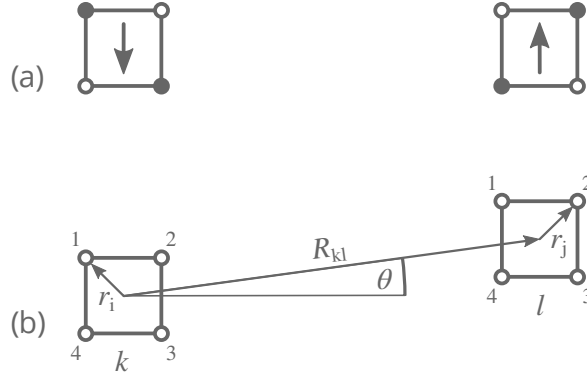


Figure 3.2: (a) The Ising approximation identifies each cell with a pseudo spin. Logic 0 corresponds to spin down and logic 1 to spin up. (b) QCA cells  $k$  and  $l$ .

this assumption and look at the splitting in more detail in due course. For the bond model the QCA Hamiltonian reduces to

$$H = - \sum_{\langle ij \rangle} t c_i^\dagger c_j + \sum_{i < j} V_{ij} (n_i - q) (n_j - q) . \quad (3.1)$$

With six bond states per cell, the Hilbert space of the bond model is  $N_s = 6^{N_c}$  ( $N_c$  the number of cells). Five and six cells are doable, with memory requirements of 460MB and 16GB, respectively, but for practical calculations five-cell systems really are the limit. For the bond model there are no additional symmetries that can be exploited.

### 3.3 Ising model

A linear array of QCA cells where each cell has a state of logic 0 or 1 is reminiscent of a 1D spin-half chain. Indeed, if we reduce the basis to only two states per cell, down from six states in the bond picture, we can map the QCA system to a transverse-field Ising model with long-ranged interactions. This is an attractive proposition: the smaller Hilbert space allows for larger system sizes with our exact diagonalization method; more importantly, the transverse-field Ising model is amenable to sign-problem-free stochastic series expansion (SSE) quantum Monte Carlo schemes [62]. These methods do not scale

exponentially<sup>1</sup> and consequently allow access to much larger systems. Last, but not least, such a mapping connects the QCA approach to the established and well studied Ising model. The prospect hinges on the assumption that the two-states-per-cell basis actually is a good approximation for QCA systems. And while bistable two-state cells are certainly the picture we have in mind when we talk about QCA, it is not *a priori* clear whether this is a correct physical picture. The transverse-field Ising model is equivalent to the two-states-per-cell approximation that has been used extensively, but was never satisfyingly derived, in the literature to study the dynamics of QCA systems.

We use the bond Hamiltonian (3.1) as the starting point. We had already discussed in the last chapter that such a Hamiltonian can be decomposed into single-cell terms and cell-cell interaction terms,

$$H = \sum_k H_k^c + \sum_{k<l} H_{kl}^{cc}. \quad (3.2)$$

In comparison, the transverse-field Ising model is described by

$$\tilde{H} = - \sum_k \gamma S_k^x + \sum_{k<l} J_{kl} S_k^z S_l^z. \quad (3.3)$$

Thus, we would like to map the single cell term  $H_k^c$  to the transverse-field term  $-\gamma S_k^x$  and the Coulombic cell-cell interaction  $H_{kl}^{cc}$  to the Ising term  $J_{kl} S_k^z S_l^z$ . Each cell  $k$  is identified with a pseudo spin  $S_k^z$ , specifically logic 0 with spin down and logic 1 with spin up, as illustrated in Fig. 3.2(a). We will first look at how the QCA cell can be represented by only two basis states and derive an approximate expression for the transverse field  $\gamma$ . Then we will use a multipole expansion to derive  $J_{kl}$  from the cell-cell Coulomb interaction.

To arrive at a single-cell-basis with only two states we can, in principle, follow a similar prescription as for the fixed-charge and bond approximations: we neglect high-energy states which are assumed to be gapped out. In this case, the neglected states are the four edge states with Coulomb energy  $V_1$ ,  $|\psi_Q\rangle = \{|3\rangle, |4\rangle, |5\rangle, |6\rangle\}$ , illustrated in Fig. 3.1, where we have introduced  $|\psi_Q\rangle$  to denote the high-energy subspace of the single-cell Hilbert space. We only keep the low-energy diagonal states  $|\psi_P\rangle = \{|1\rangle, |2\rangle\}$  with Coulomb energy  $V_0$ . Of course, these two states are exactly our logic 0 and logic 1 state, or in the Ising language,  $|\downarrow\rangle \doteq |1\rangle$  and  $|\uparrow\rangle \doteq |2\rangle$ . Here,  $|\psi_P\rangle$  denotes the low-energy subspace. For the high-energy states to be sufficiently gapped out, we require  $\Delta V = V_1 - V_0 \gg T$ . In contrast to the fixed-

---

<sup>1</sup> SSE quantum Monte Carlo methods roughly scale as  $N \ln N$  where  $N$  is the system size.

charge and bond model, merely truncating the Hilbert space is not sufficient for the Ising model. For our previous two approximations, the Hamiltonian had remained essentially unchanged, apart from dropping terms that were no longer relevant, such as the chemical potential term or the Hubbard  $U$  term. The states retained were exactly the same states as in the full, untruncated model. But with only two states per cell the existing Hamiltonian (3.1) does not “work”: there is no process that takes the cell from  $|1\rangle$  to  $|2\rangle$ , and the system would be stuck in either of the two spin states eternally. In the bond picture, in comparison, for the system to transition from state  $|1\rangle$  to  $|2\rangle$  it can take different paths, for example  $|1\rangle \rightarrow |3\rangle \rightarrow |2\rangle$ , consisting of two hopping processes with an interim high-energy edge state. We need to derive an effective, low-energy Hamiltonian from the bond model that treats those processes perturbatively, as *virtual* excitations, yielding an effective hopping term for the transition  $|1\rangle \leftrightarrow |2\rangle$ . This effective hopping is precisely the transverse field  $\gamma$  which flips the spin in the Ising picture.

A single QCA cell is described by the time-independent Schrödinger equation  $H_k^c |\psi\rangle = E_k |\psi\rangle$ , with  $|\psi\rangle = [|\psi_P\rangle |\psi_Q\rangle]$ . Our aim is to truncate the basis to  $|\psi_P\rangle$  and derive an effective Hamiltonian  $\tilde{H}_k^c$  with the subspace Schrödinger equation  $\tilde{H}_k^c |\psi_P\rangle = E_k |\psi_P\rangle$ . Using the basis depicted in Fig. 3.1, the single-cell bond Hamiltonian is very simple and can be written down explicitly. As the single-cell Hamiltonian is the same for all cells, we can drop the index  $k$ .

$$\begin{aligned}
H^c &= \left( \begin{array}{cc|cccc} V_0 & 0 & -t & -t & -t & -t \\ 0 & V_0 & -t & -t & -t & -t \\ \hline -t & -t & V_1 & 0 & 0 & 0 \\ -t & -t & 0 & V_1 & 0 & 0 \\ -t & -t & 0 & 0 & V_1 & 0 \\ -t & -t & 0 & 0 & 0 & V_1 \end{array} \right) \\
&= \begin{pmatrix} H_{PP} & H_{PQ} \\ H_{QP} & H_{QQ} \end{pmatrix}
\end{aligned} \tag{3.4}$$

Here, we have partitioned the Hamiltonian into four blocks,  $H_{PP}$ ,  $H_{QQ}$ ,  $H_{PQ}$ , and  $H_{QP}$ , corresponding to the low-energy subspace  $|\psi_P\rangle$ , the high-energy subspace  $|\psi_Q\rangle$ , and transition between the subspaces. With this partitioned Hamiltonian, the time-independent

Schrödinger equation is

$$\begin{pmatrix} H_{PP} & H_{PQ} \\ H_{QP} & H_{QQ} \end{pmatrix} \begin{pmatrix} \psi_P \\ \psi_Q \end{pmatrix} = E \begin{pmatrix} \psi_P \\ \psi_Q \end{pmatrix}. \quad (3.5)$$

Writing out the matrix equation as two equations explicitly, and eliminating  $|\psi_Q\rangle$  yields

$$H_{PP} |\psi_P\rangle + H_{PQ} \frac{1}{E - H_{QQ}} H_{QP} |\psi_P\rangle = E |\psi_P\rangle \quad (3.6)$$

and therefore

$$\tilde{H}^c = H_{PP} + H_{PQ} \frac{1}{E - H_{QQ}} H_{QP}. \quad (3.7)$$

Assuming that the system is predominantly in the subspace spanned by  $|\psi_P\rangle$  and additionally that the hopping is very small,  $t \ll V_0$ , we can approximate  $E \approx V_0$ . We write out the matrix multiplications and use  $(H_{PP})_{ij} = (V_0)_{ii} \delta_{ij}$ ,  $(H_{PQ})_{ij} = (-t)_{ij}$ , and so on. The effective Hamiltonian becomes

$$\begin{aligned} \tilde{H}_{ij}^c &= (V_0)_{ii} \delta_{ij} + (-t)_{ik} (V_0 - V_1)_{kk}^{-1} (-t)_{kj} \\ &= (V_0)_{ii} \delta_{ij} - \left( \frac{4t^2}{\Delta V} \right)_{ij}. \end{aligned} \quad (3.8)$$

As the system remains unchanged upon adding a constant term to the Hamiltonian, we can subtract the constant diagonal term  $\tilde{H}_{ii} = V_0 - \frac{4t^2}{\Delta V}$ , and arrive at

$$\tilde{H}^c = \begin{pmatrix} 0 & -\frac{4t^2}{\Delta V} \\ -\frac{4t^2}{\Delta V} & 0 \end{pmatrix}. \quad (3.9)$$

The off-diagonal matrix elements are the effective hopping, transitioning the system between its two states  $|1\rangle \leftrightarrow |2\rangle$ . If we now compare this matrix with the transverse-field term of the Ising model,

$$\begin{aligned} \tilde{H}^c &= -\gamma S_k^x \\ &= -\frac{1}{2} \gamma (S_k^+ + S_k^-) \\ &= \begin{pmatrix} 0 & -\frac{1}{2} \gamma \\ -\frac{1}{2} \gamma & 0 \end{pmatrix}, \end{aligned} \quad (3.10)$$

we identify the effective hopping as the transverse field,

$$\gamma = \frac{8t^2}{\Delta V}. \quad (3.11)$$

The effective hopping is a virtual process involving two hopping processes in the original bond model, yielding the  $t^2$  in the numerator, and an interim high-energy state gapped out by  $\Delta V$ , hence the  $\Delta V$  in the denominator. To arrive at the expression for the effective hopping  $\gamma$  we used the assumptions  $\Delta V \gg T$  and  $t \ll \Delta V$ . As a reminder,  $\Delta V = V_1 - V_0 = \frac{2-\sqrt{2}}{2} \frac{1}{a} \approx 0.3V_1$ . Notably, the energy gap is independent of the compensation charge  $q$ . As the derivation used only a single cell, it is also implicitly assumed that the perturbations from other cells in the system are small, at least as far as the effective hopping is concerned. If the hopping depended on the state of nearby cells, then the effective Hamiltonian would be much more involved and certainly could not be mapped to an Ising-like model.

We have successfully derived an effective hopping term and therefore also an effective two-state model for the QCA Hamiltonian. With only two states per cell the Hilbert space scales as  $N_s = 2^{N_c}$  ( $N_c$  the number of cells) and up to 14 cells are computationally feasible, with memory requirements of 2GB. In practice, we restrict the calculations to a maximum of 12 cells. For our calculations, we can use the two-state approximation with the effective hopping term but still retain the original cell-cell interaction term  $H_{kl}^{cc}$ . From a computational point of view, nothing is gained by expressing the cell-cell interaction as an Ising interaction. However, deriving  $J_{kl}$  from  $H_{kl}^{cc}$  is very rewarding conceptually and will already allow some key insights into the characteristics of QCA devices. Therefore, we now undertake the derivation of an expression for  $J_{kl}$ . The obvious starting point is the cell-cell interaction term  $H_{kl}^{cc}$ ,

$$\begin{aligned} H_{kl}^{cc} &= \sum_{\substack{i \in k \\ j \in l}} V_{ij} (n_i - q) (n_j - q) \\ &= \sum_{\substack{i \in k \\ j \in l}} \frac{(n_i - q) (n_j - q)}{|\mathbf{R}_{kl} + \mathbf{r}_j - \mathbf{r}_i|} \\ &= \sum_{\substack{i \in k \\ j \in l}} \frac{n_i n_j - q(n_i + n_j)}{|\mathbf{R}_{kl} + \mathbf{r}_{ij}|}, \end{aligned} \quad (3.12)$$

where  $i$  and  $j$  sum over the four dots  $1, \dots, 4$  of cell  $k$  and  $l$ , respectively, and  $\mathbf{R}_{kl}$  denotes

the vector between the centres of the cells, see Fig. 3.2(b). We have introduced  $\mathbf{r}_{ij} = \mathbf{r}_j - \mathbf{r}_i$  and dropped the constant  $q^2$  term in the last line of Eq. (3.12). There are only four possible configurations for two interacting cells:  $\uparrow\uparrow$ ,  $\downarrow\downarrow$ ,  $\uparrow\downarrow$ , and  $\downarrow\uparrow$ . Using the shorthand notations  $V_{ij} = \frac{1}{|\mathbf{R}_{kl} + \mathbf{r}_{ij}|} + \frac{1}{|\mathbf{R}_{kl} - \mathbf{r}_{ij}|}$  and  $V_{00} = \frac{1}{|\mathbf{R}_{kl}|}$ , we calculate their energies explicitly.

$$E^{\uparrow\uparrow} = (1 - 2q) (2V_{00} + V_{24}) - q (2V_{12} + 2V_{14}) \quad (3.13)$$

$$E^{\downarrow\downarrow} = (1 - 2q) (2V_{00} + V_{13}) - q (2V_{12} + 2V_{14}) \quad (3.14)$$

$$E^{\uparrow\downarrow} = (1 - 2q) (V_{12} + V_{14}) - q (4V_{00} + V_{13} + V_{24}) \quad (3.15)$$

$$E^{\downarrow\uparrow} = (1 - 2q) (V_{12} + V_{14}) - q (4V_{00} + V_{13} + V_{24}) \quad (3.16)$$

Note that the expression for two spin-down cells can be obtained from the expression for two spin-up cells (and similarly  $E^{\uparrow\downarrow}$  from  $E^{\downarrow\uparrow}$ ) simply by rotating the system by  $90^\circ$ , or equivalently, by permuting the dot numbering:  $1, 2, 3, 4 \rightarrow 4, 1, 2, 3$ . Symmetries can be exploited, for example  $V_{43} = V_{12}$ . Evidently,  $E^{\uparrow\downarrow} = E^{\downarrow\uparrow}$ , which, given the highly symmetric geometry of those cell arrangements, does not come as a surprise. But crucially, we find that  $E^{\uparrow\uparrow} \neq E^{\downarrow\downarrow}$ . Therefore, we have a system with three distinct energy levels that we cannot hope to represent with the solely two-level Ising term  $J_{kl} S_l^z S_l^z$ . Instead, let us try to map to a *modified* Ising model with a three-level cell-cell interaction term of the form

$$\tilde{H}_{kl}^{\text{cc}} = J_{kl} S_k^z S_l^z + J'_{kl} (S_k^z + S_l^z) . \quad (3.17)$$

For this Hamiltonian we have the energies

$$\tilde{E}^{\uparrow\uparrow} - \tilde{E}^{\uparrow\downarrow} = 2J_{kl} + 2J'_{kl} \quad (3.18)$$

$$\tilde{E}^{\downarrow\downarrow} - \tilde{E}^{\uparrow\downarrow} = 2J_{kl} - 2J'_{kl} \quad (3.19)$$

which yields

$$J_{kl} = \frac{1}{4} (\tilde{E}^{\uparrow\uparrow} + \tilde{E}^{\downarrow\downarrow} - 2\tilde{E}^{\uparrow\downarrow}) \quad (3.20)$$

$$J'_{kl} = \frac{1}{4} (\tilde{E}^{\uparrow\uparrow} - \tilde{E}^{\downarrow\downarrow}) , \quad (3.21)$$

and therefore, identifying  $E^{\uparrow\uparrow} = \tilde{E}^{\uparrow\uparrow}, E^{\downarrow\downarrow} = \tilde{E}^{\downarrow\downarrow}$ , and so on,

$$J_{kl} = \frac{1}{4} (4V_{00} + V_{13} + V_{24} - 2V_{12} - 2V_{14}) \quad (3.22)$$

$$J'_{kl} = \frac{1}{4} (1 - 2q) (V_{24} - V_{13}) . \quad (3.23)$$

These results, while abstract, are remarkable in two ways. First, the newly introduced term  $J'_{kl}$  vanishes for  $q = \frac{1}{2}$ . In that special case,  $E^{\uparrow\uparrow} = E^{\downarrow\downarrow}$ . Thus, only for charge neutral cells do we recover the genuine, unmodified transverse-field Ising model. Second, the Ising  $J_{kl}$  itself is independent of the compensation charge  $q$ . We will see that  $J_{kl}$  is the quadrupole-quadrupole cell-cell interaction, to leading order. Thus, it is fair to say that  $J_{kl}$  is the pure QCA interaction. With the above equations we can also already look at rotational symmetries of  $J_{kl}$  and  $J'_{kl}$ :  $J_{kl}$  is invariant under rotations by  $90^\circ$  as can be seen by permuting the dots  $1, 2, 3, 4 \rightarrow 4, 1, 2, 3$ . This is what we expect intuitively. For example, a horizontal straight line of cells ( $\theta = 0^\circ$ ) should behave exactly the same as a vertical straight line of cells ( $\theta = 90^\circ$ ). In contrast,  $J'_{kl}$  is not invariant under rotations by  $90^\circ$ . In fact, applying the same dot permutation yields  $J'_{kl} \xrightarrow{90^\circ} -J'_{kl}$ . Consequently,  $J'_{kl}$  is symmetric under rotations by  $180^\circ$ . It is also clear that a non-zero  $J'_{kl}$  breaks the system's symmetry under spin inversion— $\tilde{H}_{kl}^{\text{cc}}$  is not unchanged for  $\uparrow\uparrow \rightarrow \downarrow\downarrow$ . This has profound implications for QCA. For non-zero  $J'_{kl}$  we would, for example, expect different polarization responses for two spin-down cells versus two spin-up cells, and as a consequence the device would behave differently for logic 0 and logic 1 signals. From an application point of view, this is definitely not what we want. For QCA operation we therefore require charge neutral cells and a genuine, unmodified Ising model.

To obtain more tangible expressions for  $J_{kl}$  and  $J'_{kl}$  we perform a multipole expansion of the  $V_{ij}$  terms. Specifically,

$$\begin{aligned} \frac{1}{|\mathbf{R}_{kl} \pm r_{ij}|} &= \frac{1}{R_{kl}} \left( 1 \pm 2 \frac{\mathbf{r}_{ij} \cdot \hat{\mathbf{R}}_{kl}}{R_{kl}} + \frac{r_{ij}^2}{R_{kl}^2} \right)^{-1/2} \\ &= \frac{1}{R_{kl}} (1 \pm x + y)^{-1/2} \end{aligned} \quad (3.24)$$

is Taylor-expanded in  $x$  and  $y$ , keeping all terms up to  $\mathcal{O}(a^4/R_{kl}^5)$ , which corresponds to quadrupole-quadrupole interactions. Plugging the results of the expansion back into



Eqs. (3.22) and (3.23) yields

$$J_{kl} = \frac{1}{32} (9 - 105 \cos 4\theta) \frac{a^4}{R_{kl}^5} \quad (3.25)$$

$$J'_{kl} = (1 - 2q) \left( \frac{3}{2} \sin 2\theta \frac{a^2}{R_{kl}^3} + \frac{5}{4} \sin 2\theta \frac{a^4}{R_{kl}^5} \right). \quad (3.26)$$

The leading order term of  $J_{kl}$  is  $R^{-5}$ , the quadrupole-quadrupole interaction. In contrast, the leading order term of  $J'_{kl}$  is  $R^{-3}$  and therefore, in general,  $J'_{kl}$  would be the dominant term—yet another argument why a non-zero  $J'_{kl}$  is highly undesirable for functioning QCA devices. Of course, we find our general symmetry observations confirmed by these more concrete expressions for  $J_{kl}$  and  $J'_{kl}$ : the former is invariant under  $90^\circ$  rotations, the latter only under rotations of  $180^\circ$ . Both terms vanish at select angles. For example, we have  $J'_{kl} = 0$  for  $\theta = 0^\circ$ , so that at least for an exactly straight line of cells we recover the unmodified Ising model, even for non-charge-neutral cells. This does not help when building more complex devices than a wire, of course, but might still be useful for some experiments. As another example,  $J_{kl} = 0$  for  $\theta = 22.5^\circ$ . Conceivably, this could be exploited for device applications, to decouple closely spaced cells. As multipole expansions, the obtained expressions for  $J_{kl}$  and  $J'_{kl}$  should be valid for large cell-cell distances. In principle, an arbitrary number of higher order terms can be included to make the expressions as exact as desired. In practice on the computer, however, we do not use the multipole expansion at all, but simply sum up all Coulomb interactions exactly. We will see in due course that for the small cell-cell distances that we are typically interested in, an expansion up to  $R^{-5}$  is indeed not sufficient, and higher order terms would have to be included.

In summary, we have successfully mapped the QCA bond Hamiltonian (3.1) to a modified transverse-field Ising model,

$$\tilde{H} = - \sum_k \gamma S_k^x + \sum_{k < l} [J_{kl} S_k^z S_l^z + J'_{kl} (S_k^z + S_l^z)] , \quad (3.27)$$

where  $J_{kl}$  and  $J'_{kl}$  are given by Eqs. (3.25) and (3.26), and  $\gamma$  by Eq. (3.11).

### 3.4 Validity of the approximations

In the last three sections we have introduced three successive approximations for the QCA Hamiltonian: the fixed-charge model, the bond model, and the Ising model. However, even though we know the extreme theoretical limits in which those approximations become exact, we have given little thought to the practical bounds of applicability. Numerical benchmarks will help us establish the parameter regimes where we can use the approximations and get sufficiently accurate results, and also give us a better understanding of how the approximations behave in those parameter ranges.

The fixed-charge approximation is a Hilbert space truncation where we only keep the states with exactly two electrons per cell. Figure 3.3(a) compares the density of states of the fixed-charge model against the exact grand canonical model for a two-cell system. The chemical potential is  $\mu = 250$  and the nearest-neighbour Coulomb energy is  $V_1 = 100$ , whereas the on-site Coulomb repulsion is  $U = 1000$ . The energies are in units of the hopping  $t$ , with  $t = 1$ . The cells are placed a distance  $d/a = 3$  apart, horizontally; a driver cell to the left sets the input  $P_D = 1$ . This system does not have any compensation charges, hence  $q = 0$ . The approximation reproduces the low-energy spectrum exactly, in the plot up to  $E \lesssim 35$ . Therefore, as long as the two-electrons-per-cell sector is lowest in energy and the temperature is small compared to the energy of the next charge sector, the model works perfectly. Figure 3.3(b) plots the number of particles per cell over temperature and demonstrates the breakdown of the approximation. Whereas the fixed-charge model gives, per definition, a constant number of particles over the whole temperature range, the grand canonical system’s cell occupancies start to diverge from two electron per cell at around  $T \sim 10$ . This roughly corresponds to the energy states the fixed-charge model misses at  $E \gtrsim 35$ . A small deviation from exactly two electrons per cell is not detrimental to QCA; a cell occupied by only one or by three electrons, however, renders QCA non-functional. We often use the fixed-charge model as the starting point and assume, without further investigation, that a practical QCA implementation can be tuned to be in the right charge regime at a given temperature.

The bond model neglects doubly occupied states and represents the four states of a bond—one singlet and three triplets—with only one single bond state. The model thus assumes that singlet and triplet states are energetically equivalent, but we had already asserted that we might expect a small singlet-triplet splitting. Figure 3.4(a) shows the density of states of a single QCA cell for both the fixed-charge and the bond model. The hopping

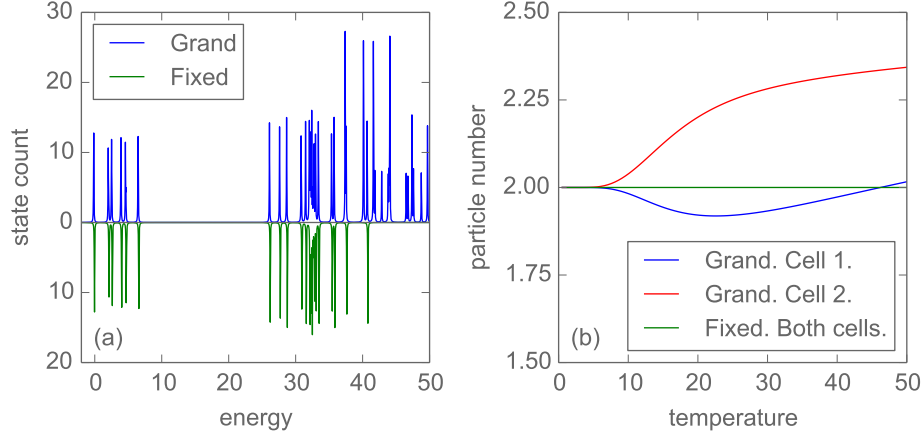


Figure 3.3: (a) Low-energy density of states of the exact grand canonical and the approximate fixed-charge two-cell QCA system. For small energies the curves agree perfectly (up to  $E \lesssim 35$ ). (b) Particle number per cell over temperature for the same two-cell system. The curves diverge for  $T \gtrsim 10$ .

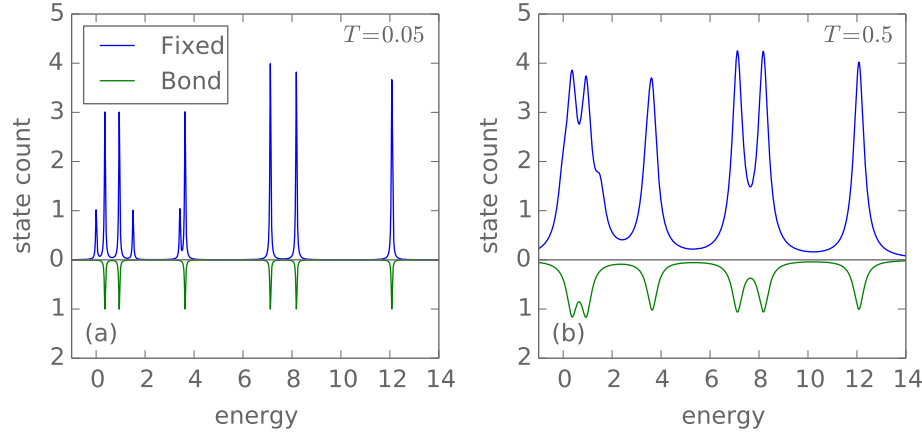


Figure 3.4: (a) Low-energy density of states of a one-cell QCA system for both the fixed-charge and the bond model. The bond approximation only reproduces the triplet states, but omits the singlet states. The “measurement” temperature is indicated. (b) The same spectrum, but “measured” at a higher temperature. The singlet-triplet splitting is “washed out” at large enough temperatures: the singlet and triplet peaks are no longer separately resolved and each bond model state corresponds to four fixed-charge states at roughly the same energy.

is again  $t = 1$ , the nearest-neighbour Coulomb energy is  $V_1 = 20$ , and the on-site Coulomb repulsion is  $U = 10^6$ —practically at infinity. A driver cell placed at a distance  $d/a = 3$  to the left of the single cell serves as an input. We have chosen the driver cell’s polarization to be  $P_D = 1$ . Indeed, each bond state corresponds to three fixed-charge states—the triplet—and one “close-by” state—the singlet. They are not energetically equivalent, but split by a small energy gap,  $\Delta E_S$ , the singlet-triplet splitting. Like the fixed-charge model, the bond approximation truncates the Hilbert space and the retained states are exact. Evidently, the bond model keeps one triplet state, but discards the other two and the singlet. We understand that, similar to the antiferromagnetic Heisenberg coupling constant  $J$  emerging in the low-energy limit of the Hubbard model (with  $J \sim \frac{t^2}{U}$ ) [63], here, virtual excitations to high-energy doubly occupied states lower the energy of the singlet state and make it the ground state. Because the bond model misses those doubly occupied states, it cannot accommodate singlet states and hence reproduces the triplet states. Consequently, we cannot hope that the bond model is correct for ground state and low-temperature properties. We assert that as long as the singlet-triplet splitting is “washed out”, that is, as long as the temperature is much larger than the singlet-triplet gap,  $T \gg \Delta E_S$ , the approximation should give good results. At high enough temperatures, the system no longer “sees” the difference between the singlet and the triplet states. This is illustrated in Fig. 3.4(b) where the spectrum is “measured” at a higher temperature:<sup>2</sup> the singlet and triplets are no longer resolved separately. Instead, each bond state corresponds to four fixed-charge states at roughly the same energy.

The figure shows all six bond states of the single cell—the complete spectrum apart from the doubly occupied states. As this cell is perturbed by a nearby driver cell with  $P_D = 1$ , the ground state is qualitatively closest to the logic 1 state, or  $|2\rangle$  in Fig. 3.1. Similarly, the first excited state is similar to  $|1\rangle$ , or logic 0, and the four higher energy states correspond to  $|4\rangle$ ,  $|5\rangle$ ,  $|3\rangle$ , and  $|6\rangle$ , in that order. Of course, in general the energy eigenstates are a mixture of all basis states, but we can still characterize them by the most dominantly contributing basis state. As this is a non-charge-neutral system,  $q = 0$ , with a relatively small cell-cell distance  $d/a = 3$ , charge buildup tends to push the electrons to the far edge of the cell, thus making  $|4\rangle$  lower in energy than  $|6\rangle$ .

---

<sup>2</sup> We calculate the density of states graphs by folding the energy eigenvalues of the system—a delta function energy spectrum—with a Lorentzian with the half-width at half-maximum set by a “measurement” temperature. Very roughly speaking, this corresponds to a photoemission / inverse photoemission spectroscopy experiment at this temperature.

Since the bond model ignores the singlet-triplet splitting, it is important to understand how the gap  $\Delta E_S$  depends on various system parameters. To that end we picked out a few selected singlet-triplet states from the spectrum in Fig. 3.4(a) as examples. Contrary to expectations, for those states the gap  $\Delta E_S$  did not change significantly with the on-site Coulomb repulsion  $U$ . However, it did become smaller for shorter and shorter cell-cell distances  $d$ . Most importantly, for the nearest-neighbour Coulomb energy  $V_1$  we found  $\Delta E_S \sim \frac{1}{V_1^p}$ . The exponent is  $p \sim 3$  when the cell “sees” a biasing external potential (e.g.  $P_D = \pm 1$ ) and  $p \sim 1$  otherwise (e.g.  $P_D = 0$ ). Even though our method is anything but rigorous and the obtained results very likely not universally true, the findings should nonetheless give a good enough idea of the principal trends. Quite generally, the higher the overall Coulomb potential—large  $V_1$  and small  $d$ —the smaller the singlet-triplet splitting and, conceivably, the more accurate the bond approximation. The bond model should work as long as  $T \gg T_{\min}$  with  $T_{\min} \sim \Delta E_S$ , and as a very rough guideline we can use  $\Delta E_S \sim \frac{t^2}{V_1}$ . Of course, we also need  $T \ll T_{\max}$  with  $T_{\max} \sim U$ , so that the doubly occupied states are gapped out.

To illustrate the limitations of the bond approximation we now look at a two-cell system: a horizontal line of cells with two active cells and a driver cell to the left. Figure 3.5 shows the spectra and output polarizations of the system for two different Coulomb energies,  $V_1 = 20$  and  $V_1 = 100$ . Otherwise the parameters are the same as for the one-cell system in the previous graph. In particular, the spectrum in Fig. 3.5(a) is exactly the same as in Fig. 3.4(a), except that we have added one more cell to the system. Each bond state now corresponds to 16 (i.e.,  $4 \times 4$ ) fixed-charge states. Looking at the four lowest-energy peaks in the spectrum, we see that the bond model exactly reproduces the nine triplet-triplet states, but misses the three singlet-triplet and the three triplet-singlet states (in the graph the corresponding two peaks are hardly distinguishable), as well as the single singlet-singlet ground state. The four lowest bond states should roughly correspond to, in that order, both cells being aligned with the driver cell (the ground state), only one of the two cells being aligned with the driver cell, and both cells being anti-aligned with the driver cell. Higher energy states have at least one of the cells not in the preferred diagonal states,  $|1\rangle$  and  $|2\rangle$ , with electrons occupying predominantly the edge of a cell.

Arguably, the spectra of the fixed-charge and the bond model in Fig. 3.5(a) do not look very similar. Consequently, the polarization curves in Fig. 3.5(b) do not agree, especially at low temperatures. In fact, it is rather remarkable that given the widely dissimilar spectra, the polarizations actually do agree relatively well at higher temperatures,  $T \gtrsim 1$ .

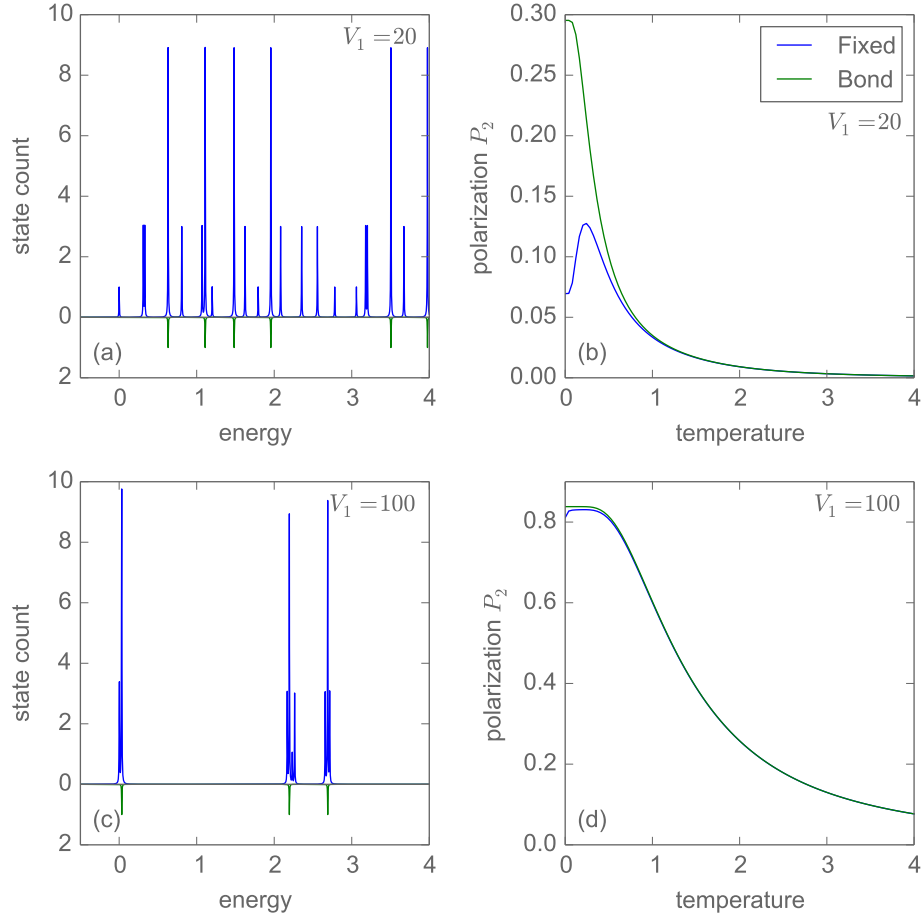


Figure 3.5: The two-cell fixed-charge and bond systems at  $V_1 = 20$  and  $V_1 = 100$ . (a)(c) Low-energy density of states. (b)(d) Output polarization  $P_2$  over temperature. For a small Coulomb repulsion the density of states curves look qualitatively very different (a) and the bond approximation does not work very well (b). At a larger Coulomb repulsion the density of states curves look much more alike (c) and the bond approximation works much better (d).

The bond model only reproduces the most populous energy states of the exact spectrum. Apparently, that is enough to give (almost) correct results at high temperatures. The lower the temperature, the more important become the few lowest lying energy states which the bond model misses. Very roughly speaking, the temperature where the bond model's polarization becomes accurate also matches the temperature where we saw the singlet-triplet splitting being washed out in Fig. 3.4(b). For the much larger Coulomb energy  $V_1 = 100$  the spectra look much more alike, qualitatively, even though the bond model obviously still does not resolve all the lines of the exact density of states, as illustrated in Fig. 3.5(c). Therefore, the approximation works much better: the polarization curves agree down to much lower temperatures and even the discrepancy of the ground state polarizations is much reduced, as demonstrated in Fig. 3.5(d). Compared to the  $V_1 = 20$  system, the ground state polarization is much larger and, generally, the larger the cell polarization, the better the agreement between bond and fixed-charge model. We also note that in the spectrum the peaks are much more spaced out, and thus the  $V_1 = 100$  wire retains larger cell polarizations up to much higher temperatures. For any conventional material, a Coulomb energy scale such as we have chosen here,  $V_1/t \geq 20$ , where we have, of course,  $U/t \gg V_1/t$ , seems like an extremely large value. However, we will find that such Coulomb energies are generally in agreement with what the QCA approach itself requires, and we will discuss this in detail in the next chapter.

The polarization of the fixed-charge model shows a curious bump at low temperatures, for example in Fig. 3.5(b), and similarly, if less visibly, in Fig. 3.5(d). Apparently, the ground state is not the most polarized state. Maximum polarization is reached at a small, but finite temperature. At the same time, for the bond model the ground state is the most polarized state and generally its zero-temperature polarization is larger than that of the fixed-charge model. Interestingly, in contrast to the fixed-charge model, the bond model's ground state polarization is largely independent of the magnitude of the driver polarization and also only weakly influenced by the cell-cell distance  $d$ , especially for charge-neutral cells where no charge buildup occurs. Instead, it is predominantly set by  $V_1$ , and thus by  $V_1/t$  and the energy gap  $\Delta V = V_1 - V_0$ . Without an external perturbation such as a non-zero driver polarization the ground state polarization is zero, of course. But any infinitesimal external perturbation will instantly see the bond model's ground state become almost fully polarized. We interpret this behaviour as the ground state actually consisting of two energetically degenerate states, corresponding to  $\pm P_{\text{gs}}$ , where  $P_{\text{gs}}$  is the full ground state polarization for a given  $V_1$ . The smallest perturbation lifts this degeneracy and sees the

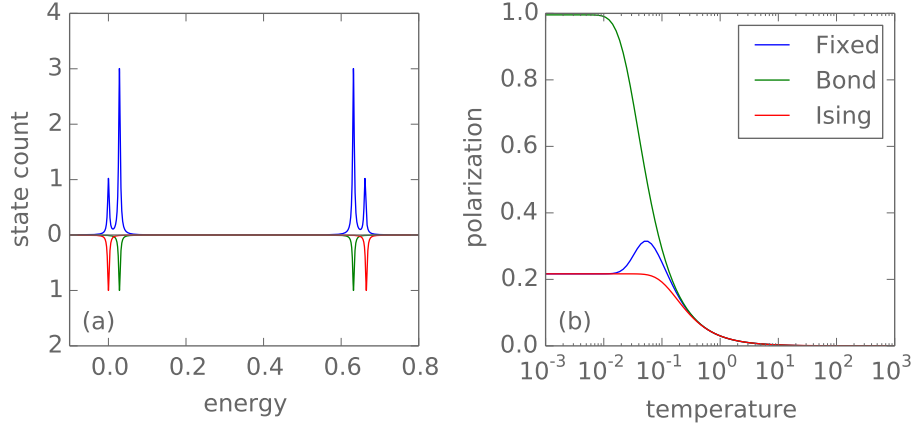


Figure 3.6: Comparing the fixed-charge, bond, and Ising model for the one-cell charge-neutral QCA system. (a) Low-energy density of states. The Ising model reproduces the singlet and not the triplet states, as the bond model does. (b) Cell polarization over temperature. At larger temperatures  $T \gtrsim 0.3$  all three models seem to agree. At  $T = 0$  the bond model is wrongly fully polarized, whereas the Ising model exactly reproduces the fixed-charge model’s ground state polarization.

system snapping to either  $+P_{\text{gs}}$  or  $-P_{\text{gs}}$ . Now the bond model’s ground state corresponds to the fixed-charge model’s triplet state—one of the lower lying excited states, but not the ground state. The true ground state of the more exact model is a single singlet state, a superposition of the  $+P_{\text{gs}}$  and  $-P_{\text{gs}}$  (and other) states. Therefore, the polarization of the true ground state is generally smaller in magnitude than the polarization of the corresponding two triplet states, explaining the low temperature bump in the polarization curve and the larger polarization of the bond model’s ground state.

The Ising approximation is derived as an effective low-energy model from the bond Hamiltonian. It is therefore qualitatively different from the previous two approximations: it is not merely a Hilbert space truncation. While the Ising model should resemble the bond model in the limit where the approximations in its derivation become exact, for less than optimal parameters the models’ states need not be in perfect agreement. The derivation assumed  $E \approx V_0$  ( $E$  the energy of the whole system) and therefore  $t \ll \Delta V$  as well as  $T \ll \Delta V$ . Additionally, cells were assumed to be isolated, so the Ising model presumably requires reasonably large cell-cell distances. Naturally, the model inherits the limits of the bond approximation, and we would therefore expect  $T \gg \Delta E_{\text{S}}$  ( $\Delta E_{\text{S}}$  the singlet-triplet



splitting) and  $T \ll U$  as further requirements. It is important to keep in mind that the Ising model is not a low-energy model for the more exact fixed-charge Hamiltonian—it is derived as the low-energy limit of the bond model, which, however, is not an accurate low-energy description of the fixed-charge system. The approximation can also not hope to capture non-charge-neutral systems correctly. It simply lacks the edge states that are the manifestation of charge buildup, as discussed in the example of the one-cell bond system above. We had seen in the derivation of the Ising model that non-charge-neutral cells are very problematic for the QCA approach in general. Consequently, we will concentrate on charge-neutral systems with a compensation charge  $q = \frac{1}{2}$  for the remainder of the chapter.

To understand how the Ising approximation behaves, we again start by looking at the density of states of a one-cell system, shown in Fig. 3.6(a). We have plotted both the fixed-charge and bond model’s density of states for comparison and now use slightly different system parameters: the nearest-neighbour Coulomb energy is  $V_1 = 100$ , the cell-cell distance is  $d/a = 4$ , and the driver cell is only slightly polarized with  $P_D = 0.1$ . As always, the hopping is  $t = 1$ . We are in for a surprise! Evidently, the Ising model reproduces the singlet states and not the bond model’s triplet states. In line with this observation, the Ising model exactly matches the fixed-charge model’s ground state polarization, but misses the triplet-bump at  $T \sim 0.05$ , as can be seen in Fig. 3.6(b). Here, for the charge-neutral system, the bond model’s ground state is fully polarized even at this large cell-cell distance and for a very weak driver cell polarization. Even though we had derived the Ising model from the bond Hamiltonian, it does not resemble the bond model at all, which is very confusing. To lift the confusion, we first note that, even though the Ising model correctly captures the fixed-charge ground state of the single-cell system, this is not true in general for larger systems, as we will see in a moment. Second, we need to be very careful when we talk about the bond model. The bond Hamiltonian is simply a spinless model that does not distinguish between singlet and triplet states. In contrast, the bond model uses a concrete basis and we saw that it chooses the triplet states. Therefore, the bond Hamiltonian, from which we derived the Ising model, and the bond model are not equivalent. Because the Ising model is an effective low-energy model, it makes sense that it captures the singlet states, which are lowest in energy. The Ising and bond states should still eventually become energetically and qualitatively equivalent, in the limit where the Ising model becomes exact and the singlet-triplet splitting goes to zero. On second thought, the fact that the Ising model exactly reproduces the ground state of the one-cell system is maybe not as surprising, because we had derived it precisely for a single, isolated cell.

Close inspection of the Ising model's only two states as compared to the equivalent fixed-charge model's states show that they are not exactly the same energetically. The difference is hardly discernible in the plotted spectrum, but more pronounced for differently chosen system parameters. Given that the Ising approximation is an effective model and used several assumptions in its derivation, this is hardly surprising. For the single-cell system we can easily study the error of the energies of the Ising states with respect to the fixed-charge states: the states are in better agreement for larger  $V_1$  and smaller  $t$ . The error explodes for very small cell-cell distances  $d/a < 2$ —when the assumption of isolated cells breaks down—but is largely independent of  $d/a$  otherwise. Therefore, we find the assumptions and limits of the derivation confirmed.

To be able to better quantitatively compare different models we introduce the relative error of the polarization, defined as

$$\epsilon_k^{\text{I}} = \frac{|P_k^{\text{F}} - P_k^{\text{I}}|}{P_k^{\text{F}}} \quad (3.28)$$

for the Ising model. We use the fixed-charge model as the reference. Hence,  $P_k^{\text{F}}$  refers to the polarization of cell  $k$  with the fixed-charge model and  $P_k^{\text{I}}$  is the same polarization, but determined using the Ising model. The relative error for the bond model,  $\epsilon_k^{\text{B}}$ , is defined equivalently. The relative error is independent of the magnitude of the polarization and therefore suitable for comparing models over wide parameter ranges. For best results it is also desirable not to drive the systems into full polarization. Once cells are saturated at  $|P_k| \sim 1$  the quantitative differences between the models disappear. This is why for our calculations with the Ising model here, which generally require larger  $V_1/t$  ratios, we have chosen larger cell-cell distances and smaller driver cell polarizations, resulting in less polarized cells.

Figure 3.7 shows the relative error over temperature together with the density of states for all three models for a two-cell system at  $V_1 = 100$  and  $V_1 = 200$ . As before, we find that the bond approximation works much better when its spectrum looks qualitatively more similar to the fixed-charge spectrum. At  $V_1 = 100$  the bond model yields an almost fully polarized ground state, whereas the fixed-charge model's zero-temperature polarization is much smaller, resulting in a very large relative error, as indicated in Fig. 3.7(b). At  $V_1 = 200$ , both the fixed-charge and the bond system are almost fully polarized at low temperatures and the relative error is therefore very small, as demonstrated in Fig. 3.7(d).

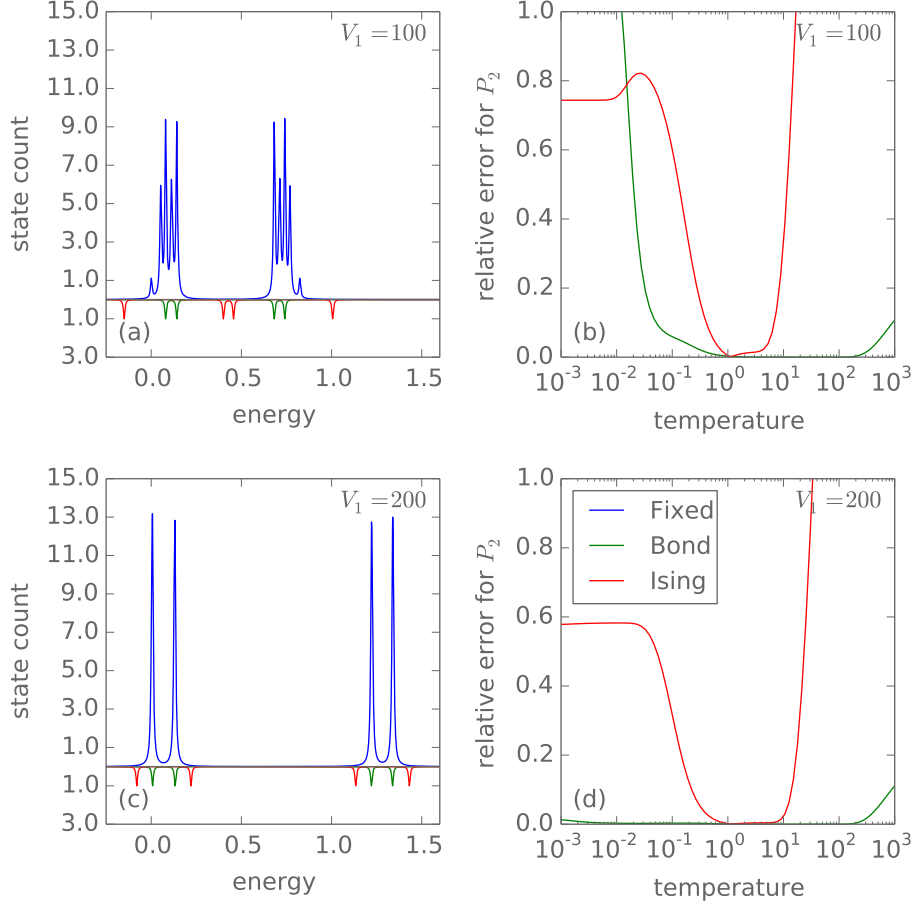


Figure 3.7: Comparing the fixed-charge, bond, and Ising model for the two-cell charge-neutral QCA system at  $V_1 = 100$  and  $V_1 = 200$ . (a)(c) Low-energy density of states. The Ising model's spectrum is qualitatively quite wrong, although it is in better agreement with the bond model's spectrum for larger  $V_1$ . (b)(d) Relative error of the output polarization of the bond and Ising model, with respect to the fixed-charge model. The bond model's error is small over a large range of temperatures. At  $T \sim U \sim 1000$  the neglected doubly occupied states become noticeable. The Ising model's error is small only over a relatively narrow temperature range. Its ground state no longer agrees with the fixed-charge model's ground state.

For these calculations we used  $U = 1000$  for the on-site Coulomb repulsion, but otherwise the same parameters as for the one-cell system above. Accordingly, we can see that the bond model starts to diverge for  $T \gtrsim 200$ . Even at  $T = 1000$  the error is relatively small, because the polarization is quite insensitive to doubly occupied dots, being defined solely as the difference in charge of one diagonal versus the other diagonal of the cell. Note that at these large temperatures the actual polarization is already very small.

Looking at the relative error of the Ising model, we first notice that it becomes very large for  $T > T_{\max}$  with  $T_{\max} \sim 5 \dots 10$ . Of course, this is a consequence of the Ising model missing the gapped out edge states, where the gap is  $\Delta V \sim 0.3V_1$ . Accordingly,  $T_{\max}$  is larger for  $V_1 = 200$  than for  $V_1 = 100$ , though maybe not by as much as we might expect. In stark contrast to the one-cell system, for two cells the Ising model's ground state no longer agrees with the ground state of the fixed-charge model. The Ising zero-temperature polarization is generally smaller than the polarization of the more exact model, and, similarly to the bond model, the zero-temperature relative error decreases for increasing  $V_1$ . The relative error curves of the Ising model reveal that the temperature range where the error is actually small—that is, where the Ising model can be considered valid—is quite narrow. For  $V_1 = 100$  it is almost like a sweet spot, a very narrow window around  $T \sim 1$ . For  $V_1 = 200$  the situation is much better, the error is close to zero in the temperature range  $T = T_{\min} \dots T_{\max} \sim 0.8 \dots 8$ . This temperature range only very weakly depends on the cell-cell distance  $d/a$  or the driver polarization  $P_D$ . It is dominantly set by  $V_1$ . Roughly speaking, the lower temperature limit  $T_{\min}$  is set by the singlet-triplet splitting, which becomes smaller with increasing  $V_1$ , and the upper temperature limit  $T_{\max}$  is set by  $\Delta V$  which is, of course, directly proportional to  $V_1$ . Here we have, as always, kept the hopping constant at  $t = 1$ . In agreement with our analysis for the one-cell system, the relative error at a fixed temperature decreases with increasing  $V_1$ , but is largely independent of  $d/a$  as long as  $d/a$  is not too small.

The spectrum of the Ising approximation does not compare well with the fixed-charge or bond model, especially at  $V_1 = 100$ , shown in Fig. 3.7(a). Clearly, the Ising model gets the energy levels completely wrong. However, we have to keep in mind that, in contrast to the bond model, the Ising model's states may be qualitatively different from the more exact models' states. Therefore, even though the spectrum looks completely wrong, the Ising model still does work correctly, if in a very small temperature range. In the right limit the Ising model should eventually resemble the bond model and accordingly, at  $V_1 = 200$ , the two models' spectra do look comparable, as can be seen in Fig. 3.7(c). The qualitative

agreement of the spectra becomes better for smaller cell-cell distances and larger driver cell polarizations as well, thus generally when the cells are more fully polarized.

All told, the Ising model is a tricky approximation. It is conceptually confusing, because, even though it is derived from the bond Hamiltonian, it does not exactly resemble the bond model. Adding to this confusion is the fact that it gets the ground state of the one-cell fixed-charge system right. From a practical point of view, the Ising model requires very large  $V_1/t$  ratios and its operational window can be very small, unless one is willing to go to obscenely large  $V_1/t$  ratios. Therefore, for moderately large Coulomb energies, great care should be exercised when using the Ising approximation. Calculations should be verified with a more exact model as much as possible and the error, and trends of the error, should be kept in check. Where an explicit verification is not possible, for larger systems, its results should be taken with a grain of salt.

As a final step, we look at a few concrete systems and their error trends. For a horizontal wire with three to five cells, a cell-cell distance of  $d/a = 4$ , and a nearest-neighbour Coulomb energy  $V_1 = 100$ , Fig. 3.8(a) shows the relative error as a function of the number of cells in the system. For these larger systems the Ising approximation and its error are benchmarked against the bond model and not the fixed-charge model as before. We notice that for these wires the error is quite a bit smaller at  $T = 2$  compared to  $T = 1$ , and an error of 1% seems to be the best we can do. Most worryingly, the error increases with the number of cells in the wire. This trend holds quite generally, for a range of systems with different cell-cell distances  $d/a$  and Coulomb energies  $V_1$ . Consequently, we expect the error to grow with increasing system sizes and once the systems are too large for bond model calculations, we will not be able to give a good upper error bound. The error will become uncontrolled. On a slightly more optimistic note, the error seems to decrease from cell to cell inside each wire. This is explored in more detail in Fig. 3.8(b), where we have plotted the error of each cell inside a five-cell wire. Evidently, the error decreases along the wire and we can expect this decrease to counter the generally growing error for longer and longer wires, at least as long as we are mainly interested in the output polarization of the wire. However, this trend is not true generally, and for differently chosen system parameters the error may also remain constant along the wire. Still, for this particular QCA structure and for the chosen system parameters, we are relatively confident that the error of the output polarization, while not well controlled, will not grow very large for systems accessible with the Ising approximation—up to twelve QCA cells.

In this chapter we introduced and established three approximations for QCA systems:

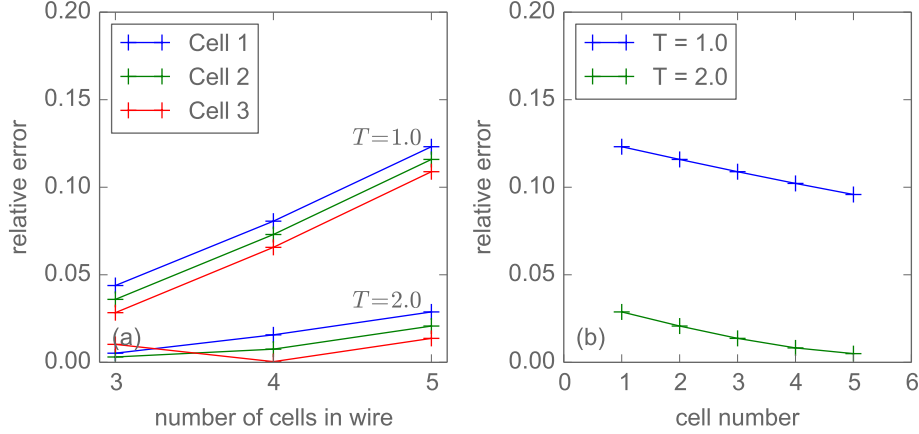


Figure 3.8: (a) The Ising model's relative error of the cell polarization for three-cell to five-cell charge-neutral wires at two different temperatures. The longer the wire the larger becomes the error. The error is no longer well controlled. (b) The Ising model's relative error for each cell's polarization in a five-cell charge-neutral wire. For the chosen parameters the error decreases along the wire. At least for the output polarization, the effect of a growing error with increasing wire length is therefore compensated.

the fixed-charge, the bond, and the Ising model. We usually use the fixed-charge model as the starting point, without further explicit verification. In principle, whether the fixed-charge approximation holds for a chosen set of parameters, has to be checked for each potential QCA implementation on a case by case basis. If the fixed-charge model is not applicable, then there is also generally no hope of implementing QCA on the given experimental system. We generally assume doubly occupied states to be sufficiently gapped out and put  $U$  at infinity. The bond approximation is then a very good description of QCA systems at high temperatures. It starts breaking down when the temperature becomes comparable to the singlet-triplet splitting, and therefore for small  $V_1$  and too large cell-cell distances. While it is conceptually rewarding to map QCA to an Ising system, we have seen the Ising approximation to be difficult to handle for practical calculations. It is only valid in a relatively small parameter window, at least for moderate system parameters, and great care has to be taken with its application. Generally speaking, both the bond and the Ising approximation become exact in the same limits—large  $V_1/t$  and small (but not too small) cell-cell distances. Not coincidentally, those are the limits where the QCA approach works best, as we will find out in the next chapter. Both approximations are useless for

low-temperature calculations, and for ground state properties we thus have to rely on the fixed-charge model, which only allows system sizes of up to three cells. We will use the bond model for most of our QCA characterization work at finite temperature. With system sizes of up to six cells, it already allows for some interesting insights. The Ising model is problematic and we will employ it sparingly and only to look at larger structures such as gates.

## Chapter 4

# Characterization

### 4.1 The three-cell wire

We choose a simple QCA system, the three-cell wire that we had already introduced in Fig. 2.5 in the second chapter, to investigate general time-independent characteristics of QCA circuits. Specifically, we are interested in how the polarization of one cell *responds* to the polarization of a second cell, and how cell polarizations depend on cell-cell distance and inter-cell angle. For the three-cell wire we use a nearest-neighbour Coulomb repulsion  $V_1 = 40$  and the cell-cell distance is  $d/a = 2.2$ , where  $a$  is the edge length of the cell. Most of our calculations will be at finite temperature,  $T = 1$ , and we will concentrate on horizontal wires for now (meaning the inter-cell angle is  $\theta = 0^\circ$ ). Both the Coulomb energy scale  $V_1$  and the temperature  $T$  are in units of the hopping  $t$ , with  $t = 1$ . For these parameters the bond approximation is valid, and we employ it unless otherwise noted. We investigate systems both without compensation charges  $q = 0$ , here the net cell charge is  $-2e$ , and with a compensation charge of  $q = \frac{1}{2}$ , yielding charge-neutral cells.

The driver cell sets the input for the three-cell wire, with its polarization  $P_D$  taking values in the range  $-1$  to  $+1$ . The three active cells respond to the driver polarization. For our discussion, we define the linear polarization response of cell  $k$  with respect to cell  $l$  as

$$\chi_{kl} = \left. \frac{\partial P_k}{\partial P_l} \right|_{P_l=0}. \quad (4.1)$$

Figure 4.1(a) and (b) show the polarization of the first cell with respect to the driver cell, the polarization of the second cell with respect to the first cell, and so on. For the



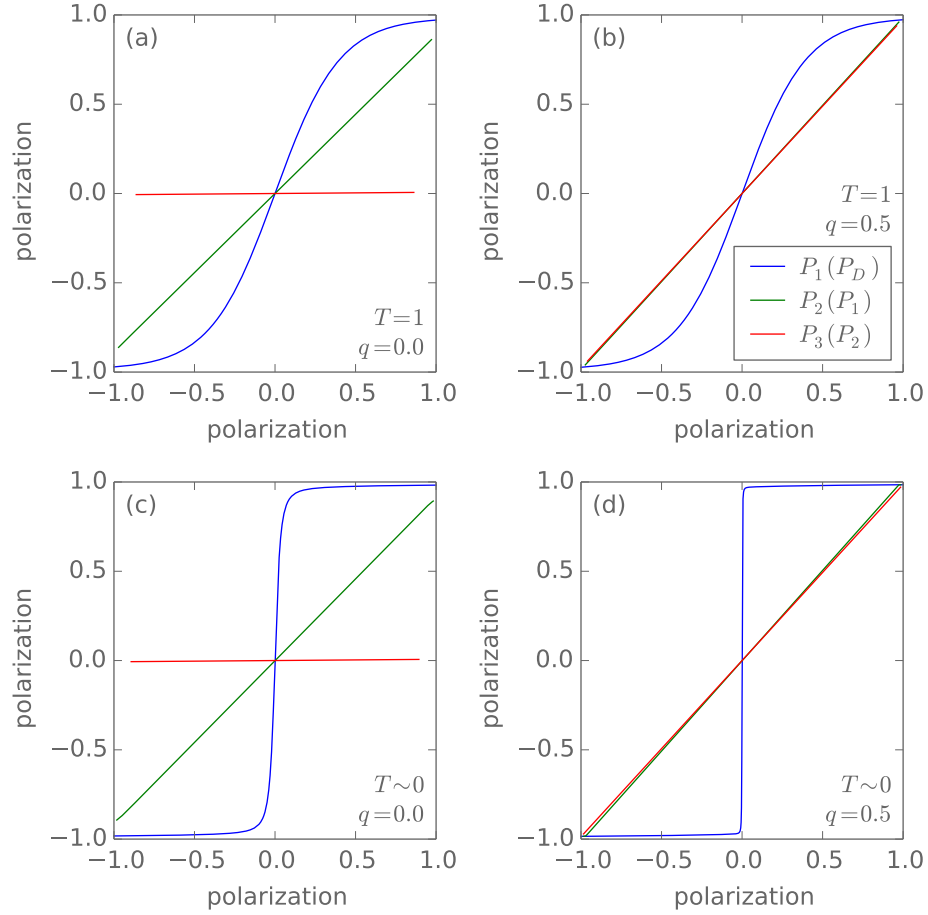


Figure 4.1: The cell-cell polarization response. The response of the first cell with respect to the driver cell is non-linear and exhibits gain. In contrast, the response of the second cell with respect to the first cell, and similarly for the third with respect to the second, is linear and without gain. At zero temperature, the responses are generally improved, but the qualitative behaviour remains the same.

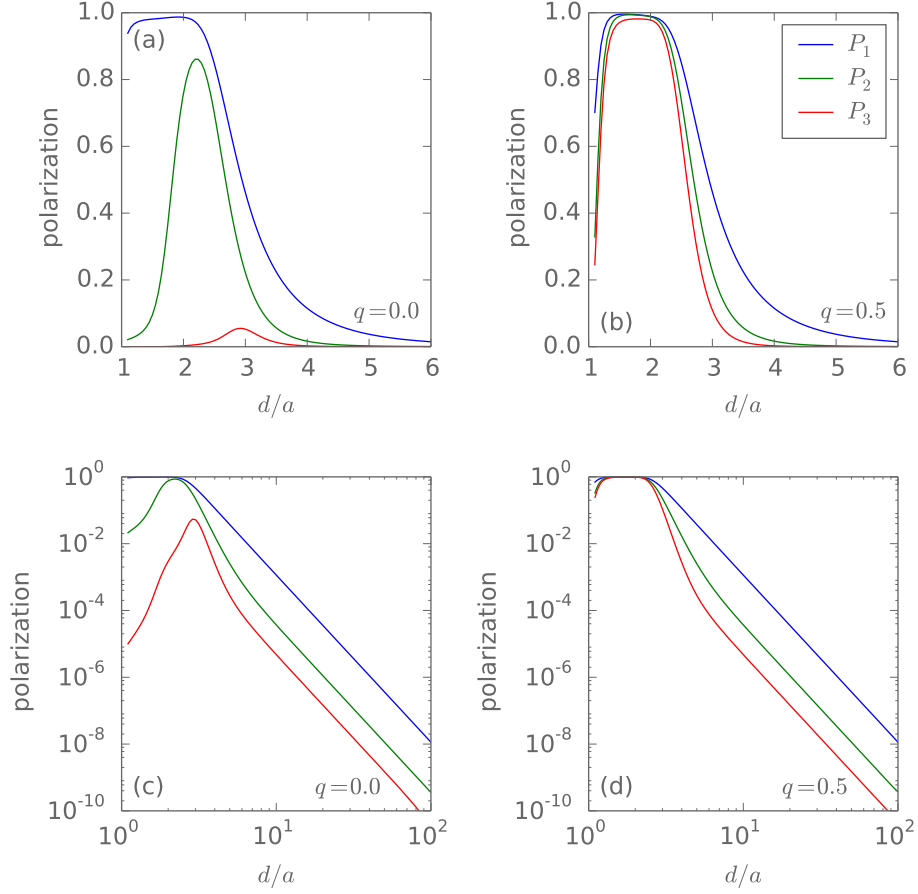


Figure 4.2: (a)(b) Cell polarization as a function of cell-cell distance. In the non-charge-neutral system ( $q = 0$ ), due to charge buildup the maximum polarization for consecutive cells is at increasingly large cell-cell distances. Even at optimal distance the output polarization  $P_3$  is very small. The output polarization is drastically improved for the charge-neutral system. Each cell attains its optimal polarization in the same range of cell-cell distances. (c)(d) Cell polarization over very large cell-cell distances. For large distances  $d/a > 10$  the polarizations settle into an universal long distance tail  $d^{-5}$ , independent of  $q$  and as predicted by the Ising interaction  $J$ .

first cell, the response is non-linear and shows gain, therefore  $\chi_{1D} > 1$ . In contrast, the polarization response between cells interior to the wire is linear and does not exhibit gain, i.e.  $\chi_{21} \leq 1$  and  $\chi_{32} \leq 1$ . Generally, the polarization decreases monotonically from cell to cell,  $|P_D| \geq |P_1| \geq |P_2| \geq |P_3|$ . In fact, for the  $q = 0$  system the polarization rapidly drops to zero for the chosen parameters. The transmission is much improved for charge neutral cells. In that case, the response is almost perfect,  $\chi_{21} \sim \chi_{32} \sim 1$ .

It is worth pointing out that at zero temperature, where we have to use the fixed-charge model rather than the inapplicable bond approximation, we observe the same polarization response characteristics, as demonstrated in Fig. 4.1(c) and (d). Quantitatively, for the same system parameters the response is improved at zero temperature compared to  $T = 1$ . For example, the first cell's polarization response becomes a near-perfect step function for the chosen parameters. But, importantly, it remains true that the response inside the wire ( $\chi_{21}, \chi_{32}$ ) is always linear and without gain. Without compensation charges, the polarization of the third cell remains zero even in the ground state, indicating that the cells are so closely spaced that charge buildup pushes the electrons of the rightmost cell to the rightmost edge.

In the literature, the non-linear nature of  $P_1(P_D)$  has been noted [21, 22], and the apparent gain  $\chi_{1D} > 1$  has been invoked to argue for the robustness and fault-tolerance of the QCA scheme. However, as our graph shows, this is only strictly true for the response with respect to the static-charge driver cell. We believe that the picture where each cell switches with gain with respect to its neighbours is an artefact of the intercellular Hartree approximation (ICHA), which we had introduced in more detail in Chapter 2. ICHA treats each cell individually in the static charge mean field of the other cells in the system. In other words, in the ICHA scheme, for each cell the rest of the system is approximated by an effective driver cell.

We now fix the driver polarization at  $P_D = 1$  and look at how the polarizations of the active cells depend on the cell-cell distance  $d/a$ , see Fig. 4.2(a) and (b). At  $d/a = 2$  all quantum dots in the system are equally spaced, cells are placed a distance  $a$  apart. At this separation and smaller, our basic assumption of no inter-cell hopping breaks down, as some dots in adjacent cells are now placed closer together than the dots inside each cell. Thus  $d/a \leq 2$  is an unphysical limit. Conversely, at very large cell-cell distances we expect the cells to become decoupled and therefore all polarizations to be zero. Obviously, neither extreme limit is of interest if our aim is to build functional QCA devices.

As already observed above, and in line with our intuition, polarizations generally de-

crease from cell to cell as we go further away from the driver cell. Without compensation charges ( $q = 0$ ) the polarization quickly falls off to very small values, whereas for charge neutral cells ( $q = \frac{1}{2}$ ) the situation is much improved. The graph shows that there is a cell-cell distance that yields maximal polarization for each cell. For the  $q = 0$  system—non-charge-neutral cells—the optimal distance increases from cell to cell, due to charge buildup. In contrast, with charge-neutral cells ( $q = \frac{1}{2}$ ) the cell-cell distance yielding optimal polarization does not change notably from cell to cell. In fact, here a range of distances gives very good polarizations, as the polarization saturates at values close to  $P = 1$ . Outside of this plateau region cell polarizations still fall off quickly towards zero, for example for cell-cell distances  $d/a \gtrsim 3$ . Of course, for a wire what really matters is the output polarization. For the chosen parameters, this calculation demonstrates that for a  $q = 0$  system we should choose  $d/a \sim 2.9$ . For  $q = \frac{1}{2}$  the range  $d/a \sim 1.3 \dots 2.3$  gives the best output polarization. Worryingly, this range is very close to the lower, unphysical limit!

Especially for the non-charge-neutral system, it is beneficial to allow for different distances between different adjacent cells along the wire. Thus a single  $d/a$  parameter is replaced by  $d_k/a$  with  $k = 1, 2, 3$  for the three-cell wire. Using a stochastic optimization scheme introduced by Sandvik *et al.* [64], we can optimize the  $d_k/a$  for optimal output polarization. We find that the output polarization is significantly improved from  $P_3 = 0.06$  for uniformly spaced cells to  $P_3 = 0.15$  for cells with individual cell-cell distances. For the uniform wire we find the optimal cell-cell distance  $d/a = 2.92$ , in agreement with Fig. 4.2(a), whereas the best distances for the non-uniform wire are  $d_1/a = 2.21$ ,  $d_2/a = 2.55$ , and  $d_3/a = 3.25$ . Not surprisingly, cells are farther spaced to the right (the output) and closer spaced to the left (the input). This is a manifestation of charge buildup in the system. The situation is very similar for longer wires and different parameters for non-charge-neutral wires. Of course, non-uniformly spaced cells have implications for the directionality of transport in a wire, which would have to be considered when designing QCA circuitry. More generally, we should be able to optimize the functionality of any given non-charge-neutral QCA layout by allowing for slightly adjustable cell placement. We can do the same stochastic optimization for charge-neutral wires ( $q = 1/2$ ), but find that little is gained by allowing non-uniform cell-cell distances. Looking at Fig. 4.2 this is really not surprising at all, and simply a consequence of having no charge buildup in the system. It should be emphasized how much better the output polarization is for charge-neutral wires. At least for the chosen parameters, even very short wires seem unrealistic for a non-charge-neutral system.

It is instructive to plot the polarizations over cell-cell distance up to very large distances in a log-log graph as shown in Fig. 4.2(c) and (d). Even though large distances come with extremely small polarizations that are not of practical interest, this graph yields valuable insights into the nature of the interaction that mediates the polarization. At distances  $d/a > 10$  we see that the polarization settles into an universal long range tail with  $P(d) \sim d^{-5}$ . This is consistent with our understanding that the polarization is mediated by a quadrupole-quadrupole interaction. For these large distances the polarization is exactly the same for both the  $q = 0$  and the  $q = \frac{1}{2}$  systems. Hence, having non-charge-neutral cells does not actually alter the characteristics of the cell-cell interaction. Instead, it suppresses the cell-cell interaction at small distances. That is, charge repulsion competes with the quadrupole interaction. The graph exactly confirms our analysis from Chapter 3. There, we had derived an approximate expression for the mediating cell-cell interaction in the Ising picture,  $J \sim d^{-5}$ , to leading order, and the derived  $J$  was independent of  $q$ . At the time we had seen that, in general, we can only map QCA to a modified Ising model with an additional cell-cell interaction  $J'$ , which does depend on  $q$ . However, for the horizontal wire,  $J'$  vanishes and we are left with the pure Ising model, and at large enough distances the behaviour of the polarization is just as predicted. Of course, we are mostly interested in small distances, where the polarization is relatively large. Here, the polarization falls off faster than  $d^{-5}$  and, remembering the derivation of  $J$ , we would need to include higher order corrections in the multipole expansion to accurately describe this behaviour. Even with higher order terms the Ising model and its  $J$  cannot, however, correctly reproduce the suppression of the quadrupole interaction at short distances in the case of  $q = 0$ .

From the discussion of the Ising model in Chapter 3, we already know that cell polarizations should change with the inter-cell angle. The polarizations are mediated by the cell-cell interactions  $J$  and  $J'$ , and specifically we had found  $J \sim \cos 4\theta$ , whereas  $J' \sim \sin 2\theta$ . We rotate the three-cell wire from a horizontal configuration ( $\theta = 0^\circ$ ) over diagonal ( $\theta = 45^\circ$ ) to vertical ( $\theta = 90^\circ$ ), and back to horizontal ( $\theta = 180^\circ$ ), and look at the cell polarizations in the process. Figure 4.3(b) shows the polarization as a function of the angle for the charge-neutral system, where  $J' = 0$ . Indeed, the cell polarizations follow the behaviour predicted by  $J$ : they are rotationally invariant under rotations by  $90^\circ$  and peak at the angles  $0^\circ, 90^\circ$ , and so on, where  $J > 0$ . At  $45^\circ$ , where  $J < 0$ , cell polarizations are alternating, e.g.  $P_D \sim 1$ ,  $P_1 \sim -1$ ,  $P_2 \sim 1$ , and  $P_3 \sim -1$ . In between, for example at  $\theta = 22.5^\circ$ ,  $J = 0$  and the polarization is zero accordingly. The wire can be used to transmit signals in a range of about  $20^\circ$  around  $\theta = n \cdot 45^\circ$ , where  $n$  is an integer and the usable angle

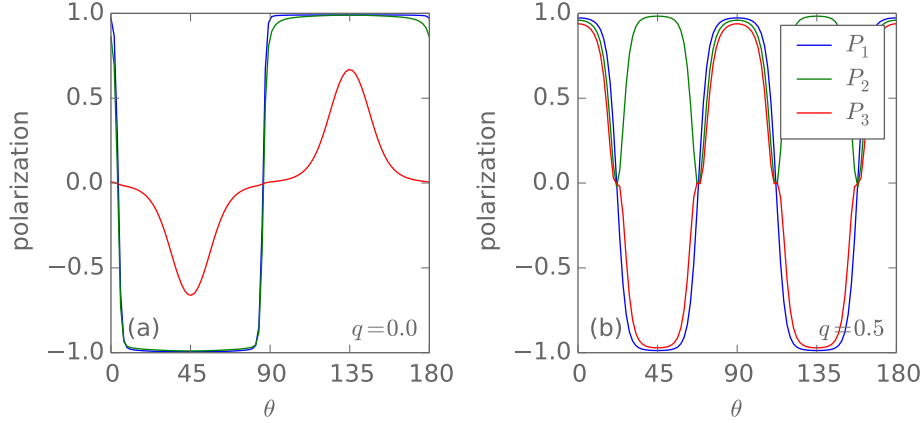


Figure 4.3: Cell polarization over the inter-cell angle. The charge-neutral system is invariant under rotations by  $90^\circ$  and closely matches the behaviour predicted by the Ising  $J$ . At  $45^\circ$  cell polarizations are alternating. For the non-charge-neutral system, the polarizations are predominantly set by the angle, and not by the driver polarization. The system is invariant under rotations by  $180^\circ$ , as predicted by the modified Ising  $J'$ . In the non-charge-neutral case QCA does not work at all, except for horizontal or vertical wires.

range depends on the chosen system parameters. Of course, at  $45^\circ$  we have to make sure to use an even number of cells for transmission, as the signal will be inverted otherwise. Conceivably, the nodes at  $22.5^\circ, 67.5^\circ$ , and so on could be used to decouple closely spaced cells.

The situation is very different for non-charge-neutral systems, as shown in Fig. 4.3(a). In this case,  $J' \neq 0$  and we see that the polarization is actually predominantly set by  $J'$ , which is rotationally invariant under rotations by  $180^\circ$ . This is in line with our derivation where we had found, to leading order,  $J' \sim d^{-3}$ , whereas  $J \sim d^{-5}$ , and thus,  $J'$  was expected to dominate. The graph shows that the cell polarizations are much larger in magnitude away from  $0^\circ, 90^\circ$ , and so on, where we know that the system behaves as expected. In fact, the presented graph looks exactly the same for  $P_D = 1$  and  $P_D = -1$ , except for a small range of angles of about  $5^\circ$  around  $\theta = n \cdot 90^\circ$ , where the angle range again depends on the chosen system parameters. In short, the cells' polarizations are set by the inter-cell angle and not by the driver polarization. The importance of charge neutrality had first emerged in our discussion of the Ising model. Here we see this finding most impressively confirmed. The non-charge-neutral system will never work as a QCA

circuit unless all we want to do is build linear chains of cells. Even in this case the system becomes very fragile with respect to angular displacement. Thus, for QCA charge-neutral cells,  $q = \frac{1}{2}$ , are absolutely essential. In the literature charge neutrality has usually been assumed, either explicitly or implicitly, but as far as we know, no one else has previously identified its crucial role.

## 4.2 Workable parameters for QCA

In the previous section we found charge-neutral cells to be essential for QCA. Therefore we will from now on restrict ourselves to  $q = \frac{1}{2}$  systems. Additionally, we saw that in a line of cells the polarization is at best preserved but generally decreases from cell to cell. There is no inter-cell gain. If the cell-cell polarization response is less than ideal then the polarization will eventually decrease to zero for a long line of cells, rendering the wire non-functional. It is therefore important to identify a parameter regime where the response is ideal or close-to-ideal as a prerequisite for functional QCA circuits.

We use a cluster mean field approach beyond the single-site ICHA approximation to calculate the polarizations of semi-infinite wires. A small cluster of active cells is embedded in a large number of driver cells—the mean field—whose polarization is set as the average of the active cells. The setup is illustrated in Fig. 4.4 for three active cells. Therefore, instead of solving only the one-cell mean field Hamiltonian  $H_k^{\text{MF}}$  (2.7) introduced in section 2.4, as for the ICHA scheme, we solve a cluster mean field Hamiltonian  $H^{\text{MF}}$ , and instead of only using a single cell’s polarization  $P_k$ , the average of all active cells  $\langle P_k \rangle$  is used to set the mean field  $P_D$ . The self-consistency condition then is

$$P_D = \langle P_k (P_D) \rangle . \quad (4.2)$$

If we don’t find a solution for the self-consistency condition for a given set of parameters then only the trivial solution  $P_D = 0$  remains. In this case no self-consistent polarization exists.

We made a point of how problematic mean field approximations can be. Here we use the approach to establish a *lower bound* on workable parameters. In principle, the number of active cells can be indefinitely increased and properties of interest can be extrapolated to the thermodynamic limit; the approximation is asymptotically correct. Of course, in practice the number of active cells allowed by the available computer resources is actually

quite small and probably far from the asymptotic behaviour.

We have found that as few as ten driver cells on each side of the active cells already look like an infinite wire. Adding more and more driver cells, the active cells' polarizations quickly saturates, indicating that they don't "see" cells farther away than ten cells. This also shows that in practice the interaction, while beyond nearest-neighbour, is not extremely long-ranged. In the following calculations we use 100 driver cells on each side of the active cells.

We now use a larger cell-cell distance  $d/a = 3.0$  and a higher temperature  $T = 2$ , and calculate the self-consistent polarization with three active cells over a wide range of values of  $V_1$ , shown in Fig. 4.5(a). We observe a second-order phase transition at  $V_{1\text{crit}}$ . For  $V_1 < V_{1\text{crit}}$  no self-consistent solution with  $P_D > 0$  exists. This regime is therefore inhibitive for QCA devices. Above the critical  $V_1$  the polarization rises very sharply and quickly saturates towards full polarization. The presence of a phase transition is likely an artefact of the mean field method. Still, the scale of the critical  $V_1$  sheds light on what order of magnitude to expect for a workable  $V_1$ . For our system, we find that  $V_1 \gtrsim 150$  should yield large cell polarizations, and as before this is in units of the hopping, with  $t = 1$ . For more favourably chosen parameters the critical  $V_1$  can also be much smaller. Table 4.1 lists the  $V_{1\text{crit}}$  for a variety of different system parameters. In particular, for the parameters used for the three-cell wire in the last section,  $T = 1$  and  $d/a = 2.2$ , the critical  $V_1$  is only  $V_{1\text{crit}} = 14.71$ . The table also demonstrates that the critical  $V_1$  grows very rapidly for larger cell-cell distances. This is in line with what we had seen in Fig. 4.2(a) and (b), where we had plotted the cell polarizations as a function of the cell-cell distance. In that graph, after a plateau-like feature at small distances, the polarization had dropped off very quickly with growing inter-cell spacing. Both observations emphasize that small cell-cell distances are crucial, and, generally, we want distances as small as possible while still satisfying our underlying physical assumptions, such as no inter-cell hopping. Let us note that a graph qualitatively similar in appearance to Fig. 4.5(a), obtained from single-cell ICHA calculations for a seven-cell wire, has been reported in the literature previously [22]. However, the reference's interpretation of the graph is lacking. In particular, the significance and consequences of employing a mean field scheme were not understood, and the critical values were therefore not identified as lower boundaries, but taken at face value.

We now investigate how the critical  $V_1$  changes with the number of active cells and whether we can extrapolate to the thermodynamic limit, where the mean field scheme



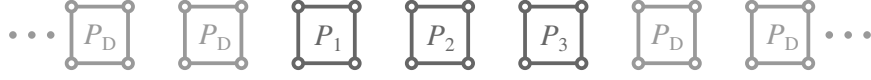


Figure 4.4: Semi-infinite wire. A small number of active cells is embedded in a large number of driver cells on both sides. The driver cells' polarization is determined self-consistently from the polarization of the active cells. This mean-field approach allows to establish a lower bound  $V_{1\text{crit}}$  for workable nearest-neighbour Coulomb energies  $V_1$ .

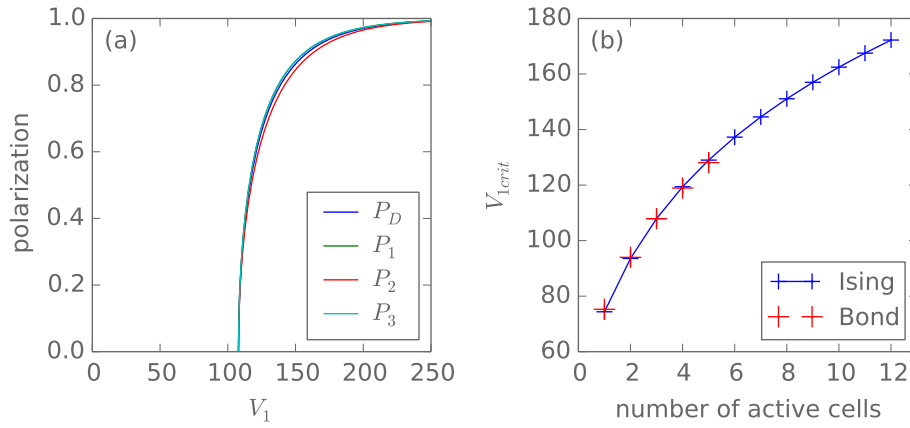


Figure 4.5: (a) Self-consistent polarization of a charge-neutral semi-infinite wire with three active cells. The cell-cell distance is  $d/a = 3.0$ , the temperature is  $T = 2$ . Below a critical  $V_1$  no self-consistent solution exists and the polarization is zero throughout the wire. Above the critical  $V_1$  the polarization grows quickly and saturates towards a perfectly polarized wire. (b) The critical  $V_1$  as a function of the number of active cells in the same semi-infinite wire: it grows monotonically and is expected to become infinite in the thermodynamic limit. For larger numbers of active cells the Ising model has to be used. Calculations with the bond model are included for comparison.

$T$	$d/a$	$V_{1\text{crit}}$	$T$	$d/a$	$V_{1\text{crit}}$
1	2.2	14.71	2	2.2	25.99
1	3.0	55.10	2	3.0	107.90
1	4.0	230.24	2	4.0	459.87

Table 4.1: The critical  $V_1$  obtained from bond model calculations with three active cells for a number of different charge-neutral systems.

becomes exact. Figure 4.5(b) traces  $V_{1\text{crit}}$  as the number of active cells is increased. With the more accurate bond model only up to five cells are computationally feasible, and we have therefore included calculations with the Ising model for up to twelve active cells. For the chosen system parameters, the obtained values of the critical  $V_1$  are relatively large and the Ising model is therefore expected to give sufficiently accurate results. Comparing the bond and Ising model in the graph, we see that they indeed agree well. The bond model gives slightly larger  $V_{1\text{crit}}$  than the Ising model for one and two active cells, but for four and five active cells the situation is reversed. Therefore, extrapolating the trend, we believe that the Ising model slightly overestimates the critical  $V_1$  for larger numbers of active cells. This is in line with our observation in section 3.4 that the Ising model generally underestimates the polarization. Most importantly, the graph shows that the critical  $V_1$  grows monotonically and substantially with an increasing number of active cells. For the chosen parameters, the  $V_{1\text{crit}}$  for twelve active cells is more than twice the  $V_{1\text{crit}}$  for only one active cell. The critical  $V_1$  grows more slowly for larger numbers of active cells, but does not saturate, and there is no clear identifiable scaling behaviour otherwise. Therefore, we strongly suspect that the  $V_1$  grows indefinitely and becomes infinite in the thermodynamic limit. Conversely, for a finite  $V_1$  the polarization of the infinitely long wire will be zero.

We used a mean field semi-infinite wire to obtain a lower bound  $V_{1\text{crit}}$  for workable  $V_1$  values. But we find that the  $V_{1\text{crit}}$  grows significantly with the number of active cells and in fact eventually becomes infinite. The  $V_{1\text{crit}}$  should still yield a valid scale for finite size QCA systems, presumably of a size comparable to the number of active cells in the mean field scheme, and certainly  $V_1 < V_{1\text{crit}}$  is a range where QCA is non-functional. More importantly though, the fact that no finite thermodynamic limit exists implies that perfect cell-cell response is impossible—the polarization along the wire will always decrease monotonically—and that QCA systems are limited in size. We already know from entropy arguments, laid out in section 2.1, that we cannot build infinitely large QCA systems, so having a second size bound is not a show stopper. The crucial question is whether we can achieve device units large enough in size to do practical computations.

To put into perspective the mean field  $V_{1\text{crit}}$  values we found for small QCA systems, we calculate the cell polarizations in two- to twelve-cell wires at  $V_1 = 200$ —well above all the  $V_{1\text{crit}}$  values in Fig. 4.5(b)—and with a driver polarization of  $P_D = 1$ . According to Fig. 4.5(a), which was calculated for three active cells, at  $V_1 = 200$  we should have a self-consistent average polarization of  $\langle P_k \rangle = 0.97$  throughout the semi-infinite wire. However, in an actual wire the cell polarizations are not constant, but drop off quickly and are also

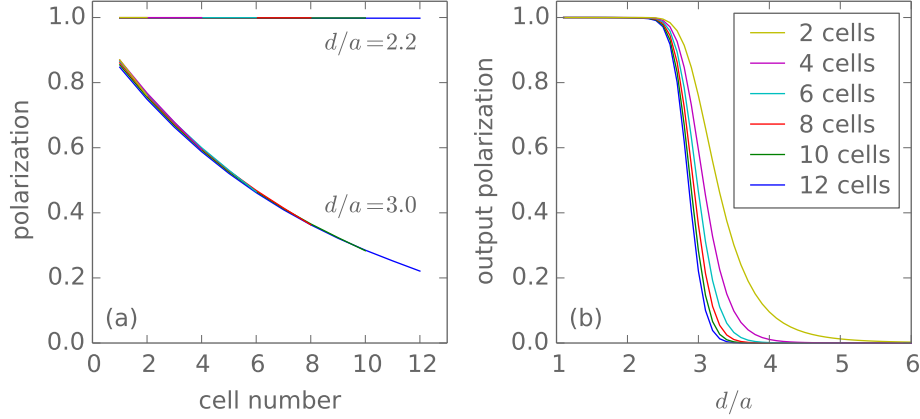


Figure 4.6: (a) Cell polarizations of two-, four-, six-, eight-, ten-, and twelve-cell wires for two different cell-cell distances at  $V_1 = 200$  and  $T = 2$ . Individual cell polarizations are hardly changed as the wire is made longer. The polarizations for the  $d/a = 2.2$  wire are essentially perfect. (b) Output polarization over cell-cell distance for the same two- to twelve-cell wires. The output polarization is perfect in a plateau-like region at small distances. For larger distances,  $d/a \gtrsim 2.5$ , the polarization very quickly drops to zero.

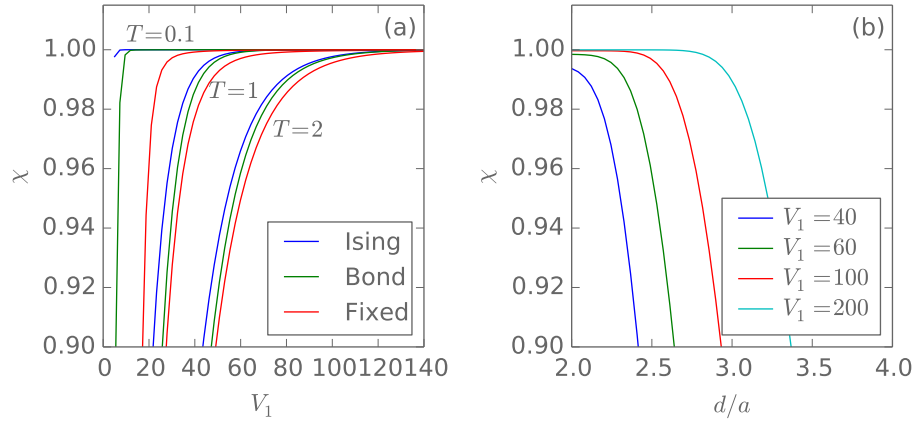


Figure 4.7: (a) The cell-cell response over the Coulomb energy  $V_1$  at different temperatures and calculated with different models and wires. The cell-cell distance is  $d/a = 2.2$ . The fixed-charge wire slightly underestimates the in-wire response, but is otherwise the most accurate model over the whole parameter range. The minimum  $V_1$  required for close-to-perfect response increases with temperature. (b) The cell-cell response of the fixed-charge wire over cell-cell distance at  $T = 1$ . The distance range yielding close-to-perfect response increases with the Coulomb energy  $V_1$ .

much smaller, as shown in Fig. 4.6(a) in the  $d/a = 3.0$  curve. For a six-cell wire the output polarization is already less than half of the input polarization, for twelve cells it is almost a fifth. The graph strongly suggests that the polarization will continue to drop to zero for longer wires. It therefore becomes apparent that the mean field  $V_{1\text{crit}}$  really does set a lower boundary, and in practice significantly larger  $V_1$  values are necessary for functional QCA devices, even for relatively small systems.

Figure 4.6(a) also includes cell polarizations for wires with a cell-cell distance  $d/a = 2.2$ . For these systems, Table 4.1 lists  $V_{1\text{crit}} = 25.99$ , which was determined for three active cells in a semi-infinite wire. An Ising model calculation with twelve active cells yields  $V_{1\text{crit}} \sim 45$ , which likely overestimates the critical  $V_1$  and, for these small  $V_1$  values, should really be taken as a very rough guideline. At  $V_1 = 200$  we are therefore almost an order of magnitude larger than the critical  $V_1$ . At these shorter cell-cell distances the cell polarizations are essentially perfect for all two- to twelve-cell wires. When we zoom in, however, we find that the behaviour is qualitatively the same as for the  $d/a = 3.0$  wires: the polarizations still decrease monotonically along the wire. But quantitatively the short cell-cell distance is quite a different story. The polarizations fall off so slowly, that we can reasonably expect to achieve sufficiently large output polarizations for very long wires. To investigate the astounding quantitative difference between the two systems, we again plot the polarization over cell-cell distance. Figure 4.6(b) shows the output polarization of two- to twelve-cell wires. The graph looks qualitatively similar to Fig. 4.2(b) from the last section: for small distances the output polarization is close to perfect in a plateau-like region, but for  $d/a \gtrsim 2.5$  rapidly drops to zero. And it drops increasingly faster to zero for longer wires. Therefore, for large, functional QCA devices we want to make sure we operate in the plateau-like regime at small distances.

The cell polarization curves for all two- to twelve-cell wires in Fig. 4.6(a) almost lie on top of each other, implying that the polarizations of existing cells hardly change as the wire is made longer by adding more cells to the right. We can directly inspect the cell polarization responses along the wire  $\chi_{i,i-1}$  and find that they are almost constant, with the exception of the first cell which responds to the driver cell and therefore behaves differently, and the last two cells, which have slightly lower responses, due to edge effects. Additionally, the responses are largely independent of the driver polarization, with the exception of the response of the first cell,  $\chi_{1D}$ , of course, which we also find to decrease for longer wires. The observed behaviour matches our intuition: we know that the cell polarization responses interior to the wire are linear. Symmetry suggests that the responses

of cells far from the edges in a long wire should be the same. Therefore, we are inspired to fit the cell polarization curves to a simple physical model,

$$P_k = \chi_e(P_D) \chi^k P_D. \quad (4.3)$$

Here,  $P_k$  is the polarization of cell  $k$  in the wire,  $\chi$  is the polarization response which is assumed to be the same for all cells in the wire, and  $\chi_e(P_D)$  is the system response to the driver cell polarization  $P_D$ . If the response to the driver cell was the same as for a regular cell, then we would have  $\chi_e(P_D) = 1$ . We fit this model to the polarization curves, with  $P_D = 1$  fixed, and find that it works surprisingly well. Averaging over all wires, we find  $\chi_e = 0.999114(8)$  and  $\chi = 0.999997(0)$  for  $d/a = 2.2$ , and  $\chi_e = 0.97(4)$  and  $\chi = 0.884(0)$  for  $d/a = 3.0$ . Similar to  $\chi_{1D}$ ,  $\chi_e$  decreases slightly for longer wires, whereas  $\chi$  is almost perfectly constant (it increases very, very slightly with wire length). If the model worked perfectly then both parameters would be the same for all wires, but given that the model is so simple, we feel that it works reasonably well, and over a range of system parameters. The assumption of constant cell responses throughout the wire starts to break down for larger cell-cell distances  $d/a \gtrsim 4$ , where the actual polarizations are already very small for a majority of the cells.

The graph in Fig. 4.6(b) can be readily understood using the simple model (4.3). In the plateau region at small cell-cell distances the cell responses interior to the wire are close to perfect,  $\chi \sim 1$ . For larger distances,  $\chi < 1$  and therefore the polarization  $P_k \sim \chi^k$  quickly falls off to zero for long wires. For very long wires we expect the figure to resemble a step function. While  $\chi$  does not depend on the driver polarization, it does depend on other system parameters, like  $d/a$  and  $V_1$ , and to be able to scale up to large system sizes we want  $\chi \sim 1$  and have to choose the parameters accordingly.

We can use the found values for  $\chi_e$  and  $\chi$  to roughly estimate how long we can make the wires before the output polarization falls below a certain threshold. More generally, this gives an approximate upper size for QCA devices for the chosen system parameters. Averaging  $\chi_e$  and  $\chi$  over the two- to twelve-cell wires, for the wire with  $d/a = 3.0$  we find that the output polarization drops below  $0.1P_D$  after 18 cells. As the graph demonstrates the output polarization already drops below  $0.9P_D$  before the first cell. In contrast, with a cell-cell distance of  $d/a = 2.2$ , the output polarization is above  $0.9P_D$  for up to 35,040 cells, and above  $0.1P_D$  for up to a staggering 771,988 cells. These are very simple estimates that could likely be improved, for example by extrapolating  $\chi_e$  in a better way, but even if the

numbers are wrong by a factor of two or three, the improvement from  $d/a = 3.0$  to  $d/a = 2.2$  is most dramatic. For the smaller cell-cell distance the potentially achievable system sizes are orders of magnitude larger than for the larger cell spacing. With something like 30,000 cells we can clearly build practical circuit units that perform meaningful computations.

Our calculations show that the model  $P_k \sim \chi^k$  is the right physical picture for QCA wires, and by cranking up the system's parameters we will be able to push the response increasingly close to perfect. Truly perfect response, with  $\chi = 1$ , however, is not possible. As a consequence, in the thermodynamic limit the polarization will always be zero. This picture agrees with our observations of the critical  $V_1$ , which we had seen to grow to infinity for infinitely large systems. Therefore, the polarization inside a wire is never truly constant, but always decreases, if very slowly. The picture of constantly and fully polarized QCA systems employed in the literature is qualitatively wrong. Of course, by choosing the right system parameters and making  $\chi$  large enough, we can, in principle, achieve system sizes that should be more than sufficient to build practical device units.

We have shown explicitly that a set of parameters exists where QCA works well up to large system sizes:  $V_1/t = 200$ ,  $T/t = 2$ , and  $d/a = 2.2$ . These parameters are rather extreme and were partly chosen so that the Ising approximation is valid, which allowed us to do calculations with wires of up to twelve cells. For practical QCA implementations, however, it is important to identify minimal workable parameters, specifically a minimal  $V_1$  and a range of cell-cell distances at a given temperature. The mean field  $V_{1\text{crit}}$  is an indicative value, of course, but we have just seen that it is ultimately not very reliable. Following the simple model (4.3), we can calculate the cell-cell response  $\chi$  in short wires with more accurate models over wide parameter ranges and use this short-wire response as an estimate for the response inside very long wires. According to the model, those responses should be exactly the same. In practice, there are small differences due to more pronounced edge effects in short wires.

Figure 4.7(a) shows the cell-cell response over  $V_1$  for three different temperatures and for three different wires and models. Specifically, the  $\chi$  is calculated as the response of the sixth cell in an eight-cell wire with the Ising model, as the response of the third cell in a four-cell wire with the bond model, and as the response of the second cell in a two-cell wire with the fixed-charge model, which is the most accurate model of the three. If the assumption of constant  $\chi$  for all wires is true, and if we are additionally in a parameter regime where all three approximations become exact, then all three curves should agree. The presented calculation uses a cell-cell distance  $d/a = 2.2$  and very small driver cell

polarizations  $P_D = 0.01$ . The latter is chosen so that cell polarizations do not saturate,  $P_k < 1$ , over the whole parameter range.

For all three temperatures, the responses of the Ising, bond, and fixed-charge wires all agree at large enough  $V_1$ , where we find  $\chi \sim 1$ . Concentrating on the  $T = 2$  curves, we see that bond and Ising agree for  $V_1 \gtrsim 100$ —where the Ising model becomes accurate—and their responses become close to perfect around  $V_1 \sim 120$ . In contrast, the fixed-charge  $\chi$  is slightly smaller and only achieves  $\chi \sim 1$  around  $V_1 \sim 140$ . In this regime, the bond and Ising model are both accurate, and the difference between those two models'  $\chi$  and the fixed-charge model's  $\chi$  is due to edge effects of the shorter two-cell fixed-charge wire. Thus, while the fixed-charge two-cell  $\chi$  slightly underestimates the response in longer wires, it clearly follows the trend of the other two models and can therefore be used as a good estimate for the in-wire response in longer wires. At  $T = 0.1$ , for example, bond and Ising model are no longer valid and give wrong results. The fixed-charge model indicates that even at these small temperatures, perfect response is only achieved for  $V_1 > V_{1min}$  with  $V_{1min} \sim 20$ , and this is also the minimum  $V_1$  for any temperature. For  $T = 1$  and  $T = 2$ , we find  $V_{1min} \sim 60$  and  $V_{1min} \sim 120$ , respectively.

We investigate how  $\chi$  depends on the cell-cell distance. Figure 4.7(b) plots the fixed-charge two-wire response over the cell-cell distance at  $T = 1.0$  and for different values of  $V_1$ . Clearly, the cell-cell distance range yielding  $\chi \sim 1$  depends on the Coulomb energy  $V_1$ : the larger  $V_1$ , the larger the distance range. In agreement with Fig. 4.7(a), the graph demonstrates that at  $V_1 = 40$  close-to-perfect response is not possible, even when going down to the lower physical inter-cell distance limit  $d/a = 2.0$ . While  $V_1 \sim 60$  is workable,  $V_1 \sim 100$  seems like a comfortable regime where a range of cell-cell distances  $2.0 < d/a < 2.5$  yield very good cell-cell responses. The figure remains qualitatively unchanged at different temperatures. We find that the  $\chi \sim 1$  distance range increase for lower temperatures, as can be expected. However, at  $T = 0.1$  and  $V_1 = 20$  we cannot achieve close-to-perfect response at any cell-cell distance. Therefore,  $V_{1min} \sim 20$  really is the lower limit for operational QCA devices, at all temperatures. In summary, Fig. 4.7 provides us with rough estimates for minimal workable parameters, and we have used a loosely defined close-to-perfect polarization  $\chi > 0.99$  to establish them. As discussed above, how close to perfect is good enough depends on the desired system sizes. However, we saw that for  $\chi \lesssim 0.9$  only very small systems are realistically achievable, and for  $V_1 < V_{1min}$  the response quickly drops below that mark.

We have used dimensionless parameters throughout. In the extended Hubbard model,

the energy scale is set by the hopping parameter, and we have chosen  $t = 1$ . We use  $V_1$  to characterize the Coulombic energies and found that very large  $V_1/t$  is a requirement for QCA. This Coulomb energy is set directly by the cell size,  $V_1 = 1/a$ . Therefore, to achieve a very large  $V_1$ , we need either very small cell sizes or a very small hopping  $t$ . Of course, as the overlap integral the hopping  $t$  also depends on the distance between quantum dots, and thus the cell size. In a highly idealized system we can assume the overlap integral to decay exponentially with dot-dot distance, whereas the Coulomb interaction falls off as  $1/r$ . Therefore, in principle, we can achieve the required large  $V_1/t$  ratios simply by making the QCA cells large enough. In practice, even if such an engineered  $V_1/t$  ratio were achievable, we might not gain much from it. An increasingly small  $t$  would “freeze” the system: dynamics would be very slow, greatly reducing the usefulness for computation. The temperature is also in units of the hopping parameter, and a small  $t$  therefore potentially brings down the temperature to the cryogenic regime. Lastly, bringing down the overall energy scales by reducing  $t$  presumably would make the device more susceptible to external perturbations in a less-than-perfect material system.

To put the minimal workable parameters we have found in a more tangible context, we return to the atomic silicon quantum dots which we introduced in detail in Section 2.2. Even though this system is quite different from our model—it uses six electrons per cell instead of two, and, more importantly, is not charge neutral—it is close enough to get a rough idea of what real world numbers might look like. Using *ab initio* estimates from reference [40] for the hopping rate  $t$  and the Coulomb repulsion  $V_1$  at various dot-dot distances, and fitting the data with the simple assumptions  $t \sim e^{-ba}$  and  $V_1 \sim ba^{-1}$  ( $b \approx 0.2$  and  $b \approx 1.2$ , respectively), where  $b$  is a fit parameter and  $a$  the dot-dot separation, allows us to provide approximative dot-dot distances for the  $V_1/t$  ratios we have used. For example, to achieve  $V_1/t = 100$  would require a dot-dot distance and hence cell size of roughly  $a \approx 32\text{\AA}$ , yielding a hopping rate  $t \approx 0.4\text{meV}$  and a Coulomb repulsion  $V_1 \approx 40\text{meV}$ . At  $T/t = 1$ , this corresponds to a temperature  $T \approx 4\text{K}$ . We had found the absolute minimum  $V_1$  to be  $V_{1\text{min}}/t = 20$ , requiring  $T/t \lesssim 0.1$ . This would correspond to a dot-dot distance  $a \approx 22\text{\AA}$ , a hopping rate  $t \approx 3\text{meV}$ , a Coulomb repulsion  $V_1 \approx 60\text{meV}$ , and a temperature  $T = 3\text{K}$ . For comparison, for the atomic silicon quantum dots the on-site Hubbard repulsion has been estimated to be  $U \approx 500\text{meV}$ . While these are very rough estimates, they still illustrate the challenge posed for experimental systems by the large parameters required for QCA operation. On the silicon (100) surface the dimer-dimer distance is  $a = 3.84\text{\AA}$ —the closest possible spacing for two quantum dots. Therefore, the



estimated dot separations correspond to six to eight lattice spacings. The hopping constant becomes very small and as a consequence the operational temperature moves to the single-digit Kelvin regime. This is markedly different from the experiments and envisioned setup of the group of Wolkow *et al.*, illustrated with a few examples in Fig. 2.4, where dots are placed close to each other and room temperature is used.

### 4.3 The majority gate

In the last section we identified a set of parameters for which the QCA approach works very well up to large system sizes, specifically  $T = 2$ ,  $V_1 = 200$ ,  $q = 1/2$ , and  $d/a = 2.2$ , with, as always  $t = 1$ . For these parameters, we can use the Ising model with good accuracy. It is instructive to look at more complex QCA structures than the simple horizontal wire, and we pick the majority gate—the single most important QCA logic device—as an example. The setup is illustrated in Fig. 2.2(a). The inputs are set with the driver cell polarizations  $I_1$ ,  $I_2$ , and  $I_3$ ; the gate output is the polarization of the rightmost cell, denoted by  $O$ . Each input lead consists of two active cells, and similarly there are two cells for the output lead, for a total of nine active cells. The polarizations of the input leads are understood to “vote” on the central device cell, with the majority polarization winning and setting the final output. We test the AND and OR functionality of the gate by fixing one of its inputs to  $-1$  and  $1$ , respectively, and we use  $I_2$  as the fixed input, for symmetry reasons.

Figure 4.8(a) and (b) show the output polarization as a function of the two inputs for AND and OR gate configurations. Because the response to driver cells is strongly non-linear, we do not plot directly against  $I_1$  and  $I_3$ , but use instead the polarizations  $I'_1$  and  $I'_3$  of the cells right next to the driver cells, i.e. the topmost and bottommost active cells. This gives a more accurate picture for a gate in a large circuit, far from the input driver cells. The gate implements the truth table of  $I_1 \wedge I_3$  and  $I_1 \vee I_3$  correctly, for example  $1 \wedge 1 = 1$  and  $1 \wedge -1 = -1$ . Unsurprisingly, the gate inherits the linear cell-cell response, and therefore switches completely linearly with the input polarizations. As an example,  $0.5 \wedge 0.5 = 0.5$ , and perfect output polarization is only achieved for perfect input polarization. There is no input threshold: any  $I_{1,3} > 0$  is treated as a logic 1 state, and any  $I_{1,3} < 0$  corresponds to logic 0. This is reflected by the fact that the zero contour line exactly traces the outline of the upper right and lower left quadrant for AND and OR gate, respectively.

We gain further insight into the characteristics of the QCA majority gate by operating it slightly outside of the optimal parameter regime. Figure 4.8(c) and (d) show again the

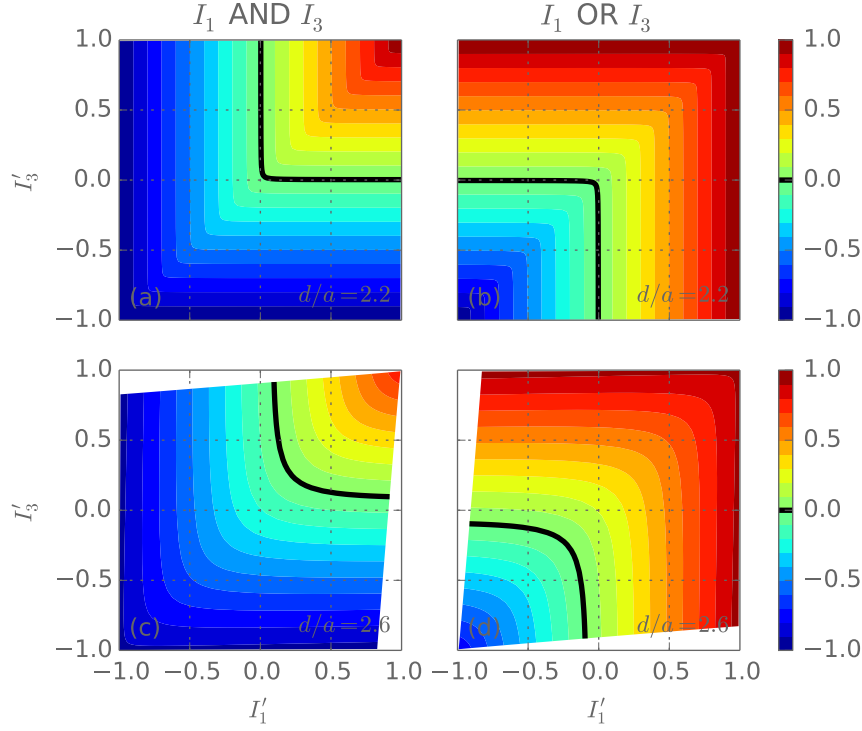


Figure 4.8: Output polarization  $O$  over input polarizations  $I'_1$  and  $I'_3$  of a majority gate in AND (with  $I_2 = -1$ ) and OR (with  $I_2 = 1$ ) configuration. (a)(b) The majority gate with a cell-cell distance  $d/a = 2.2$ . The gate correctly reproduces the AND and OR truth tables. The output polarization is linear with both input polarizations. (c)(d) The majority gate with a cell-cell distance  $d/a = 2.6$ —slightly outside the optimal parameter regime. The output polarization range becomes asymmetric with respect to the input polarizations. A non-zero input threshold is introduced.

output polarization for AND and OR gate configurations, but now at a larger cell-cell distance  $d/a = 2.6$ . As can be expected, the output of the gate no longer spans the whole polarization range from  $-1$  to  $+1$ . The output range becomes asymmetric with respect to the input range, for example  $1 \wedge 1 \sim 0.8$ , but  $-1 \wedge -1 \sim -1$ . Similarly, we find that now there is a threshold  $I_{\text{th}} \sim 0.2$ , where we require  $|I_{1,3}| > I_{\text{th}}$  so that the output is correct. Below the threshold, the gate switches incorrectly, for example  $0.1 \wedge 0.1 \sim -0.1$ . This asymmetry is understood by considering the geometry of the gate. The cells of the input leads  $I_1$  and  $I_3$  couple diagonally to the output lead and therefore induce a polarization that is opposite to their own. Outside of the optimal parameter regime, polarizations generally decrease from cell to cell, starting from the driver cells. Thus, at larger cell-cell distances where the central cell is only relatively weakly polarized, the influence of the more strongly polarized input leads on the output lead becomes more important and consequently decreases the overall output polarization and introduces a threshold. In this regime, if instead of the symmetric  $I_2$  one of the other two inputs,  $I_1$  or  $I_3$ , is used as the fixed input, then the output polarization also becomes asymmetric with respect to switching the inputs.

Because QCA has no in-built directionality, different inputs are not decoupled from each other. For example, the driver cell  $I_3$  influences cells in the lead of input  $I_1$ . This aspect is not directly captured by the graphs presented. These are plotted against the effective cell polarizations  $I'_1$  and  $I'_3$ , which are directly or indirectly set by all three driver cell polarizations  $I_1$ ,  $I_2$ , and  $I_3$ . But as a consequence, the ranges of the inputs  $I'_1$  and  $I'_3$  in the plots 4.8(c) and (d) are truncated, simply because the cells next to the driver cells never attain some polarization values. For example in the AND configuration, if  $I_3 = -1$ , then we can never have  $I'_1 = 1$ . We expect that for the design of larger circuits, consisting of a network of gates and other elements, the relative magnitude of gate input polarizations and the interference of various input driver settings need to be considered. As a simple example, for the presented majority gate with non-optimal parameters, input leads of different lengths would significantly alter the behaviour.

Overall, we find that in the optimal parameter regime the majority gate works well and functions as expected. The gate attains some undesirable characteristics outside the optimal regime, such as an asymmetric output range and non-zero input threshold, and in a real-world system these characteristics might be exposed by fabrication imperfections and other perturbations.

## Chapter 5

# Conclusion

We have undertaken the first in-depth numerical study of quantum-dot cellular automata (QCA), a beyond-CMOS computing paradigm which represents binary states as bistable charge distributions in cells consisting of several quantum dots. We have concentrated on the time-independent properties of small and simple structures, such as horizontal lines of cells, but have striven to characterize them with as much detail and as little bias as possible, in a material-independent but semi-realistic manner. Starting from an extended Hubbard model, our exact diagonalization calculations avoid commonly used but problematic approximations, such as the intercellular Hartree approximation, and instead introduce two controlled Hilbert space truncations: the fixed-charge and the bond model. We studied the limits of these truncations and established the parameter ranges where they are valid. We were the first to derive (rather than presume) an effective transverse-field Ising model for the QCA approach—another commonly used approximation—and to establish the parameter range in which it can be used, which we observed to be quite restrictive.

In contradiction to previously published results, we found that the cell-cell response function is linear and does not exhibit gain [65]. In our calculations, gain and non-linearity, hitherto claimed as important QCA characteristics, are only observed in the response to static-charge input driver cells. As a consequence, QCA systems cannot retain finite polarization—a definite logic state—in the thermodynamic limit. In practical terms, this limits the size of QCA devices where the maximum size is determined by the quality of the cell-cell response. The observed cell-cell response characteristic is universal for all system parameters, including zero and finite temperatures. The absence of gain makes QCA a less robust scheme overall, and has profound implications for logic applications—QCA’s

raison d’être—which, at least for traditional CMOS-style computing architectures, require binary switches with gain. Implicitly, our findings indicate that the intercellular Hartree approximation is incorrect and its results cannot be trusted.

We have identified charge neutral cells as a strict requirement for operational QCA devices. Additionally, we have established parameter bounds for a functional system. Generally, short cell-cell distances are desirable for optimal operation, but cells cannot be placed closer together than one cell apart, for otherwise cells are no longer distinct physical entities. The upper limit of the operational range of cell-cell distances depends on the nearest-neighbour Coulomb energy  $V_1$  and the temperature, with larger Coulomb terms and lower temperatures increasing the range. For the Coulombic energy scale, we identified an absolute lower bound of  $V_1/t > 20$  (in units of the hopping  $t$ ), a value that increases significantly at moderate and high temperatures. The cell-cell response improves with increasing Coulomb scale  $V_1$ . It is in this limit, where additionally temperatures are not too high and cell-cell distances not too large, that systems of a size practical for building extended circuits are attainable for QCA. For a chosen set of system parameters, we showed explicitly that devices with tens of thousands of cells are feasible. Nonetheless, the identified requirements—charge neutrality and large  $V_1/t$  ratios—pose potentially severe challenges for experimental realizations of the QCA approach.

It has to be noted that our characterization and results only apply to QCA implementations that can be described, with good accuracy, by the extended Hubbard model. Molecular QCA realizations, for example, are expected to behave differently. Similarly, the aluminum island system, which has seen the most experimental work on QCA so far, uses quantum dots with micrometer diameters and is therefore not necessarily well-represented by a Hubbard model. In contrast, our findings should be applicable to atomic silicon quantum dots and other truly molecular-scale semiconductor-based devices.

There is room for more numerical work on the QCA approach. The semi-realistic modelling and simulation of system dynamics is the most important outstanding aspect for an exhaustive evaluation of QCA as a beyond-CMOS technology. For small systems, our exact diagonalization method can be extended to the calculation of time-resolved properties. Notably, this requires the inclusion of a sufficiently accurate dissipative term. The calculation of the switching time of the majority gate and the signal transmission time of wires will then allow one to estimate the overall operational time-scale of QCA devices and therefore permit more in-depth comparisons to CMOS technology and other proposed novel computing architectures.

Within the Ising approximation, stochastic series expansion Monte Carlo techniques can be used for numerical simulations of the QCA approach and would make much larger system sizes computationally accessible. While the Ising approximation is only valid in restricted and rather extreme parameter regimes, this would provide an avenue to study large-scale phenomena such as the design of complex QCA circuits. So far, this has been the domain of intercellular Hartree calculations, which we have proven to be deeply flawed.

A third possibility for future numerical work are models that are closer to specific material systems. For example, for the atomic silicon quantum dots *ab initio* calculations shed light on this material's properties on a very small scale. We have now provided a QCA characterization that is general and therefore relatively abstract. Informed by *ab initio* estimates, our Hubbard model could be extended to include more material-specific characteristics, for example a screening term or a detailed, non-isotropic hopping term. As such modelling becomes very difficult very quickly, it should best be pursued in tandem with experiments that allow one to benchmark and verify the theoretical predictions.

In our opinion, the most promising path for QCA in the near future lies in the experimental domain. We have identified lower bounds for QCA systems' parameters that pose a challenge for experimental realizations, particularly the large  $V_1/t$  ratios. As a next step, experiments could test whether those parameter requirements are achievable and whether small QCA devices can be made to work at a basic, time-independent level. In particular, the atomic silicon quantum dot fabrication capabilities have improved to the point where the reliable manufacturing of small to medium sized structures is within reach. We propose that for a line of cells, static signal transmission can be tested by setting an input with an external static charge and sensing the resulting charge distribution in the cells. Presently, for these systems the strongly perturbative scanning tunnelling microscope measurement process is a challenge, but this will surely be resolved with further work. The observation of a signal transmission charge pattern in a line of ten cells, for example, would establish that QCA does work, in principle, for the atomic silicon quantum dot system and mark a major breakthrough for the QCA approach.

# Bibliography

- [1] G. E. Moore, “Cramming more components onto integrated circuits,” *Electronics Magazine* (1965) .
- [2] M. Bohr, “The evolution of scaling from the homogeneous era to the heterogeneous era,” in *2011 IEEE International Electron Devices Meeting (IEDM)*, pp. 1.1.1–1.1.6. 2011.
- [3] C. Auth, C. Allen, A. Blattner, D. Bergstrom, M. Brazier, M. Bost, M. Buehler, V. Chikarmane, T. Ghani, T. Glassman, *et al.*, “A 22nm high performance and low-power CMOS technology featuring fully-depleted tri-gate transistors, self-aligned contacts and high density MIM capacitors,” in *2012 Symposium on VLSI Technology (VLSIT)*, pp. 131–132. 2012.
- [4] S. Owa, S. Wakamoto, M. Murayama, H. Yaegashi, and K. Oyama, “Immersion lithography extension to sub-10nm nodes with multiple patterning,” in *Proc. SPIE, Optical Microlithography XXVII*, vol. 9052, pp. 90520O–90520O–9. 2014.
- [5] B. Wu and A. Kumar, “Extreme ultraviolet lithography: A review,” *Journal of Vacuum Science & Technology B* **25** (2007) 1743–1761.
- [6] R. Cavin, P. Lugli, and V. Zhirnov, “Science and Engineering Beyond Moore’s Law,” *Proceedings of the IEEE* **100** (2012) 1720–1749.
- [7] “International Technology Roadmap for Semiconductors,” 2011.  
<http://www.itrs.net/Links/2011ITRS/Home2011.htm>.
- [8] K. Bernstein, R. Cavin, W. Porod, A. Seabaugh, and J. Welser, “Device and Architecture Outlook for Beyond CMOS Switches,” *Proceedings of the IEEE* **98** (2010) 2169–2184.

- [9] C. Mead, “Neuromorphic electronic systems,” *Proceedings of the IEEE* **78** (1990) 1629–1636.
- [10] J. Schemmel, D. Bruderle, A. Grubl, M. Hock, K. Meier, and S. Millner, “A wafer-scale neuromorphic hardware system for large-scale neural modeling,” in *Proceedings of 2010 IEEE International Symposium on Circuits and Systems (ISCAS)*, pp. 1947–1950. 2010.
- [11] S. Furber, D. Lester, L. Plana, J. Garside, E. Painkras, S. Temple, and A. Brown, “Overview of the SpiNNaker System Architecture,” *IEEE Transactions on Computers* **62** (2013) 2454–2467.
- [12] D. Nikonov and I. Young, “Overview of Beyond-CMOS Devices and a Uniform Methodology for Their Benchmarking,” *Proceedings of the IEEE* **101** (2013) 2498–2533.
- [13] H. Kam, T.-J. K. Liu, V. Stojanovic, D. Markovic, and E. Alon, “Design, Optimization, and Scaling of MEM Relays for Ultra-Low-Power Digital Logic,” *IEEE Transactions on Electron Devices* **58** (2011) 236–250.
- [14] M. Spencer, F. Chen, C. Wang, R. Nathanael, H. Fariborzi, A. Gupta, H. Kam, V. Pott, J. Jeon, T.-J. K. Liu, D. Markovic, E. Alon, and V. Stojanovic, “Demonstration of Integrated Micro-Electro-Mechanical Relay Circuits for VLSI Applications,” *IEEE Journal of Solid-State Circuits* **46** (2011) 308–320.
- [15] S. A. Wolf, D. D. Awschalom, R. A. Buhrman, J. M. Daughton, S. von Molnr, M. L. Roukes, A. Y. Chtchelkanova, and D. M. Treger, “Spintronics: A Spin-Based Electronics Vision for the Future,” *Science* **294** (2001) 1488–1495.
- [16] D. A. Allwood, G. Xiong, C. C. Faulkner, D. Atkinson, D. Petit, and R. P. Cowburn, “Magnetic Domain-Wall Logic,” *Science* **309** (2005) 1688–1692.
- [17] A. Khitun and K. L. Wang, “Nano scale computational architectures with Spin Wave Bus,” *Superlattices and Microstructures* **38** (2005) 184 – 200.
- [18] M. P. Kostylev, A. A. Serga, T. Schneider, B. Leven, and B. Hillebrands, “Spin-wave logical gates,” *Applied Physics Letters* **87** (2005) .



- [19] B. Behin-Aein, D. Datta, S. Salahuddin, and S. Datta, "Proposal for an all-spin logic device with built-in memory," *Nature Nanotechnology* **5** (2010) 266–270.
- [20] S. Srinivasan, A. Sarkar, B. Behin-Aein, and S. Datta, "All-Spin Logic Device With Inbuilt Nonreciprocity," *IEEE Transactions on Magnetics* **47** (2011) 4026–4032.
- [21] C. S. Lent, P. D. Tougaw, W. Porod, and G. H. Bernstein, "Quantum cellular automata," *Nanotechnology* **4** (1993) 49.
- [22] C. S. Lent and P. D. Tougaw, "Lines of interacting quantumdot cells: A binary wire," *Journal of Applied Physics* **74** (1993) 6227–6233.
- [23] P. D. Tougaw, C. S. Lent, and W. Porod, "Bistable saturation in coupled quantumdot cells," *Journal of Applied Physics* **74** (1993) 3558–3566.
- [24] C. S. Lent, P. D. Tougaw, and W. Porod, "Bistable saturation in coupled quantum dots for quantum cellular automata," *Applied Physics Letters* **62** (1993) 714–716.
- [25] C. Lent and P. D. Tougaw, "A device architecture for computing with quantum dots," *Proceedings of the IEEE* **85** (1997) 541–557.
- [26] C. S. Lent, "Bypassing the Transistor Paradigm," *Science* **288** (2000) 1597–1599.
- [27] C. S. Lent, B. Isaksen, and M. Lieberman, "Molecular Quantum-Dot Cellular Automata," *Journal of the American Chemical Society* **125** (2003) 1056–1063.
- [28] R. P. Cowburn and M. E. Welland, "Room Temperature Magnetic Quantum Cellular Automata," *Science* **287** (2000) 1466–1468.
- [29] G. Bernstein, A. Imre, V. Metlushko, A. Orlov, L. Zhou, L. Ji, G. Csaba, and W. Porod, "Magnetic QCA systems," *Microelectronics Journal* **36** (2005) 619 – 624.
- [30] A. Imre, G. Csaba, L. Ji, A. Orlov, G. H. Bernstein, and W. Porod, "Majority Logic Gate for Magnetic Quantum-Dot Cellular Automata," *Science* **311** (2006) 205–208.
- [31] M. Alam, J. DeAngelis, M. Putney, X. Hu, W. Porod, M. Niemier, and G. Bernstein, "Clocking scheme for nanomagnet QCA," in *7th IEEE Conference on Nanotechnology, 2007. IEEE-NANO 2007.*, pp. 403–408. 2007.

- [32] M. Alam, S. Kurtz, M. Siddiq, M. Niemier, G. Bernstein, X. Hu, and W. Porod, “On-Chip Clocking of Nanomagnet Logic Lines and Gates,” *IEEE Transactions on Nanotechnology* **11** (2012) 273–286.
- [33] A. O. Orlov, I. Amlani, G. H. Bernstein, C. S. Lent, and G. L. Snider, “Realization of a Functional Cell for Quantum-Dot Cellular Automata,” *Science* **277** (1997) 928–930.
- [34] A. O. Orlov, I. Amlani, G. Toth, C. S. Lent, G. H. Bernstein, and G. L. Snider, “Experimental demonstration of a binary wire for quantum-dot cellular automata,” *Applied Physics Letters* **74** (1999) 2875–2877.
- [35] I. Amlani, A. O. Orlov, G. Toth, G. H. Bernstein, C. S. Lent, and G. L. Snider, “Digital Logic Gate Using Quantum-Dot Cellular Automata,” *Science* **284** (1999) 289–291.
- [36] R. K. Kumamuru, A. Orlov, R. Ramasubramaniam, C. Lent, G. Bernstein, and G. Snider, “Operation of a quantum-dot cellular automata (QCA) shift register and analysis of errors,” *IEEE Transactions on Electron Devices* **50** (2003) 1906–1913.
- [37] S. Gardelis, C. G. Smith, J. Cooper, D. A. Ritchie, E. H. Linfield, and Y. Jin, “Evidence for transfer of polarization in a quantum dot cellular automata cell consisting of semiconductor quantum dots,” *Phys. Rev. B* **67** (2003) 033302.
- [38] M. Mitic, M. C. Cassidy, K. D. Petersson, R. P. Starrett, E. Gauja, R. Brenner, R. G. Clark, A. S. Dzurak, C. Yang, and D. N. Jamieson, “Demonstration of a silicon-based quantum cellular automata cell,” *Applied Physics Letters* **89** (2006) .
- [39] M. B. Haider, J. L. Pitters, G. A. DiLabio, L. Livadaru, J. Y. Mutus, and R. A. Wolkow, “Controlled Coupling and Occupation of Silicon Atomic Quantum Dots at Room Temperature,” *Phys. Rev. Lett.* **102** (2009) 046805.
- [40] J. L. Pitters, L. Livadaru, M. B. Haider, and R. A. Wolkow, “Tunnel coupled dangling bond structures on hydrogen terminated silicon surfaces,” *The Journal of Chemical Physics* **134** (2011) .
- [41] R. A. Wolkow, L. Livadaru, J. Pitters, M. Taucer, P. Piva, M. Salomons, M. Cloutier, and B. V. C. Martins, “Silicon Atomic Quantum Dots Enable Beyond-CMOS Electronics,” *arXiv preprint arXiv:1310.4148* (2013) .

- [42] P. D. Tougaw and C. S. Lent, “Dynamic behavior of quantum cellular automata,” *Journal of Applied Physics* **80** (1996) 4722–4736.
- [43] G. Tóth and C. S. Lent, “Role of correlation in the operation of quantum-dot cellular automata,” *Journal of Applied Physics* **89** (2001) 7943–7953.
- [44] P. D. Tougaw and C. S. Lent, “Logical devices implemented using quantum cellular automata,” *Journal of Applied Physics* **75** (1994) 1818–1825.
- [45] K. Hennessy and C. S. Lent, “Clocking of molecular quantum-dot cellular automata,” *Journal of Vacuum Science & Technology B* **19** (2001) 1752–1755.
- [46] E. Rahimi and S. Nejad, “Quantum-Dot Cellular ROM: A nano-scale level approach to digital data storage,” in *6th International Symposium on Communication Systems, Networks and Digital Signal Processing, 2008. CNSDSP 2008.*, pp. 618–621. 2008.
- [47] K. Walus, T. Dysart, G. Jullien, and R. Budiman, “QCADesigner: a rapid design and Simulation tool for quantum-dot cellular automata,” *IEEE Transactions on Nanotechnology* **3** (2004) 26–31.
- [48] M. Taucer, F. Karim, K. Walus, and R. A. Wolkow, “Consequences of many-cell correlations in treating clocked quantum-dot cellular automata circuits,” *arXiv preprint arXiv:1207.7008* (2012) .
- [49] E. P. Blair and C. S. Lent, “Environmental decoherence stabilizes quantum-dot cellular automata,” *Journal of Applied Physics* **113** (2013) .
- [50] J. Hubbard, “Electron Correlations in Narrow Energy Bands. III. An Improved Solution,” *Proceedings of the Royal Society of London. Series A. Mathematical and Physical Sciences* **281** (1964) 401–419.
- [51] H. Fehske, R. Schneider, and A. Weiße, *Computational Many-Particle Physics*. Lecture Notes in Physics. Springer, 2008.
- [52] B. Bauer, L. Carr, H. Evertz, A. Feiguin, J. Freire, S. Fuchs, L. Gamper, J. Gukelberger, E. Gull, S. Guertler, *et al.*, “The ALPS project release 2.0: open source software for strongly correlated systems,” *Journal of Statistical Mechanics: Theory and Experiment* **2011** (2011) P05001.

- [53] X. Gonze, B. Amadon, P.-M. Anglade, J.-M. Beuken, F. Bottin, P. Boulanger, F. Bruneval, D. Caliste, R. Caracas, M. Cote, *et al.*, “ABINIT: First-principles approach to material and nanosystem properties,” *Computer Physics Communications* **180** (2009) 2582 – 2615.
- [54] F. Perez and B. E. Granger, “IPython: a system for interactive scientific computing,” *Computing in Science & Engineering* **9** (2007) 21–29.
- [55] G. Guennebaud, B. Jacob, *et al.*, “Eigen v3,” 2010. <http://eigen.tuxfamily.org>.
- [56] A. Alexandrescu, *Modern C++ design: generic programming and design patterns applied*. Addison-Wesley Professional, 2001.
- [57] “Boost C++ Libraries.” <http://www.boost.org>.
- [58] E. Jones, T. Oliphant, P. Peterson, *et al.*, “SciPy: Open source scientific tools for Python,” 2001–. <http://www.scipy.org/>.
- [59] J. D. Hunter, “Matplotlib: A 2D graphics environment,” *Computing in Science & Engineering* **9** (2007) 0090–95.
- [60] B. Ritter, “An exact diagonalization implementation for quantum-dot cellular automata,” 2014. <https://github.com/meznom/qca>.
- [61] B. Ritter, “Coma: A small Python library aiding with some aspects of running computer simulations,” 2014. <https://github.com/meznom/coma>.
- [62] A. W. Sandvik, “Stochastic series expansion method for quantum Ising models with arbitrary interactions,” *Phys. Rev. E* **68** (2003) 056701.
- [63] A. Auerbach, *Interacting electrons and quantum magnetism*. Graduate texts in contemporary physics. Springer New York, 1994.
- [64] J. Lou and A. W. Sandvik, “Variational ground states of two-dimensional antiferromagnets in the valence bond basis,” *Phys. Rev. B* **76** (2007) 104432.
- [65] B. Ritter and K. Beach. (manuscript in preparation).